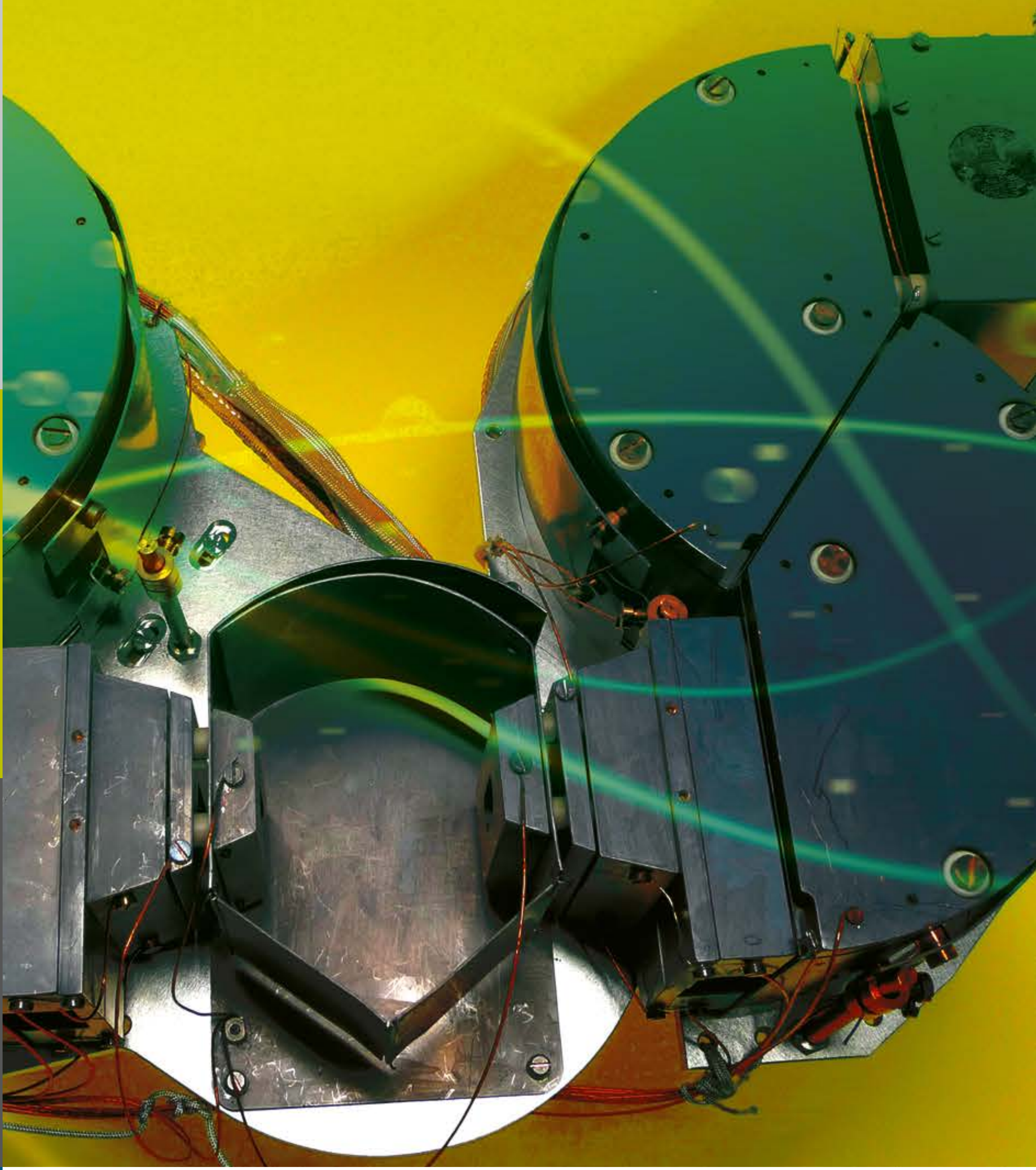

High-energy high-momentum surface spin waves of ultrathin epitaxial 3d transition metal films

Rajeswari Jayaraman

JÜLICH
FORSCHUNGSZENTRUM

Member of the Helmholtz Association

Schriften des Forschungszentrums Jülich
Reihe Schlüsseltechnologien / Key Technologies Band / Volume 68

Forschungszentrum Jülich GmbH
Peter Grünberg Institute (PGI)
Electronic Properties (PGI-6)

High-energy high-momentum surface spin waves of ultrathin epitaxial 3d transition metal films

Rajeswari Jayaraman

Schriften des Forschungszentrums Jülich
Reihe Schlüsseltechnologien / Key Technologies Band / Volume 68

ISSN 1866-1807 ISBN 978-3-89336-890-7

Bibliographic information published by the Deutsche Nationalbibliothek.
The Deutsche Nationalbibliothek lists this publication in the Deutsche Nationalbibliografie; detailed bibliographic data are available in the Internet at http://dnb.d-nb.de.

Publisher and Distributor: Forschungszentrum Jülich GmbH
Zentralbibliothek
52425 Jülich
Tel: +49 2461 61-5368
Fax: +49 2461 61-6103
Email: zb-publikation@fz-juelich.de
www.fz-juelich.de/zb

Cover Design: Grafische Medien, Forschungszentrum Jülich GmbH

Printer: Grafische Medien, Forschungszentrum Jülich GmbH

Copyright: Forschungszentrum Jülich 2013

Schriften des Forschungszentrums Jülich
Reihe Schlüsseltechnologien / Key Technologies, Band / Volume 68

D 464 (Diss., Duisburg, Univ., 2013)

ISSN 1866-1807
ISBN 978-3-89336-890-7

The complete volume is freely available on the Internet on the Jülicher Open Access Server (JUWEL) at www.fz-juelich.de/zb/juwel

Neither this book nor any part of it may be reproduced or transmitted in any form or by any means, electronic or mechanical, including photocopying, microfilming, and recording, or by any information storage and retrieval system, without permission in writing from the publisher.

Zusammenfassung

Oberflächen-Spinwellen von 3d-Übergangsmetallen wurden mit Hilfe eines kürzlich entwickelten hochauflösenden Elektronenspektrometers untersucht. Dazu wurden Filme aus kubisch-flächenzentriertem Kobalt auf Cu(100) Oberflächen präpariert. Die Spinwellen wurden in den [110]- und [010] Richtungen mit Wellenvektoren im Bereich von 0,02 nm^{-1} bis 0,1 nm^{-1} gemessen. Die Richtungsanisotropie der Spinwellen stellte sich als sehr klein heraus. Im Wellenvektorbereich unterhalb von $0,035\mathrm{nm}^{-1}$ wurden zusätzlich zu den Oberflächenspinwellen auch stehende Spinwellen der Filme gefunden. Die den Magnetismus tragenden 3d-Elektronen sind nicht lokalisiert, sondern bilden ein Energieband von beträchtlicher Breite. Spinwellen in diesen Systemen zerfallen rasch in Einelektronenanregungen, die mit einem Spin-flip verbunden sind (Stoner-Anregungen). Dadurch werden die Energiebreiten der Spinwellen sehr groß. Für Kobaltfilme wurden diese Energiebreiten quantitativ ermittelt.

In einem nächsten Schritt wurden epitaktische Nickelfilme auf Cu(100) Oberflächen präpariert. In Übereinstimmung mit früheren unpublizierten Arbeiten wurden jedoch keine Spinwellen auf Nickel gefunden, vermutlich wegen ihren geringen Intensität und ihrer starken Dämpfung.

Um den Einfluss von Nickel auf die Oberflächenspinwellen von Kobalt zu untersuchen, wurden ein bis drei Monolagen von Nickel auf fcc Kobaltfilme aufgebracht. Durch eine genaue Untersuchung der Intensität der Spinwellen als Funktion der Nickel-Schichtdicke ließ sich zeigen, dass die Spinwellen auf der Kobaltseite der Ni/Co Grenzfläche lokalisiert bleiben. Die Abdeckung durch Nickel reduziert die Energie der Spinwellen und führt zu einer weiteren Verbreiterung des Spinwellensignals durch die zusätzlichen Zerfallskanäle für Stoner-Anregungen in der Nickelschicht.

Im Gegensatz zu Nickel ist das 3d-Band von Kupfer vollständig besetzt. Infolgedessen gibt es in Kupfer weniger Möglichkeiten für niederenergetische Anregungen, und deshalb ist die freie Weglänge für Elektronen in Kupfer größer als in Nickel. Dies eröffnet die Möglichkeit, die Spinwellen an der Cu/Co Grenzfläche auch durch dickere Kupferschichten (bis zu $\approx$12 Monolagen) zu sehen. Eine Verbreiterung der Spinwellen und eine Absenkung der Energie ähnlich wie bei Nickel wurde beobachtet.

Infolge seines Reichtums an magnetischen und strukturellen Phänomenen zählt das epitaktische System Eisen auf Cu(100) zu den am meisten untersuchten. In Abhängigkeit von der Schichtdicke lassen sich wenigstens drei verschiedene magnetische Phasen präparieren. In dieser Dissertation wurden die Spinwellen von drei bis fünf Monolagen dicken Fe-Filmen untersucht. Aufgrund der Ähnlichkeit der Spinwellendispersion mit der an bcc-Filmen gefundenen wurde geschlossen, daß die Spinwellen von der sogenannten nanomartensitischen Phase stammen. Diese Phase ähnelt lokal der bcc Struktur, hat jedoch keine langreichweitige Ordnung. Die gleiche Dispersion der Spinwellen wurde für Eisenfilme gefunden, die auf fcc Kobalt deponiert wurden. Daraus wird geschlossen, dass auch in diesem Fall eine nanomartensitische Struktur vorliegt.

Abstract

Surface spin waves on 3d ferromagnetic films are studied in the large wave vector regime with the help of a recently developed high resolution electron energy loss spectrometer.

As a first study, face centered cubic (fcc) cobalt films were prepared by the epitaxial growth of cobalt on Cu(100). Spin waves were probed along the [110]- and the [010]-direction with in-plane wave vectors ranging from $0.02\,\mathrm{nm}^{-1}$ to $0.1\,\mathrm{nm}^{-1}$. The directional anisotropy in the surface spin wave dispersion is found to be very small in this system. In the low wave vector regime (wave vector $< 0.035\mathrm{nm}^{-1}$), standing spin wave modes are observed in addition to the surface spin waves.

In cobalt, like in other transition metal ferromagnets, the 3d electrons are not localized. Rather they form a band of considerable width which offers the possibility for spin-flip excitations (Stoner-excitations) in a wide energy-momentum range. The damping of spin waves by Stoner excitations results in large energy width of the spin wave signals. For the well-defined spin waves of cobalt, the line-widths of the surface spin wave signals were quantitatively determined.

As a next step, epitaxial nickel films were prepared by deposition on Cu(100). In agreement with earlier unpublished work, no spin wave excitation is observed in Ni by inelastic electron scattering presumably due to the strong damping of the spin waves.

As an attempt to study the effect of nickel on cobalt surface spin waves, layers of Ni were deposited on top of Co/Cu(100). Spin waves are seen for up to three monolayers of Ni. By a careful study of the intensity of spin waves as a function of Ni layer thickness, it is proven that spin waves are localized at the Co side of the Ni/Co interface. The presence of Ni broadens the spin wave peak compared to bare Co spin waves, indicating additional decay channels provided by the nickel capping layer.

The 3d-band of copper is fully occupied, and hence copper has less low energy excitations. As a consequence, the mean free path of electrons in copper is much larger than in nickel. This provided the opportunity to look at spin waves localized at the Co interface through thicker layers (up to ≈ 12 layers) of copper. A similar spin wave broadening as for nickel is observed for copper.

One of the extensively studied systems in thin film magnetism is Fe/Cu(100) due to its richness in structural and magnetic phenomena. At least three different magnetic phases can be stabilized depending on the film thickness. In this thesis, surface spin waves of three to five monolayer iron films were studied. From the similarity to the surface spin wave dispersion of bcc Fe films, it is concluded that the observed spin waves arise from the so-called *nanomartensitic* phase. The nanomartensitic phase is locally similar to a bcc structure, however lacking the perfect long range order of the latter. The spin wave dispersion measured on iron films deposited on fcc Co(100) is found to be nearly identical to that of Fe/Cu(100), indicating the structural similarity of the two systems.

Contents

1 Introduction 1

2 Magnetic excitations in solids 7
- 2.1 Magnetic interactions . . . 7
- 2.2 Spin waves versus Stoner excitations . . . 8
- 2.3 Spin waves in the Heisenberg model . . . 11
  - 2.3.1 Spin waves in the $\overline{\Gamma}\,\overline{\mathrm{X}}$-direction of an fcc(100) surface . . . 14
  - 2.3.2 Spin waves in the $\overline{\Gamma}\,\overline{\mathrm{M}}$-direction of an fcc(100) surface . . . 16
  - 2.3.3 Dispersion of an eight layer slab . . . 16
  - 2.3.4 Analytical solution for surface spin waves . . . 17
- 2.4 Experimental probes to study spin waves . . . 19

3 Electron energy loss spectroscopy 23
- 3.1 Basic principles . . . 23
- 3.2 The spectrometer . . . 25
  - 3.2.1 New operation mode of the lens system . . . 27
  - 3.2.2 Relation between experimental intensity and scattering probability . . . 29
- 3.3 Solid angle and lens transmission . . . 29
- 3.4 Calculation of the incident electron energy . . . 31

4 Spin waves in fcc Co layers grown on Cu(100) 35
- 4.1 Introduction . . . 35
- 4.2 The Co/Cu(100) system . . . 36
  - 4.2.1 Preparation . . . 37
  - 4.2.2 Definition of scattering geometry . . . 38
  - 4.2.3 Data evaluation procedure . . . 40
- 4.3 Results of spin wave measurements . . . 44
  - 4.3.1 Experimental data . . . 44
  - 4.3.2 Dispersion . . . 48
  - 4.3.3 Energy width of spin waves . . . 50
  - 4.3.4 Intensity of spin waves . . . 51

4.4 Discussion 53
    4.4.1 Spin waves in the Heisenberg model 54
    4.4.2 Stiffness of spin waves 55
    4.4.3 Qualitative discussion of the width of spin waves 56
    4.4.4 Spin waves in itinerant electron theory 57
4.5 Summary 60

5 Search for spin waves on fcc Ni layers grown on Cu(100) 63
5.1 Introduction 63
5.2 Preparation and characterization 63
5.3 Electron energy loss spectra 65
5.4 Summary 67

6 Spin waves at interfaces 69
6.1 Introduction 69
6.2 Data evaluation procedure 70
6.3 The Ni/Co(100) interface 71
    6.3.1 Experimental details 71
    6.3.2 Spin wave spectra 72
    6.3.3 Dispersion of Ni/Co interface spin waves 77
    6.3.4 Widths of the Ni/Co interface spin waves 78
    6.3.5 Electronic and magnetic structure of the Ni/Co interface . . . 79
6.4 The Cu/Co(100) interface 80
    6.4.1 Experimental details 80
    6.4.2 Spin wave spectra 82
    6.4.3 Dispersion of Cu/Co interface spin waves 83
    6.4.4 Width of Cu/Co(100) interface spin waves 84
    6.4.5 Effect of interface magnetic moment 86
6.5 Summary 87

7 Surface spin waves of ultrathin iron layers 89
7.1 Introduction 89
7.2 The Fe/Cu(100) system 90
    7.2.1 Structure and magnetic properties 90
    7.2.2 Preparation 93
    7.2.3 Spin waves of the 4 ML Fe/Cu(100) system 95
    7.2.4 Spin waves of the 3 ML Fe and 5 ML Fe on Cu(100) 100
7.3 The Fe/Co(100) system 102
    7.3.1 Structure and magnetic properties 102
    7.3.2 Preparation 103
    7.3.3 Spin waves of the 4 ML Fe/8 ML Co/Cu(100) system 104
7.4 Iron clusters on 8 ML Co/Cu(100) 104

7.4.1 Preparation 105
7.4.2 Energy loss spectra 106
7.5 Discussion 109
7.5.1 Spin waves in a 4 ML Fe film 110
7.5.2 Spin waves in 3 ML and 5 ML Fe films on Cu(100) 113
7.6 Summary 115

8 Conclusions and outlook **117**

Bibliography **119**

List of Own Publications **131**

Acknowledgements **133**

Curriculum Vitae **135**

1 Introduction

Ever since electricity has revolutionized the industrial world, magnetism has played a major role, from electric generators, electromotors and transformers to electroacoustic applications. Traditional materials research on magnetism has pursued essentially two directions: the development of magnetic soft (zero-coercivity) materials for applications in transformers and of magnetic hard materials for applications as permanent magnets, e.g. in headphones and loudspeakers. Spurred by the desire to discover novel magnetic phenomena, research turned to magnetic properties of thin films in the later decades of the last century. The research was propelled by the significant progress in the development of deposition techniques such as molecular beam epitaxy, and by the development of *in situ* crystallographic and spectroscopic characterization techniques for probing thin film properties. The epitaxial growth of thin films on single crystal substrates provides means of stabilizing bulk-like phases as thin films of few atomic layers thickness. The thin film nature as well as symmetry-breaking by the interfaces causes additional magnetic interactions acting on different length scales. These additional interactions give rise to significant changes in the magnetic anisotropy, the temperature dependence of the magnetization, the magnetic domain structure and the dynamical properties.

Moreover, epitaxy permits the stabilization of phases, e.g. high temperature phases, which do not exist as bulk phases at room temperature. These metastable structures often exhibit unique magnetic properties, which offer interesting technological applications. Prominent examples include the interlayer exchange coupling observed by Grünberg *et al.* [1] and the giant magnetoresistance effect (GMR) observed by Grünberg [2] and Fert [3] in independent experiments. These discoveries had a great impact on the recording and electronic industries [4–6]. Research and development in this industrial sector is driven by the ever increasing demand to achieve ultra-high storage density i.e. to make extremely small magnetic bits. The operation of magnetic storage devices depends on the magnetization reversal. With the limited magnetic fields available in electronic devices, magnetization switching can only be achieved by motion of domain walls i.e. by reorientation of spins.

From a fundamental point of view spin-transport is best discussed in Fourier-space. There, transport of a single spin is associated with the group velocity of one quantum of a spin wave. It is interesting to note that spin-transport via spin waves involves neither mass nor charge transport. The question of fastest spin-transport thereby becomes the question of the maximum group velocity of a spin wave. The highest group velocities occur for spin waves with wave vectors approximately halfway between the center and the boundary of the Brillouin zone. These extremely short wavelengths also allow for a localization of the spin information stored in the spin wave by building a wave package. Large wave-vector high-energy spin waves tend to be strongly damped. This may be an advantage rather than a draw-back since "ringing" effects (reappearance of spin waves after reflection) are negligible. The damping therefore influences the magnetic recording velocities.

Spin waves have been studied experimentally by ferromagnetic resonance spectroscopy (FMR) and Brillouin light scattering (BLS) for nearly three decades. FMR samples spin wave modes whose wave vector parallel to the surface is close to zero. In BLS, the wave vector of the spin waves probed is in the range of the optical frequency of photons i.e. for wave vectors of the order of 10^{-2}Å^{-1}. Hence, both methods provide information on long wavelength spin waves only. In order to understand the response of the spin system in magnetic nanostructures, information on the microscopic level is required, i.e. on spin waves with wavelength comparable to the lattice constant. The method which is traditionally used for the studies of short wavelength spin waves is inelastic neutron scattering (INS). Because of the small cross sections of neutrons, however, the method is limited to bulk materials.

It was theoretically predicted by Mills in 1967 that electrons can be used as probing particles to study short wavelength surface spin waves [7]. The technique is called electron energy loss spectroscopy (EELS), a technique that is widely used for studies of surface phonons and surface vibrational excitations. To distinguish spin waves from phonons or vibrational excitations one can employ spin-polarized electron sources and measure the intensity asymmetry in spin reversal on magnetically polarized samples. It was shown in a later theoretical paper that the cross section for spin-flip excitations (spin waves and single-electron Stoner excitations) using spin-polarized EELS (SPEELS) is roughly three orders of magnitude smaller than that for vibrational excitations [8]. Moreover, it was predicted that the cross section for spin wave excitations and Stoner excitations will be of the same magnitude. Glazer and Tosatti [9] reported that spin-flip excitations should be observable even in ordinary EELS experiments (unpolarized electron beam and no spin detection) at low incident electron energies.

Following the theoretical predictions, experiments were attempted to observe spin-flip excitations in ferromagnetic samples. The first EELS experiments were performed by Kirschner *et al.* [10] and Hopster *et al.* [11] on Ni samples and ferromagnetic glass samples ($Fe_2B_{12}Si_6$), respectively. The experiments by Kirschner *et al.* utilized a spin-polarized electron source and Hopster *et al.* performed measurements with an unpolarized electron beam, however, with a detector for spin-polarization. The measurements at zero momentum transfer revealed a broad Stoner spectrum with the peak centered around the exchange gap energy of Ni and Fe, respectively. In a later experiment, Modesti *et al.* [12] measured the Stoner spectrum of $Fe_2B_{12}Si_6$ using ordinary EELS and found a spectrum similar to the measurements reported by Hopster *et al.* [11] with spin-polarized EELS. However, no signature of spin waves was detected in any of the above experiments. Venus and Kirschner [13] performed the so-called complete SPEELS experiment (spin-polarized beam and spin-detection of scattered electrons) on Fe with the hope of detecting spin waves, however, without much success as far as it concerned spin waves.

Intrigued by the failure to observe spin waves, Mills *et al.* [14] performed a quantitative theory of spin-flip exchange scattering in Fe using a complete microscopic description of the excitation process. The calculations showed that spin waves should be well resolved in SPEELS spectra, provided that the experiments are carried out with a resolution of at least 25−50 meV. Motivated by this prediction Kirschner performed SPEELS measurements on a five monolayer thick Fe film deposited on a W(110) surface and observed the first signature of spin waves [15]. This success revived the interest to study spin waves and paved the way for the development of improved spectrometers. The first spectrometer specially adapted to the problem was built by a research group in Jülich and was rendered operational in the Max Planck Institut für Mikrostrukturphysik in Halle. The spectrometer used a special combination of 90° deflector followed by a 180° deflector for electron monochromatization [16]. The first studies of short wavelength surface spin waves were performed by Vollmer *et al.* on fcc cobalt layers grown on Cu(100) [17–19]. By now the spectrometer has been successfully put to use to study numerous issues including dispersion of surface spin waves on various ferromagnetic films [20, 21], studies of spin waves in ultrathin films down to one monolayer thickness [22], influence of Dzyaloshinskii-Moriya (DM) interaction on spin waves [23] and the lifetime of spin waves in the presence of DM interaction [24].

In the meantime, a new spectrometer with a combination of two 143°- deflectors as monochromators and analyzers, each, was built in Jülich and delivered to our lab at the start of this thesis. The spectrometer design is based on a theoretical study which predicted considerably higher currents compared to the spectrometer in Halle for an overall energy resolution above 10 meV. However, when this new spectrometer was put into service a rather unpleasant surprise occurred: the resolution degraded dramatically after scattering from a surface. The full width at half maximum increased from 11 meV in the direct beam (no sample in the scattering chamber and analyzer aims directly at the monochromator) to 38 meV after reflection from the sample [25]. The reason for the degradation was determined to be the angular aberrations at large angles in combination with the absence of explicit angular apertures in the spectrometer. Electron optical calculations of electron trajectories from the monochromator to the detector with intermediate scattering from the sample indicated at least three possible methods for introducing angular apertures in the spectrometer. We have chosen the solution which do not require complete re-building of any part of the spectrometer. The solution involved a minor modification of the existing analyzers to accept larger angles perpendicular to the dispersion plane and the introduction of a slit in front of the detector to cut-off the large angle electrons in the dispersion plane. After this modification, high energy resolution could be maintained even after scattering from the sample. In the course of operation of the spectrometer, a new mode of operation of the lens system was discovered which gave nearly four times higher current than the conventional mode [26]. With all the modifications, the spectrometer yielded a high energy resolution of 7 meV after diffuse scattering from the sample. The spectrometer is now furthermore completely characterized with respect to the transmission and solid angle probed by the spectrometer.

The spectrometer is now put to use to systematically study spin waves in the three 3d-transition metal ferromagnetic films Fe, Co and Ni. The films are grown on fcc(100) substrates, primarily Cu(100). All the three systems exhibit similar electronic structure. However, owing to the differences in the magnetic properties and crystallographic structure, the systems are found to exhibit distinct differences in the energy loss spectra. The effect of structure and magnetic properties on spin waves in all the three 3d-ferromagnetic film is systematically studied in this thesis.

As a first experiment, the spin waves in fcc cobalt films deposited on Cu(100) were revisited addressing questions that had to be left open in the previous studies. One concerned the absence of standing wave modes in the spin wave spectra obtained by Vollmer *et al.* [17, 21]. Theories predicted that at least the first standing wave mode should have enough strength to be visible in the spectra measured despite their strong coupling to the Stoner continuum in 3d-metals. The high resolution spectra obtained with the present spectrometer indeed show a clear signature of a standing spin wave mode in addition to surface spin waves in the region of small wave vectors. Another issue of interest is the line-width of the spin waves. The damping of spin waves by Stoner excitations leads to the short lifetimes of spin waves and broad line-widths. Quantitative values for the line-width of the spin wave signals are obtained after taking proper account of the finite energy and wave vector resolution of the spectrometer.

As a further extension of the work, the spin wave measurements were performed on fcc cobalt films grown on Cu(100) after additional deposition of $1-3$ layers of Ni or $1-12$ layers of Cu on top of cobalt. It was found that the intensity of spin waves decays continuously with the thickness of the deposited overlayers. Quantification of intensity based on the mean free path model indicated that the observed spin waves are localized at the cobalt side of the Ni/Co or Cu/Co interface. Moreover, the interface spin wave spectra are broader compared to the free cobalt surface spin waves. This effect is attributed to the additional decay channels provided for spin waves by the magnetic/nonmagnetic overlayers.

Growth of iron films deposited on Cu(100) has been extensively studied over the past two decades due to the possibility of stabilizing different structural and magnetic phases depending on the film thickness. However, the details of the film structure became known only recently. It is generally accepted that thin-film magnetism is strongly affected by even small structural modifications. Much less is known about the influence of structure on magnetic excitations, in particular, spin waves. To this end, the surface spin waves were measured on thin layers of Fe/Cu(100). The spin wave dispersion was found to be nearly identical to the dispersion of bcc Fe(110) layers deposited on W(110). This suggests that the observed spin waves arise from the so-called nanomartensitic phase of Fe/Cu(100) which has a structure akin to bcc, however with no long-range order. The spin wave dispersion was also measured on Fe layers deposited on Co/Cu(100). The dispersion was found to be identical to that of Fe/Cu(100) indicating that Fe realizes the same structure when deposited on Co/Cu(100).

The remainder of this thesis is organized as follows:

chapter 2 provides an introduction to the spin waves and Stoner excitations in a ferromagnetic solid. The theoretical description of spin waves is given within the classical Heisenberg model.

In **chapter 3**, the principles of inelastic electron scattering are outlined followed by a description of our EELS spectrometer. The performance of the spectrometer is demonstrated.

chapter 4 presents the results of the spin wave measurements carried out on the fcc cobalt films deposited on Cu(100).

chapter 5 concerns the results of electron energy loss measurements performed on Ni layers deposited on Cu(100).

The results of Ni/Co and Cu/Co interface spin waves are presented in **chapter 6**.

chapter 7 deals with the results of surface spin waves of iron films deposited on Cu(100) and Co(100) surfaces.

chapter 8 summarizes the results of this thesis and concludes with an outlook on future experiments.

2 Magnetic excitations in solids

At first, the different magnetic interactions present in a ferromagnetic crystal are introduced. Then, two kinds of elementary excitations which involve a spin-flip are discussed: Stoner excitations (single-electron excitations involving a spin-flip) and spin-waves (collective excitations). A theoretical description of spin waves is given within the Heisenberg model. The final section of the chapter reviews the existing experimental techniques to study spin-wave excitations.

2.1 Magnetic interactions

Consider a lattice of spins arranged in a regular manner as in a ferromagnetic solid. There are four relevant magnetic interactions: magnetic dipole interactions between the magnetic moments of the atoms, spin-orbit interaction i.e., the coupling between the spin and the orbital angular momentum of the atoms, Zeeman interaction of the magnetic dipoles with the external magnetic field and the exchange interaction between the spins. The strength of the dipole interaction and the Zeeman energy is of the order of $0.1\,\mathrm{meV}$ [27]. In temperature units, these two interactions cause an alignment of spins only at temperatures of about $1\,\mathrm{K}$ [28]. At higher temperatures, the alignment is lost because of the thermal motion of the spins. The spin-orbit interaction, which couples the spin moment to the lattice gives rise to magneto-crystalline anisotropy. While the technical importance of the magneto-crystalline anisotropy can hardly be overestimated, this interaction is still weak in 3d transition metals and is about $0.05\,\mathrm{eV}$ [29]. All the above three interactions do not explain the ferromagnetism in 3d transition metals with ordering (Curie) temperatures of the order of $\approx 1000\,\mathrm{K}$.

The parallel alignment of spins in a ferromagnet arises from a short range exchange interaction which is of quantum mechanical origin. A model for this interaction was first formulated by Heisenberg [30]. The exchange interaction is based on the Pauli exclusion principle. A more rigid formulation of the Pauli principle applicable to many body systems is that the total wave function of the system of electrons (product of orbital part and spin part) must be antisymmetric. A symmetric orbital part therefore corresponds to antisymmetric spin part (singlet state) and vice versa (triplet state). The symmetric or antisymmetric orbital part gives rise to different electrostatic interaction strength between the ions. In the symmetric orbital part, the electrons tend to be close together and hence experience high Coulomb repulsive interaction. The total energy of the system is nevertheless lower as the electron charge resides primarily between the ion cores. The reverse holds true for an antisymmetric orbital part. Thus, the exchange interaction results from the combination of the overall antisymmetric wave function which couples the electron orbitals to the electron spin and the Coulomb interaction. The exchange energy depends on the overlap of the wave functions. This overlap falls off exponentially with increasing distance between the nuclei. This is in contrast to the Coulomb interaction which falls off more slowly. The exchange energy is of the order of 0.1 eV/atom in 3d transition metals [27].

There are two different pictures widely used to describe the magnetic properties of ferromagnetic materials: the *localized spin* model and the *itinerant* model of magnetism. In the localized spin model, the magnetism is treated assuming that the magnetic electrons are tightly bound within the ions i.e., spins are localized on each lattice site. The overlap between the wave functions of the electrons of neighboring ions is therefore very small. However, in the case of 3d transition metals, the d-electrons which are responsible for the magnetic moments have an appreciable overlap with the 3d electrons on neighboring lattice sites giving rise to energy bands [29]. Hence the electrons are itinerant or de-localized in nature. The band model of ferromagnetism in metals was first developed by Stoner [31] and Wohlfarth [32] and is often called the Stoner model or Stoner-Wohlfarth model. According to this model the energy bands are spin-split. The difference in occupation of the d bands for majority and minority spins leads to a magnetization.

2.2 Spin waves versus Stoner excitations

The spin-polarized energy bands support the possibility of single-electron excitations with a spin-flip. An electron is lifted from an occupied majority spin state and placed in an unfilled minority state. This excitation is termed as Stoner excitation. The minimum energy required for single-electron excitations is given by the Stoner gap $\varDelta$. A schematic illustration of Stoner excitations is shown in Fig. 2.1(a). The exchange splitting $\varDelta E_{\mathrm{ex}}$ in this model is wave vector independent and is the same over the whole Brillouin zone, which is a coarse approximation. For a transition with no momentum change an electron can go from the 'up' band to the 'down' band if it is given an energy equal to the exchange splitting. The q-independence of the exchange splitting is only an approximation which does not hold true in the real band structure of 3d magnetic metals. Even for zero momentum transfer one encounters a broad peak of Stoner excitations centered about the exchange splitting [10, 11, 33]. The value of the exchange splitting is of the order of 2 eV in Fe

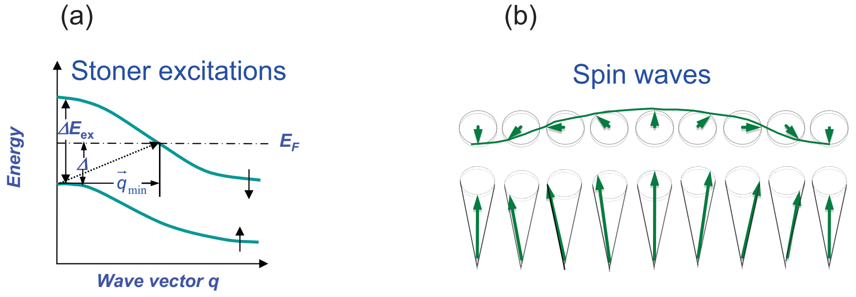

Figure 2.1: Schematic illustration of (a) Stoner excitations in an itinerant band model. The minimum energy for spin-flip is given by the Stoner gap $\varDelta$ and is represented by the dotted arrow. (b) classical picture of spin waves where the spin-flip is distributed over a spin array. When viewed from above it has a perspective of a wave as shown in the top of the figure.

and Co and 0.3 eV in Ni [29]. A second kind of elementary excitation exists in which the spin reversal can be distributed over a large number of atoms thus reducing the energy of the excitations. These collective excitations are referred to as spin waves. The quasiparticles of these spin wave excitations are called magnons. The terms spin wave and magnon are regarded as interchangeable. Magnons are bosons with energy $\hbar\omega$. They carry a magnetic moment of $1\,g\mu_\mathrm{B}$. In the itinerant electron model, a spin wave excitation can be assumed to be a linear superposition of single particle excitations [34]. The spin waves can be conveniently visualized in a semi-classical theory put forward by Herring and Kittel [35]. A schematic illustration of the spin wave is shown in Fig. 2.1(b). The spin $\vec{\mathrm{S}}$ is considered as a classical vector. As one moves through the spin array, the adjacent spins have a well defined phase shift and each spin is engaged in a circular or elliptical precession about its equilibrium orientation. The wavelength of a spin wave is given by the distance between the lattice sites over which a 360° precession occurs. In the case of long wavelength spin waves distributed over a large ensemble of electrons, each spin has a non-vanishing probability to be in a spin down state and hence the energy of the spin wave tends to zero. The thermal excitation of these long wavelength spin waves explains the reduction of the magnetization with temperature in the range $T \ll T_\mathrm{C}$ which is described by the famous Bloch $T^{3/2}$ law [36].

The exploration of long wavelength spin waves provides information on the magnetic anisotropy, magnetization and other properties which can be macroscopically described. To access information on the true microscopic aspects of the physics of

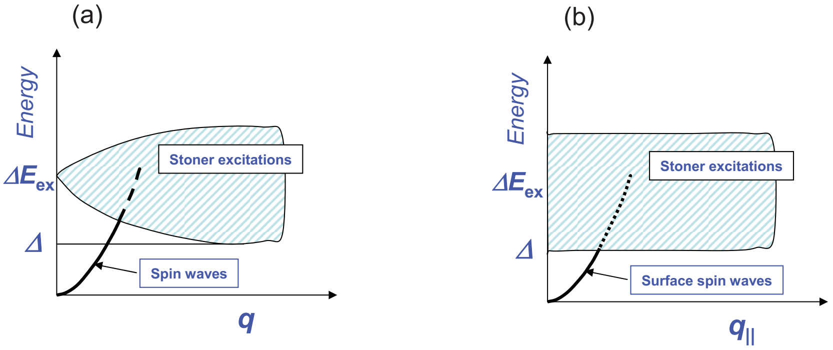

Figure 2.2: Diagram depicting the dispersion of Stoner excitations (shaded area) and spin waves (solid and broken lines) (a) for bulk crystals and (b) for thin films. The spin waves enter the Stoner continuum at a particular wave vector and are damped by the single-particle excitations. In the case of surfaces and thin films, momentum conservation concerns only the parallel component of the wave vector. Therefore additional decay channels for spin waves become available. The figure is reproduced from [37].

the magnetic materials one needs to explore the nature of short wavelength spin wave excitations. In the case of magnetic multilayers, they provide information on the intrafilm and interlayer exchange couplings. Moreover, the contemporary device technology which utilizes dynamics of spins requires the knowledge of damping mechanisms operative for short-wavelength spin waves.

The energy—wave vector relationship of spin waves and Stoner excitations in the case of a strong ferromagnet with Stoner gap Δ and exchange splitting ΔE_{ex} of the d-bands is shown in Fig. 2.2(a). It can be seen that the spin wave merges into the continuum of Stoner excitations at a particular wave vector. Hence, the spin waves are strongly damped by the Stoner excitations thereby imposing a finite lifetime for spin waves. The conservation of total spin moment requires that the spin-flip caused by the destruction of a spin wave is transferred to the band electrons by placing an electron from a spin-up band into a spin-down band. This decay of spin waves is called Landau damping.

The dispersion shown in (a) is operative for bulk materials where the spin waves are characterized by three-dimensional wave vectors. In the case of thin films, the presence of a surface reduces the symmetry. Hence, the angular momentum is conserved only for the wave vector component parallel to the surface $q_{||}$ and wave vector conservation is relaxed for the perpendicular component. This opens up new decay channels, and spin waves are even more strongly damped than in the bulk.

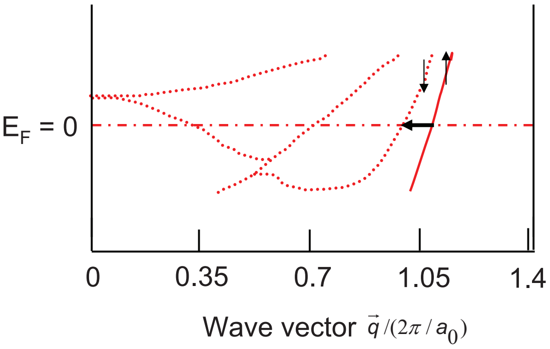

Figure 2.3: Section of the band structure of fcc cobalt taken from Ref. [38]. The figure illustrates the presence of spin-split energy bands due to the hybridization of different minority and majority spin states. A transition involving $q \approx 0.2\text{Å}^{-1}$ is shown as a fat arrow. This introduces zero energy decay channels for spin waves.

A schematic illustration of the dispersion of Stoner excitations and spin waves in 3d ferromagnetic thin film systems is shown in Fig. 2.2(b). A further decay channel arises from the possibility of spin-flip transitions in the s-p bands. The exchange splitting of s-p bands is due to spin-orbit interaction and therefore much smaller compared to that of the d-bands. It can therefore support single particle Stoner excitations of lower energies. An example is shown in Fig. 2.3 which depicts a section of the band structure near the Fermi level calculated for fcc cobalt [38]. The minority and majority spin bands are shown as dotted and solid curves. The Fermi level is indicated by the dash-dotted line. It can be seen that Stoner excitations of zero energy are possible for a wave vector change of $\approx 0.2\text{Å}^{-1}$ (fat arrow in the figure). This opens up a low energy decay channel leading to the damping of spin waves of energy lower than the exchange gap (vertical transitions in the band structure).

2.3 Spin waves in the Heisenberg model

In this section, the spin wave dispersion for a 3d ferromagnet is derived based on the localized spin model (Heisenberg approach). As mentioned before, this model is of limited value for the description of 3d itinerant ferromagnets because spin waves have an infinite life time in this model. In other words, the overlap of neighboring charge distributions is small in this model and therefore the electrons can be assumed to reside in flat d-bands. However, due to its simplicity the model is widely used to heuristically interpret the experimental data. The Heisenberg Hamiltonian for the energy of interaction of atoms i and j can be written as: [29]

$$\boldsymbol{H} = -\sum_{i \neq j}^{N} J_{ij} \vec{\boldsymbol{S}}_i \cdot \vec{\boldsymbol{S}}_j = -2 \sum_{i<j}^{N} J_{ij} \vec{\boldsymbol{S}}_i \cdot \vec{\boldsymbol{S}}_j . \tag{2.1}$$

Here J_{ij} represents the exchange integral connecting atoms i and j and is related to the overlap of the charge distributions of the two atoms. $\vec{\boldsymbol{S}}_i$ and $\vec{\boldsymbol{S}}_j$ are the spin operators in units of $\hbar$ for the ith and jth atom. The spin wave is a particular excited state solution of the Hamiltonian in Eq. (2.1). Here, we account only for the exchange interaction between the nearest-neighbors.

The formulation in Eq. (2.1) allows for different exchange constants between atoms. This is of interest for layers composed of different atoms. Solutions of Eq. (2.1) can be found by introducing a linearization of the model by a mean field approximation.

The mean field approximation considers the energy of an atomic moment of spin $\vec{S}_i$ under the influence of the mean value of the neighboring atomic spins [29]. The spin $\vec{S}$ is considered as a classical vector and not a quantum mechanical operator [1]. The energy of the magnetic moment per atom at site i, $\vec{\mu}_i = -g\mu_{\mathrm{B}}\vec{S}_i$ is written as

$$E_i = -2\vec{S}_i \cdot \sum_j J_{ij}\vec{\mathrm{S}}_j = -\vec{\mu}_i \cdot \vec{B}_i. \tag{2.2}$$

The exchange interaction, thus acquires the character of an internal field. The field acting on the ith spin is written as

$$\vec{\mathrm{B}}_i = -\frac{2}{g\mu_{\mathrm{B}}} \sum_j J_{ij}\vec{S}_j. \tag{2.3}$$

The magnetic exchange interaction exerts a torque $\vec{\mu}_i \times \vec{\mathrm{B}}_i$ on the spins that causes the precession of the spins. The spin precesses around the constant magnetic field according to the torque equation $\vec{T} = \hbar \mathrm{d}\vec{S}/\mathrm{d}t$. The torque acting on the ith spin is

$$\begin{aligned} \hbar\frac{\mathrm{d}\vec{S}_i}{\mathrm{d}t} &= -g\mu_{\mathrm{B}}\sum_j \vec{S}_i \times \vec{\mathrm{B}}_i \\ &= 2\sum_j J_{ij}\left(\vec{S}_i \times \vec{S}_j\right). \end{aligned} \tag{2.4}$$

Expansion of the cross product results in

$$\hbar\frac{\mathrm{d}S_i^x}{\mathrm{d}t} = 2\sum_j J_{ij}\left(S_i^y S_j^z - S_j^y S_i^z\right), \tag{2.5}$$

and similarly for $\hbar\frac{\mathrm{d}S_i^y}{\mathrm{d}t}$ and $\hbar\frac{\mathrm{d}S_i^z}{\mathrm{d}t}$.

The magnetization is assumed to be aligned along the $\hat{z}$ direction and the deviation of magnetic moments from this direction is taken to be small, hence S^x, $S^y \ll S^z$. Neglecting quadratic terms in S^x, S^y one obtains $\mathrm{d}S_i^z/\mathrm{d}t = 0$ [40]. The z-components of the spin are therefore time independent and because of the assumption of identical atoms, S_i^z and S_j^z can be approximated to S. S^x and S^y make precession and have a 90° phase shift with respect to each other. Hence one may write $S^x = \mathrm{i}S^y$. This eliminates S^y terms from the Eq. (2.5) which then becomes,

---

[1] For quantum mechanical formulation in terms of operators and eigenstates see [39], for applications to periodic slabs see [28].

$$\mathrm{i}\hbar \frac{\mathrm{d}S_i^x}{\mathrm{d}t} = 2S \sum_j J_{ij} \left(S_i^x - S_j^x \right) \tag{2.6}$$

Similarly,

$$\mathrm{i}\hbar \frac{\mathrm{d}S_i^y}{\mathrm{d}t} = 2S \sum_j J_{ij} \left(S_i^y - S_j^y \right) \tag{2.7}$$

Since one is interested just in the frequency and not in the phases, the above two equations can be replaced by the following equivalent equation

$$\mathrm{i}\hbar \dot{S}_i = 2S \sum_j J_{ij} \left(S_i - S_j \right). \tag{2.8}$$

It is useful to replace the indices i, j by number triples

$$i \rightarrow \vec{l}_{\|}, l_z, \quad j \rightarrow \vec{l}'_{\|}, l'_z. \tag{2.9}$$

Here, $\vec{l}_{\|}$ is a 2D-number denoting the unit cell and l_z denotes the layer number. The surface layer is assumed to be the layer with $l_z = 1$. The translational invariance of the flat crystal surface ensures that the exchange interactions between the spin at $\left(\vec{l}_{\|}, l_z\right)$ and that at $\left(\vec{l}'_{\|}, l'_z\right)$ depend only on $\vec{l}_{\|} - \vec{l}'_{\|}$. Equation (2.8) then becomes [28]

$$\mathrm{i}\hbar \dot{S}_{\vec{l}_{\|}, l_z} = 2S \sum_{\vec{l}'_{\|}, l'_z} J \left(\vec{l}_{\|} - \vec{l}'_{\|}; l_z, l'_z \right) \left(S_{\vec{l}_{\|}, l_z} - S_{\vec{l}'_{\|}, l'_z} \right). \tag{2.10}$$

For a 2D-periodic slab, the solutions are of the form

$$S_{\vec{l}_{\|}, l_z} = A \left(\vec{q}_{\|}, l_z \right) \mathrm{e}^{\mathrm{i}\left(\vec{q}_{\|} \cdot \vec{r}\left(\vec{l}_{\|}, l_z \right) \right)}. \tag{2.11}$$

The amplitude A depends on the wave vector parallel to the surface of the slab $\vec{q}_{\|}$ and the layer l_z. Here we are interested in the case of identical atoms in each layer. The exchange constant then depends only on the layer index l_z. Assuming a periodic time dependence Eq. (2.10) becomes

$$\hbar\omega A \left(\vec{q}_{\|}, l_z \right) = 2S \sum_{\vec{l}'_{\|}, l'_z} J \left(l_z l'_z \right) \left[A \left(\vec{q}_{\|}, l_z \right) - A \left(\vec{q}_{\|}, l'_z \right) \mathrm{e}^{\mathrm{i}\vec{q}_{\|} \cdot \left(\vec{r}\left(\vec{l}_{\|}, l_z \right) - \vec{r}\left(\vec{l}'_{\|}, l'_z \right) \right)} \right]. \tag{2.12}$$

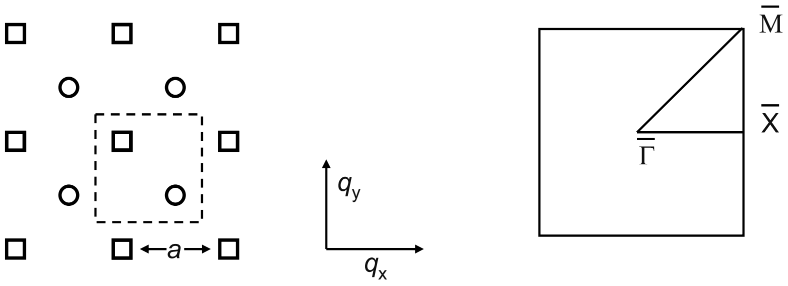

Figure 2.4: Schematic view on the first layer atoms (squares) and second layer atoms (circles) of a fcc(100) slab. Dashed square is the surface unit cell. The lattice constant of the surface unit cell is denoted as a. The right side shows the surface Brillouin zone marking the high symmetry directions.

This is the starting equation for calculating spin waves in a particular direction. As an example, the spin wave dispersion of a slab of N layers with fcc(100) structure is calculated below. It is assumed that the layers lie parallel to the x, y plane. The coupling is assumed to exist between nearest neighbor spins in a given layer and to the layer just above and below. The number of nearest neighbors is 4 within each layer and 4 in the layers above and below. The surface unit cell and the surface Brillouin zone of this crystal is shown in in Fig. 2.4. The calculations are shown for $q_\parallel$ along the [011]-direction as well as the [010]-direction. A comparison of the numerical solution of the surface spin wave dispersion to the analytical solution of the spin wave dispersion of a semi-infinite fcc(100) surface is also given.

2.3.1 Spin waves in the $\overline{\Gamma}\,\overline{\mathrm{X}}$-direction of an fcc(100) surface

Let us consider spin waves in the [011]-direction which is the x-direction in Fig. 2.4. Hence,

$$\vec{q}_\parallel = q_x \vec{e}_x \tag{2.13}$$

with $\vec{e}_x$ the unit vector in the x-direction.
After introducing layer numbers to Eq.(2.12) with $l_z = 1, 2, ...$ for the surface layer, second layer and so on, one obtains for the first layer the equation

$$\begin{aligned}\hbar\omega A_1 &= 2JS\left\{2C_1A_1 - C_1A_1\left(\mathrm{e}^{\mathrm{i}q_\parallel a} + \mathrm{e}^{-\mathrm{i}q_\parallel a}\right) + 4C_{12}V_{12}A_1\right.\\ &\qquad \left.-2C_{12}V_{12}A_2\left(\mathrm{e}^{\mathrm{i}q_\parallel a/2} + \mathrm{e}^{-\mathrm{i}q_\parallel a/2}\right)\right\} \end{aligned} \tag{2.14}$$

Here we have introduced exchange constants in the first layer as $J_1 = C_1J$ and between the first and second layer atoms as $J_{12} = C_{12}J$; J is the exchange between

bulk atoms. For all the deeper layers, the exchange constant is assumed to be as in the bulk. The coefficient V_{12} is $+1$ or -1 for ferromagnetic and antiferromagnetic coupling between the layer 1 and 2, respectively.
For the second layer one has

$$\begin{aligned} \hbar\omega A_2 &= 2JS\left\{2A_2 - A_2\left(\mathrm{e}^{\mathrm{i}q_\parallel a} + \mathrm{e}^{-\mathrm{i}q_\parallel a}\right) + 4C_{12}V_{12}A_2\right. \\ &\quad -2C_{12}V_{12}A_1\left(\mathrm{e}^{\mathrm{i}q_\parallel a/2} + \mathrm{e}^{-\mathrm{i}q_\parallel a/2}\right) \\ &\quad \left.+4A_2V_{23} - 2A_3V_{23}\left(\mathrm{e}^{\mathrm{i}q_\parallel a/2} + \mathrm{e}^{-\mathrm{i}q_\parallel a/2}\right)\right\} \end{aligned} \tag{2.15}$$

The equation for the third and deeper layers are obtained by setting C_{12} equal to one.

$$\begin{aligned} \hbar\omega A_n &= 2JS\left\{2A_n - A_n\left(\mathrm{e}^{\mathrm{i}q_\parallel a} + \mathrm{e}^{-\mathrm{i}q_\parallel a}\right) + 4V_{n-1,n}A_n\right. \\ &\quad -2V_{n-1,n}A_{n-1}\left(\mathrm{e}^{\mathrm{i}q_\parallel a/2} + \mathrm{e}^{-\mathrm{i}q_\parallel a/2}\right) \\ &\quad \left.+4A_nV_{n,n+1} - 2A_{n+1}V_{n,n+1}\left(\mathrm{e}^{\mathrm{i}q_\parallel a/2} + \mathrm{e}^{-\mathrm{i}q_\parallel a/2}\right)\right\} \end{aligned} \tag{2.16}$$

For the Nth layer of an N-layer slab the last two terms are zero. After introduction of a reduced energy E as

$$E = \hbar\omega/8\mathrm{JS} \tag{2.17}$$

one obtains the eigenvalue equation

$$\begin{pmatrix} \alpha_1 - E & \beta_1 & 0 & \cdots & 0 \\ \beta_1 & \alpha_2 - E & \beta_2 & \cdots & 0 \\ \vdots & \vdots & \vdots & \vdots & \vdots \\ 0 & \cdots & 0 & \beta_{N-1} & \alpha_N - E \end{pmatrix} \begin{pmatrix} A_1 \\ A_2 \\ \vdots \\ A_N \end{pmatrix} = 0 \tag{2.18}$$

with

$$\begin{aligned} \alpha_1 &= 0.5C_1\left(1 - \cos q_\parallel a\right) + V_{12}C_{12}, \\ \alpha_2 &= 0.5\left(1 - \cos q_\parallel a\right) + V_{23} + V_{12}C_{12}, \\ \alpha_{n>2,\neq N} &= 0.5\left(1 - \cos q_\parallel a\right) + V_{n-1,n} + V_{n,n+1}, \\ \alpha_N &= 0.5\left(1 - \cos q_\parallel a\right) + V_{N-1,N}, \\ \beta_1 &= -V_{12}C_{12}\cos q_\parallel a/2, \\ \beta_{n>1} &= -V_{n,n+1}\cos q_\parallel a/2. \end{aligned} \tag{2.19}$$

The secular equation for the tridiagonal matrix is easily calculated by the recursion formula

$$f_i(E) = \left(\alpha_i - E\right) f_{i-1}(E) - \beta_{i-1}^2 f_{i-2}(E) = 0 \text{ for } 2 \leq i \leq N. \tag{2.20}$$

$$\begin{aligned} f_0(E) &= 1 \\ f_1(E) &= \alpha_1 - E. \end{aligned} \tag{2.21}$$

2.3.2 Spin waves in the $\overline{\Gamma}\,\overline{\mathrm{M}}$-direction of an fcc(100) surface

The $\overline{\Gamma}\,\overline{\mathrm{M}}$-direction is defined by

$$\vec{q}_{\|} = q_x \vec{e}_x + q_y \vec{e}_y \tag{2.22}$$

with $q_x = q_y$ so that $|\vec{q}_{\|}| = \sqrt{2} q_x$. $\vec{e}_x$ and $\vec{e}_y$ are the unit vectors along the x and y-direction. The layers are assumed to be ferromagnetically coupled. For the first layer one has now

$$\begin{aligned} \hbar\omega A_1 &= 2JS \Big\{ 4C_1A_1 - 2C_1A_1 \left(\mathrm{e}^{\mathrm{i}q_{\|}a/\sqrt{2}} + \mathrm{e}^{-\mathrm{i}q_{\|}a/\sqrt{2}} \right) \\ &\quad +4C_{12}A_1 - 2C_{12}A_2 - C_{12}A_2 \left(\mathrm{e}^{\mathrm{i}q_{\|}a/\sqrt{2}} + \mathrm{e}^{-\mathrm{i}q_{\|}a/\sqrt{2}} \right) \Big\} . \end{aligned} \tag{2.23}$$

For the second layer one has

$$\begin{aligned} \hbar\omega A_2 &= 2JS \Big\{ 4A_2 - 2A_2 \left(\mathrm{e}^{\mathrm{i}q_{\|}a/\sqrt{2}} + \mathrm{e}^{-\mathrm{i}q_{\|}a/\sqrt{2}} \right) + 4A_2 \left(1 + C_{12}\right) \\ &\quad -2\left(C_{12}A_1 + A_3\right) - \left(C_{12}A_1 + A_3\right) \left(\mathrm{e}^{\mathrm{i}q_{\|}a/\sqrt{2}} + \mathrm{e}^{-\mathrm{i}q_{\|}a/\sqrt{2}} \right) \Big\} . \end{aligned} \tag{2.24}$$

For the Nth layer of an N-layer slab one has the equivalent equation to (2.24)

$$\begin{aligned} \hbar\omega A_N &= 2JS \Big\{ 4A_N - 2A_N \left(\mathrm{e}^{\mathrm{i}q_{\|}a/\sqrt{2}} + \mathrm{e}^{-\mathrm{i}q_{\|}a/\sqrt{2}} \right) + 4A_N \\ &\quad -2A_{N-1} - A_{N-1} \left(\mathrm{e}^{\mathrm{i}q_{\|}a/\sqrt{2}} + \mathrm{e}^{-\mathrm{i}q_{\|}a/\sqrt{2}} \right) \Big\} . \end{aligned} \tag{2.25}$$

After normalization to $E = \hbar\omega/8\mathrm{JS}$ one obtains for the matrix elements

$$\begin{aligned} \alpha_1 &= C_1 \left(1 - \cos\left(q_{\|}a/\sqrt{2}\right)\right) + C_{12}, \\ \alpha_2 &= 2 - \cos\left(q_{\|}a/\sqrt{2}\right) + C_{12}, \\ \alpha_{n>2,\neq N} &= 3 - \cos\left(q_{\|}a/\sqrt{2}\right), \\ \alpha_N &= 2 - \cos\left(q_{\|}a/\sqrt{2}\right), \\ \beta_1 &= -0.5C_{12}\left(1 + \cos\left(q_{\|}a/\sqrt{2}\right)\right), \\ \beta_{n>1} &= -0.5\left(1 - \cos\left(q_{\|}a/\sqrt{2}\right)\right). \end{aligned} \tag{2.26}$$

2.3.3 Dispersion of an eight layer slab

As an example, the dispersion curves for an $N = 8$ layer slab of identical atoms are numerically calculated from the equations given in sections 2.3.1 and 2.3.2. The

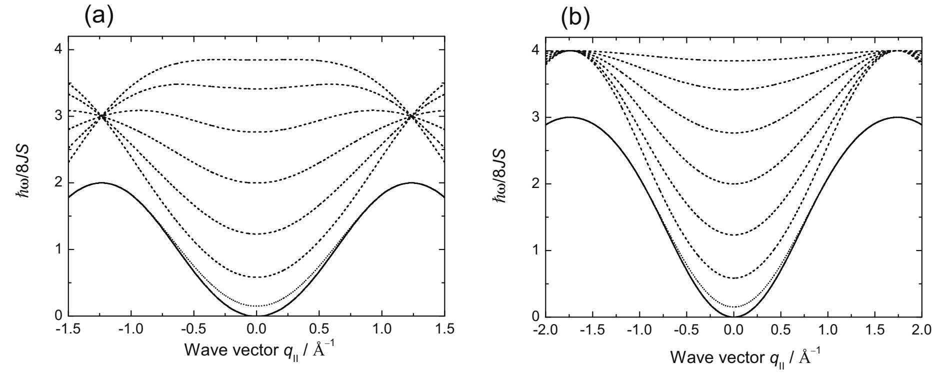

Figure 2.5: Spin wave dispersion of an eight layer (100) fcc slab along the (a) $\overline{\Gamma}\,\overline{\mathrm{X}}$-direction and (b) $\overline{\Gamma}\,\overline{\mathrm{M}}$-direction. The energies are in reduced units $\hbar\omega/8JS$. The solid line represents the spin wave dispersion of the lowest energy mode, the acoustic mode.

dispersion curves are calculated (using Matlab program) for wave vectors along the $\overline{\Gamma}\,\overline{\mathrm{X}}$ and $\overline{\Gamma}\,\overline{\mathrm{M}}$ directions. These are shown in Fig. 2.5(a) and (b), respectively. All the layers are assumed to be ferromagnetically coupled. The value of surface lattice constant a is taken as 2.55 Å.

For an eight layer slab one obtains (8×8) matrix which gives rise to eight eigenvalues. Hence for each choice of $q_{\|}$, there are eight distinct spin-wave frequencies (modes). Two of these modes are surface modes localized on one or the other surface of the eight layer film. The two modes correspond to the in-phase precession (acoustic mode) and out-of-phase precession (optic mode) of spins in the two surface layers. These two modes are represented by the solid and dotted lines in Fig. 2.5(a) and (b), respectively.

2.3.4 Analytical solution for surface spin waves

For the (100) surface of an fcc crystal with nearest neighbor interactions an analytical solution exists for the surface acoustic mode. For this structure, the equation for the second layer is then mathematically identical to all deeper layers (except for the index). A solution that satisfies the pairs of equation (2.14) and (2.15) for the $\overline{\Gamma}\,\overline{\mathrm{X}}$-direction and (2.23) and (2.24) for the $\overline{\Gamma}\,\overline{\mathrm{M}}$-direction is a general solution. Such a surface solution is obtained by the ansatz

$$A_{n+1} = A_n \mathrm{e}^{-\alpha a}. \tag{2.27}$$

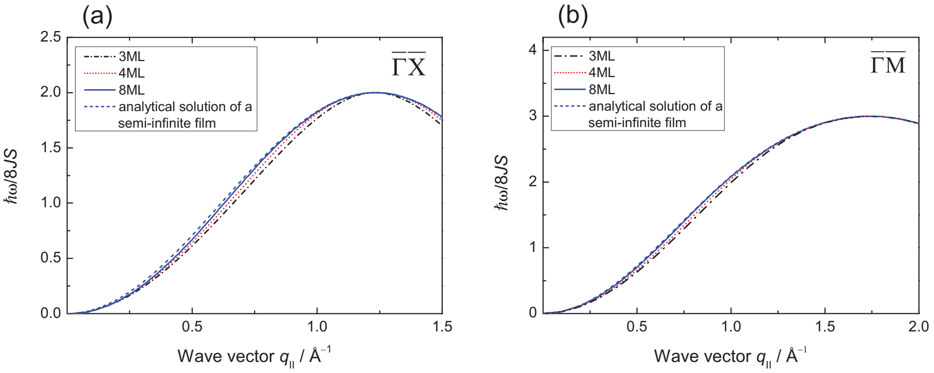

Figure 2.6: Surface spin waves for various thicknesses of an fcc(100) surface calculated in the Heisenberg model with nearest neighbor interactions. The dashed line is the analytical solution of a semi-infinite thick film. The solid, dotted and dash-dotted lines are the numerical solutions for 8, 4 and 3 layer slab, respectively. (a) represents dispersion for $q_{\|}$ along the [011]-direction and (b) that along the [010]-direction.

After insertion of the ansatz into Eq. (2.14) and (2.15) one obtains the consistency condition for $\overline{\Gamma}\,\overline{\mathrm{X}}$-direction as

$$\mathrm{e}^{-\alpha a} = \cos\left(q_{\|}a\right). \tag{2.28}$$

With that, one obtains the surface spin wave dispersion along the $\overline{\Gamma}\,\overline{\mathrm{X}}$-direction as [28]

$$\hbar\omega = 8JS\left(1-\cos q_{\|}a\right). \tag{2.29}$$

The consistency condition for $\overline{\Gamma}\,\overline{\mathrm{M}}$-direction using Eq. (2.27), (2.23) and (2.24) is obtained as

$$\mathrm{e}^{-\alpha a} = \frac{1}{2}\left(1+\cos\left(q_{\|}a/\sqrt{2}\right)\right). \tag{2.30}$$

The surface spin wave dispersion along the $\overline{\Gamma}\,\overline{\mathrm{M}}$-direction is

$$\hbar\omega = 2\mathrm{JS}\left(7-6\cos q_{\|}a/\sqrt{2}-\cos^2 q_{\|}a/\sqrt{2}\right). \tag{2.31}$$

For $q_{\|}=0$ one has $\alpha=0$, hence the surface wave extends infinitely deep into the bulk. For $q_{\|}$ at the zone boundary the cosine terms are equal to -1, hence the surface wave is confined to the first layer.

The analytical solution of the surface spin wave dispersion of a semi-infinite slab obtained above is compared with the numerical solutions obtained in Sections 2.3.1

and 2.3.2 and is depicted in Fig. 2.6. The wave vector $q_{\|}$ is along the $\overline{\Gamma}\,\overline{\mathrm{X}}$- and $\overline{\Gamma}\,\overline{\mathrm{M}}$-direction in (a) and (b), respectively. The numerical solutions of 3, 4 and 8 layer films are represented by dash-dotted, dotted and solid lines, respectively. It can be seen that for thin layers, the surface spin wave dispersion lies lower in energy compared to the dispersion of the semi-infinite crystal (given by the analytical solution). As the thickness of the film increases, the spin wave energy moves closer to the semi-infinite limit. The surface spin wave dispersion of an 8-layer film can already be closely approximated to the surface mode of a semi-infinite crystal.

2.4 Experimental probes to study spin waves

The coupling of spin waves to external probes like photons, neutrons and electrons allows their study by experimental methods. The principal techniques to study spin waves are ferromagnetic resonance (FMR), Brillouin light scattering (BLS), inelastic neutron scattering (INS) and electron energy loss spectroscopy (EELS). The focus here is on the study of spin waves in 3d ferromagnetic elements.

The techniques can be classified into two groups based on the information obtained. FMR and BLS probes spin-wave modes whose wavelength is long compared to the lattice constant. INS and EELS are commonly used to study modes whose wavelength is comparable to the underlying lattice constant.

In FMR experiments, a microwave field illuminates the sample. The total magnetic moment of the sample precesses around the combination of the external field and the anisotropy fields. The resonant absorption of a small transverse microwave field is realized when its frequency matches the precession frequency of a long wavelength spin wave. Typically, the microwave absorption at a fixed frequency is measured as a function of the applied field. The wavelength of the modes probed is comparable to the microwave skin depth and is of the order of a micron. The wave vector of the microwaves is normal to the surface and hence FMR excites spin wave modes with a wave vector component perpendicular to the surface. The wave vector parallel to the surface, $q_{\|} \approx 0$ [41].

In BLS experiments, a laser beam is incident on the sample placed between the poles of a magnet. The photons may interact with the spin fluctuations transferring energy and momentum to the spin waves. The photon can either create or absorb spin waves. The frequency of the scattered photon ω_{s} is shifted from the incident photon frequency ω_{i} by ω, which is the frequency of the spin wave. The wavelength of the modes probed by BLS is of the order of visible light, approximately one-half micron. The optical skin depth of photons in 3d-metals is nearly $100 - 200\,\text{Å}$ [42] and hence suitable to study spin waves near the surface of bulk materials as well as in thin films. The wave vector of the spin waves probed are in the range of 10^{-6} to $10^{-2}\,\text{Å}^{-1}$ [43]. If the solid has a form of a slab with magnetization parallel to the surface, one has surface spin waves in addition to the bulk spin waves [44].

These surface spin waves are called Damon-Eschbach waves. Their frequency lies above the frequency of the bulk spin waves. The Damon-Eschbach mode has a special property to be a non-reciprocal mode i.e., these modes travel only in one direction. The BLS technique can be applied to study spin waves even in ultrathin films. An example of a BLS spectrum measured on 3 ML Fe grown on Cu(100) can be found in Ref. [45].

From the above paragraphs it is clear that FMR and BLS can probe only long wavelength spin waves and are used to determine the fundamental macroscopic parameters of the materials like magnetic anisotropy and magnetization.

The method commonly used in the study of short wavelength collective excitation is inelastic neutron scattering. The kinematics of the excitation process is similar to BLS except that the probe beam now consists of neutrons instead of photons. The typical thermal neutron kinetic energies are about 50 meV with a wave vector in the range of $0.5\,\text{Å}^{-1}$. Hence INS can reach out into the Brillouin zone unlike FMR and BLS. There are two principal interaction processes in neutron scattering:
(i) *nuclear scattering* − scattering of neutrons from the nucleus resulting in structural information and
(ii) *magnetic scattering* − scattering of neutrons due to dipolar interaction between neutron magnetic moment and the field arising from the total spin of the atoms. This latter mechanism yields information about the spin waves.
Both scattering mechanisms are comparable in strength. The energy of thermal neutrons is about 50 meV as mentioned above, whereas the excitation energies of 3d transition metals will be in the range of $100 - 300$ meV at short wavelengths. This range is inaccessible to thermal neutrons. High energy neutrons from spallation sources can be used. However, the spin magnetic moment of neutrons is about 1800 times smaller than that of electrons resulting in weak spin wave signals. The signal becomes weaker at higher spin wave energy due to the falling cross section of neutrons with increasing wave vector. Lacking an electric charge, neutrons penetrate deeply into the matter, therefore they probe primarily bulk properties.

The above mentioned problems with neutron scattering, especially when applied to thin films, can be overcome by using electrons as probe particles. The technique is called Electron Energy Loss Spectroscopy (EELS). The method makes use of electron beams with kinetic energy of several electron volts. Thus the incident energy is sufficiently large to excite short wavelength spin waves in 3d ferromagnets. The Stoner excitation spectrum with energies in the range of electron volts can also be explored with this technique. Moreover, the penetration depth of electrons in solids with energies in the range of electron volts is of the order of few atomic layers [46]. Hence, the scattered electrons carry information primarily about the surface layer of atoms. In the case of 3d ferromagnetic metals, the electron mean free path is spin dependent. The spin averaged mean free path is found to be less than 10 Å even for electrons with kinetic energy close to the vacuum level [47–49].

Hence, the technique provides information about the near surface region. This is the technique of choice for studying surface spin waves of 3d ferromagnets presented in this thesis. A detailed description of the scattering mechanism and the spectrometer is presented in the next chapter.

3 Electron energy loss spectroscopy

3.1 Basic principles

Electrons scattered at a solid surface may undergo elastic and inelastic scattering events. Elastic scattering provides information about the symmetry and the geometric arrangement of atoms near the surface. Inelastic scattering or electron energy loss spectroscopy (EELS) yields information about the excitations in the surface region. In inelastic scattering, a monochromatic electron beam of energy E_0 characterized by the wave vector $\vec{k}^{(\mathrm{i})}$ is incident on the sample. A fraction of the electrons undergoes inelastic scattering and transfers energy and momentum. The analysis of the energy spectrum of scattered electrons characterized by the wave vector $\vec{k}^{(\mathrm{s})}$ provides access to the frequency spectrum of surface excitations. A schematic illustration of the scattering geometry is shown in Fig. 3.1. At surfaces, the symmetry is reduced and the momentum conservation concerns only the parallel component of the wave vector. The energy and momentum conservation between the incoming and the outgoing electrons is

$$E_{(\mathrm{s})} = E_0 \pm \hbar\omega \tag{3.1}$$

$$\vec{k}_{\parallel}^{(\mathrm{s})} = \vec{k}_{\parallel}^{(\mathrm{i})} \pm \vec{q}_{\parallel} \tag{3.2}$$

in which $\hbar\omega$ and $\vec{q}_{\parallel}$ characterize the energy and wave vector of the elementary excitation.

The incident electrons may undergo inelastic scattering in one of the following processes:

(i) An electron on its way toward the surface of a metal experiences the presence of electric fields of oscillating dipoles which may arise from phonons, dipole active localized vibration modes or plasmons at the surface. The impinging electrons will be affected by this long range Coulomb interaction in the vacuum above the target surface. Because of the long-range interaction, this produces small-angle scattering events, substantially more intense than the scatterings observed at large deflection angles. The “lobe” of inelastic scattering events is therefore strongly peaked about the specular direction.

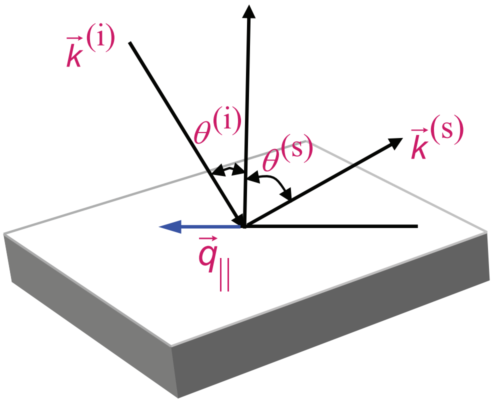

Figure 3.1: Scattering geometry illustrating the parameters of an inelastic electron scattering (EELS) experiment.

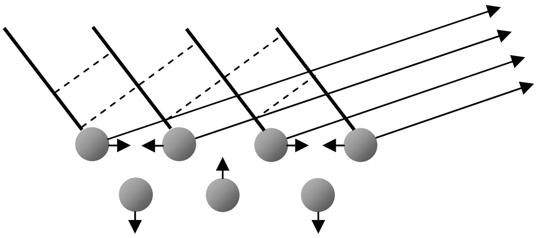

Figure 3.2: Illustration of wide-angle impact scattering mechanism. The figure is reproduced from Ref. [37].

(ii) On a much shorter length scale, electrons can be scattered from the atomic core potential. This type of scattering creates a broad angular distribution. A schematic illustration of the mechanism is represented in Fig. 3.2. The figure is reproduced from Ref. [37].
The scattering mechanisms (i) and (ii) are extensively used in the studies of surface phonon spectroscopy and in the spectroscopy of low-lying vibrational modes of adsorbates.

(iii) Incident electrons may also be inelastically scattered by short range interactions to produce electron-hole pairs. Let us consider the scattering of primary electrons from a ferromagnetic sample. Electrons may undergo scattering from excitations in which the spin of the electron is conserved and excitations in which the electron spin is inverted. Electron-hole pair excitations without change in the spin state of exciting electrons are termed *non spin-flip scattering*, while excitations in which the spin of the emitted electron is opposite to the incident electron spin are

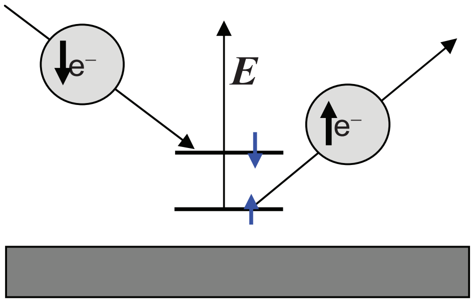

Figure 3.3: Schematic illustration of a spin flip exchange scattering process. The incident spin down electron is absorbed by the ferromagnetic sample and a spin up electron from the sample is emitted.

termed *spin-flip scattering* [13, 15]. The excitation of spin waves and Stoner pairs always necessitates the spin flip transition of the exciting electron. An illustration of the Stoner spin flip scattering event in a 3d ferromagnetic sample with an incoming spin-down electron is shown in Fig. 3.3. A primary spin-down electron falls into an unoccupied minority spin state of the sample and excites a spin-up electron from the occupied majority spin state of the sample, which is then emitted. The opposite process i.e., incident spin-up electron and emitted spin-down electron is less probable because of the nearly filled majority spin-states of 3d ferromagnets.

Excitations of ferromagnetic spin waves appear in the same spin flip channel as the Stoner excitations, however, at lower energies [8,14]. When a spin wave is excited in a ferromagnet, the total magnetic moment of the crystal is reduced by $1\, g\mu_\mathrm{B}$ [40]. Hence, conservation of spin angular momentum requires that the spin waves are excited only by an incident electron whose spin is antiparallel to the majority spins of the sample. Spin wave emission is forbidden for a spin-up incoming electron.

3.2 The spectrometer

The electron spectrometer used for the studies of spin waves presented in this thesis is shown in Fig. 3.4. Detailed description of the design and performance of the spectrometer can be found in [25, 26, 50]. The spectrometer features a $\mathrm{LaB_6}$ thermal cathode, two 143° deflectors as monochromators and analyzers, each, a lens system between monochromators and sample, and a second identical, but reversed lens system between the sample and analyzer. In order to study spin waves, merely a moderate resolution of $10 - 30\,\mathrm{meV}$ is required, however, in combination with high currents to compensate for small signals. To achieve that objective, the spectrometer is equipped with enlarged entrance and exit slits of the deflectors, measuring $0.6 \times 6\,\mathrm{mm}$ instead of $0.3 \times 3\,\mathrm{mm}$ used in the previous spectrometers [16]. The spec-

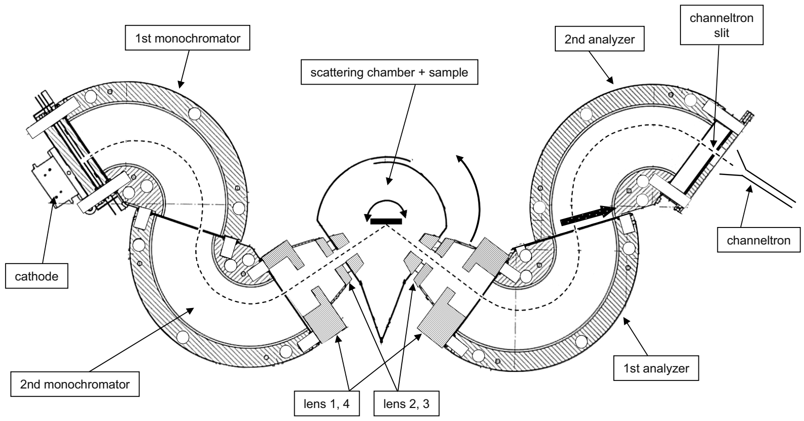

Figure 3.4: Top view of the electron energy loss spectrometer. The spectrometer features a thermal cathode, two 143° deflectors in sequence as monochromators and analyzers, each, a lens system between monochromators and sample, and an identical but reversed lens system between sample and analyzers. An extra slit named the channeltron slit acts as an angular aperture for large angle electrons in the dispersion plane.

trometer exhibited considerably higher currents for energy resolutions above 10 meV compared to the previous designs.

During the initial stages of operation of the spectrometer, the resolution of the spectrometer was found to degrade after scattering from the surface. The degradation was determined to be the outcome of angular aberrations of the electrostatic deflectors at large angles in combination with the absence of angular apertures [25]. To overcome this problem, separate angular apertures were introduced for the electrons traversing at large angles in the dispersion plane (α-angles) and perpendicular to the dispersion plane (β-angles). A detailed description of the degradation effect and the optimum method for the introduction of angular apertures is given in Ref. [25] and is outlined here. Electrons having embarked on trajectories with large α-angles with respect to the central path are blocked from entering the detector by introducing a second slit between the analyzer exit and the channeltron detector. This slit is denoted as "channeltron slit" in Fig. 3.4. The dimension of the slit is 1×6 mm. It is placed at a distance of 10 mm behind the analyzer exit. The slit was found to cut off the large α-angles very effectively. The best solution for handling large β-angles relies on the particular feature of the 143°-deflector in which the angular aberrations can be shifted into the dispersion plane from the plane perpendicular to it. The channeltron slit is then designed to match the larger aberration

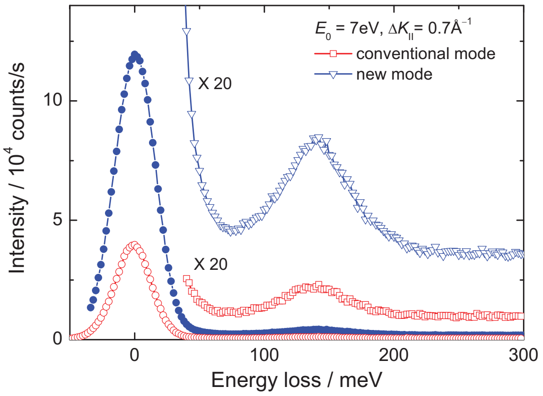

Figure 3.5: Surface spin wave spectra of 8 ML cobalt deposited on a Cu(100) surface. The new operation mode of the lens system (triangles) renders almost four times higher intensity of the inelastic signal compared to the conventional mode (squares).

in the α-plane. The reduction in angular aberration in the β-plane can be achieved by placing entrance and exit slits of the second analyzer at a larger radial position (indicated by bold arrow in the figure). The optimum radial position for the slits to minimize the β aberration coefficient was found to be around $r = 41.5$mm, whereas the slits of the first analyzer and the monochromators are placed at $r = 33.5$mm [25].

3.2.1 New operation mode of the lens system

In the course of operation of the spectrometer, a new mode of operation of the lens system was found which gives a considerable increase in the inelastic signal intensity. The intensity is approximately a factor of four higher than the conventional mode of operation [26]. A detailed description of the new mode of lens operation can be found in Ref. [26]. In the conventional mode, the lens elements 1 and 4 (Fig. 3.4) are operated at a negative voltage with respect to the exit/entrance slits. The lens elements 2 / 3 (see Fig. 3.4) are given a small positive or negative voltage. In the new mode of operation, the lens elements are operated at higher voltages. The voltages of the lens elements 1 and 4 are positive with respect to the exit/entrance slits. The voltages at lens elements 2 and 3 are higher than the voltage at the sample by a factor of $4 - 5$ [26]. In this high voltage mode, the cardinal plane of the lens in the α-plane is moved towards the sample. This results in an increase in the accepted solid angle and hence the intensity of spectral features. An example of the “classical” mode and the new mode of lens operation is shown in Fig. 3.5. The spectra have been obtained from an eight monolayer cobalt film deposited on a clean Cu(100) substrate. Energy losses were probed along the [011]-direction. It can be seen that the intensity of the inelastic signal in the new, high voltage mode is almost four times higher than in the classical mode of operation. Furthermore, it was found that a larger signal (by a factor of 2) is obtained, if the lens elements 1/4 and 2/3 are operated at slightly different potentials (asymmetric potentials). This holds true for both the low-voltage case and the new high-voltage mode. A comparison of spectra showing the effect of symmetric and asymmetric lens settings in the low voltage mode and in the high voltage mode is depicted in Fig. 3.6(a) and (b), respectively. Parameters are the same as in Fig. 3.5. In the case of the low-voltage asymmetric mode, the voltages of the lens elements 1 and 2 are $V_1 = -2.83\,\mathrm{V}$ and $V_2 = 0.9\,\mathrm{V}$, whereas the voltages at 3 and 4 are $V_3 = -2.2\,\mathrm{V}$ and $V_4 = -0.7\,\mathrm{V}$. For the symmetric case, V_1 equals V_3 and V_2 equals V_4. In the case of the high-voltage mode, the lens potentials used for obtaining the spectra are $V_1 = 6\,\mathrm{V}$, $V_2 = 32\,\mathrm{V}$, $V_3 = -1.2$ V and $V_4 = 26$ V. All lens voltages above refer to the impact energy of $E_0 = 7\,\mathrm{eV}$ and pass energies in the monochromator and analyzer of 2.7 eV. It can be seen that the asymmetric setting is particularly advantageous for the high voltage mode. The intensity is roughly a factor of four higher than that for the low voltage asymmetric setting.

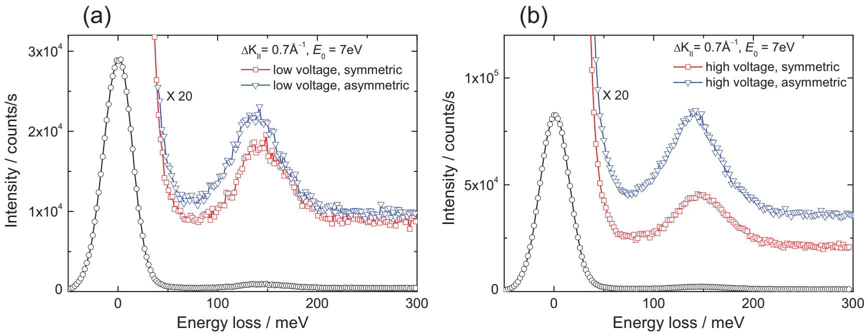

Figure 3.6: Energy loss spectrum of surface spin waves on 8 ML Co deposited on a Cu(100) surface. (a) The spectra have been obtained with the set of low voltages. The asymmetric mode yields a slightly higher intensity. (b) The spectra have been obtained with the set of high voltages. The intensity of the spin wave is higher than for low lens voltages in particular for the asymmetric setting.

3.2.2 Relation between experimental intensity and scattering probability

Theoretical calculations for the spin wave scattering cross sections have been presented by Gokhale *et al.* as early as in 1992 [8]. The quantity which was calculated in that paper is the scattering probability per unit solid angle which is defined as

$$\frac{\mathrm{d}P}{\mathrm{d}\Omega} = \int_{-\infty}^{\infty} \frac{\mathrm{d}^2 P}{\mathrm{d}\hbar\omega \mathrm{d}\Omega} \mathrm{d}\hbar\omega \tag{3.3}$$

This section deals with the relation between the above quantity and the experimentally observed intensities.

The inelastic peak and the resolution function given by the elastic diffuse signals are assumed to be Gaussians with variances s_ω and s_{el}, respectively. Within this assumption, it was shown in Ref. [26] that the experimental intensity can be related to $\mathrm{d}P/\mathrm{d}\Omega$ according to

$$\mathrm{d}P/\mathrm{d}\Omega = \frac{I_{\mathrm{peak}} s_\omega}{I_{\mathrm{in}} T \mathit{\Delta\Omega} s_{\mathrm{el}}} \tag{3.4}$$

where I_{peak} is the peak count rate of the spin wave peak at $E = \hbar\omega$ and I_{in} is the number of electrons impinging on the surface per time. The ratio of variances s_ω and s_{el} can be determined from the energy loss spectrum.

The quantitative analysis of the spectral intensities requires the knowledge of the solid angle ($\mathit{\Delta\Omega}$) which is probed by the spectrometer. Even electrons emitted from the sample within the solid angle $\mathit{\Delta\Omega}$ pass the analyzer within its acceptance angle with a probability T that is smaller than one. This transmission probability T is the product of the energy transmission of the analyzer T_{E} and the lens transmission T_{L}. A detailed calculation of the acceptance angles and transmission of the analyzer and the calculation of solid angle and lens transmission is given in Ref. [26] and is briefly described in the next section.

3.3 Solid angle and lens transmission

The first step in the calculation of the solid angle probed by the spectrometer is the determination of the acceptance angles of the analyzer. The effective acceptance angles are determined by numerical simulations as described in Ref. [26]. The maxima in the energy transmission curves T_{max} are determined as a function of the angular spread ($\pm\alpha_{\mathrm{max}}, \pm\beta_{\mathrm{max}}$) of the beam of electrons entering the analyzer. Transmission is defined as the fraction of electrons entering the entrance slit that leave the exit slit. The maximum transmission multiplied by α_{max} and β_{max} is plotted as a function of α_{max} and β_{max} and is shown in Fig. 3.7 for the second analyzer with slits in the radial position $r = 41.5\,\mathrm{mm}$. The figure is reproduced from Ref. [26]. The products of

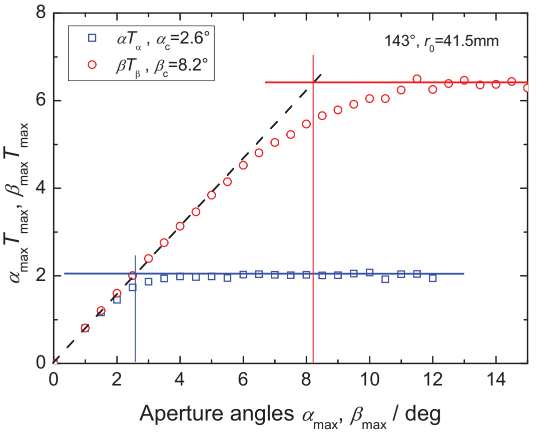

Figure 3.7: Determination of the effective angular apertures α_c and β_c from simulation of the 143° deflector with the entrance and exit slits at $r = 41.5\,\mathrm{mm}$. The product of the maxima in the energy transmission curves T_max and the aperture angles of the electron beam entering the analyzer α_max and β_max is plotted versus the aperture angles α_max and β_max.

$\alpha_\mathrm{max}T_\mathrm{max}$ vs. α_max with $\beta_\mathrm{max} = 1°$ and $\beta_\mathrm{max}T_\mathrm{max}$ vs. β_max with $\alpha_\mathrm{max} = 1°$ are plotted as squares and circles, respectively. For small α_max and β_max the transmission T_max stays constant resulting in the same linear increase of $\alpha_\mathrm{max}T_\mathrm{max}$ and $\beta_\mathrm{max}T_\mathrm{max}$. For large α_max and β_max when α_max and β_max exceed the maximum angles accepted at pass energy, the transmission T_max decays as $1/\alpha_\mathrm{max}$ and $1/\beta_\mathrm{max}$, respectively and the product $\alpha_\mathrm{max}T_\mathrm{max}$ and $\beta_\mathrm{max}T_\mathrm{max}$ stays constant. The effective angular apertures are obtained from the intersection of linear extrapolations of the two regimes (see lines in Fig. 3.7). The values are $\alpha_\mathrm{c} = 2.6°$ and $\beta_\mathrm{c} = 8.2°$. A similar procedure is applied to determine the cut-off angles for the first analyzer with $r_0 = 33.5\,\mathrm{mm}$ and the obtained values are $\alpha_\mathrm{c} = 5.2°$ and $\beta_\mathrm{c} = 5.7°$. Hence, the effective cut-off angles for the combination of two analyzers are $\alpha_\mathrm{c} = 2.6°$ and $\beta_\mathrm{c} = 5.7°$.

The transmission of the combination of the two analyzers at pass energy with a random distribution of entrance angles with $|\alpha_\mathrm{c}| < 2.6°$ and $|\beta_\mathrm{c}| < 5.7°$ was calculated to be $T_\mathrm{E} = 0.36$ [26].

Knowing the acceptance angles of the analyzers, the solid angle probed by the spectrometer $\mathit{\Delta\Omega}$ after diffuse scattering from the sample and the transmission probability T for the electrons leaving the sample within the said solid angle to pass the analyzer can be calculated. The values of the cut-off angles for diffuse scattering represented by $\alpha_\mathrm{t,c}$ and $\beta_\mathrm{t,c}$ can be calculated from plots such as that in Fig. 3.7. The transmission T_L of the lens system for electrons diffusely scattered by the sample within $\pm\alpha_\mathrm{t,c}$ and $\pm\beta_\mathrm{c}$ to enter the analyzer with $|\alpha_\mathrm{c}| < 2.6°$ and $|\beta_\mathrm{c}| < 5.7°$ is determined from calculations [26]. The quantity that enters into Eq. (3.4) is then given by

$$T\mathit{\Delta\Omega} = 4\alpha_\mathrm{t,c}\beta_\mathrm{t,c}\left(\frac{\pi}{180°}\right)^2 T_\mathrm{L}T_\mathrm{E} \tag{3.5}$$

The product of the solid angle and transmission of the lens system $T_{\mathrm{L}}\mathit{\Delta\Omega}$ depend on the impact energy E_0 at the target. It was shown in Ref. [26] that $T_{\mathrm{L}}\mathit{\Delta\Omega}$ can approximately be related to E_0 according to the following fitting equations

$$10^4 T_{\mathrm{L}}\mathit{\Delta\Omega} = 108 + 30\exp\left(-0.05E_0/\mathrm{eV}\right) \tag{3.6}$$

$$10^4 T_{\mathrm{L}}\mathit{\Delta\Omega} = 19.5 + 30\exp\left(-0.05E_0/\mathrm{eV}\right) \tag{3.7}$$

for the high lens voltage mode and low lens voltage mode, respectively.

The dispersion of spin waves is constructed by measuring energy loss spectra as function of the wave vector. The required wave vector is selected by the angle of the scattered beam with respect to the specular reflection as shown later (Section 4.2.2). Hence the wave vector resolution depends on the acceptance angles of the spectrometer in the scattering plane i.e., the α-plane. The acceptance angles determined from the procedure described in Fig. 3.7 and plotted as a function of E_0 were found to be approximately described by

$$\alpha_{\mathrm{t,c}}/\mathrm{deg} = 7.2\left(E_0/\mathrm{eV}\right)^{-0.22} \tag{3.8}$$

$$\alpha_{\mathrm{t,c}}/\mathrm{deg} = 4.8\left(E_0/\mathrm{eV}\right)^{-0.28} \tag{3.9}$$

for the high voltage and low voltage mode, respectively [26]. These equations are for electrons with a pass energy of $E_{\mathrm{pass}} = 2.7\,\mathrm{eV}$ in both monochromators and both analyzers.

3.4 Calculation of the incident electron energy

Measurements of the dispersion of energy losses as a function of wave vector requires a precise knowledge of the kinetic energy of the incident electrons E_0. The kinetic energy E_0 is given by [51],

$$E_0 = E_{\mathrm{pass}} + e\mathit{\Delta V} + e\left(\Phi_{\mathrm{graphite}} - \Phi_{\mathrm{sample}}\right) \tag{3.10}$$

Here E_{pass} is the pass energy in the monochromator, $e\mathit{\Delta V}$ in eq. (3.10) is the voltage difference between the exit of the monochromator and the sample, and $e\left(\Phi_{\mathrm{graphite}} - \Phi_{\mathrm{sample}}\right)$ is the work function difference between the graphite-coated surface of the spectrometer and the sample.

The pass energy is calculated from the nominal pass energy E_{passnom}. The latter is defined as the relation between pass energy and deflection voltage $\mathit{\Delta U}$ in an ideal cylindrical field [25]

$$E_{\mathrm{passnom}} = \frac{e\mathit{\Delta U}}{2\ln\left(r_{\mathrm{a}}/r_{\mathrm{i}}\right)} \tag{3.11}$$

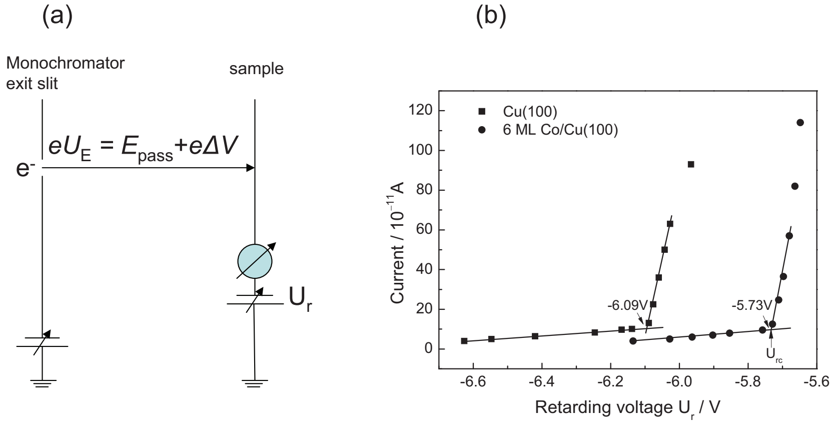

Figure 3.8: (a) Experimental arrangement for work function measurements. (b) Determination of the critical retarding voltage U_{rc} at which the sample current onsets in the case of Cu(100) (squares) and 6 ML Co deposited on Cu(100) (circles). See text for more details.

in which r_{a} and r_{i} are the radii of the outer and inner deflection plates [25]. The actual pass energy for the 143°-deflector is [25]

$$E_{\mathrm{pass}} = 1.18\, E_{\mathrm{passnom}}. \tag{3.12}$$

The values of r_{a} and r_{i} for our spectrometer are 60.3 mm and 20.3 mm, respectively. Hence,

$$E_{\mathrm{pass}}/e = 0.54\varDelta U. \tag{3.13}$$

The work function difference between the graphite coating of the electrodes and the sample is determined in the following way: electrons directed toward the sample from the monochromator exit slit with energy $eU_{\mathrm{E}} = E_{\mathrm{pass}} + e\varDelta V$ are retarded by the voltage U_{r}. A diagram of the arrangement is shown in Fig. 3.8(a). When the retarding voltage is strongly negative, the sample current is zero. As the retarding voltage is increased, a break point U_{rc} is reached at which an onset of the sample current is detected. The difference between the voltage eU_{E} and eU_{rc} is the work function difference between the graphite and the sample. To compensate for the difference in the work functions, this additional voltage is applied to the sample. An example for the determination of the work function of graphite and of Co(100) is explained with the help of Fig. 3.8(b).

The work function of graphite is determined indirectly from the work function of clean Cu(100) whose value is precisely known from the literature [52]. The value of eU_{rc} is determined for the clean Cu(100) sample by measuring sample current as a function of retarding voltage, eU_{r} (solid squares). The value of eU_{rc} is obtained as -6.09 eV. The value of eU_{E} for this particular measurement is 5.96 eV. Hence, the work function difference between graphite and copper is 0.13 eV. The work function of Cu(100) is known to be 4.59 eV from Ref. [52]. Using this value, the work function of graphite is established to be $4.59+0.13 = 4.72$ eV. This value is in good agreement with the value of 4.8 eV reported in literature for clean graphite [53]. Knowing the work function of graphite, the next step is the determination of the work function of Co(100). Proceeding in the same way as for Cu(100), the value of eU_{rc} for 6 ML Co/Cu(100) is determined to be -5.73 eV as shown in Fig. 3.8(b) (solid circles). The difference between eU_{E} and eU_{rc} is 0.23 eV. The work function of graphite is 4.72 eV as found earlier. Using this value, the work function of fcc Co(100) deposited on Cu(100) is found to be $4.72+0.23 = 4.95$ eV which is in good agreement with the literature value for bulk cobalt [52]. To compensate for the difference between the work function of graphite and Co(100), the additional acceleration of 0.23 eV has to be given to the electron beam to obtain the same impact energy at the cobalt sample as on a graphite reference.

4 Spin waves in fcc Co layers grown on Cu(100)

4.1 Introduction

High wave vector spin waves in 3d-ferromagnets are embedded in a continuum of electron-hole pair excitations involving a spin flip (Stoner excitations) (see Fig. 2.2). Spin waves in these systems are therefore strongly Landau damped. Landau damping is particularly strong for thin films and surfaces due to the broken translational symmetry which increases the number of available channels for Stoner excitations. Owing to strong damping, the surface spin waves in 3d-ferromagnets exhibit broad line-widths which increase with increasing wave vector component parallel to the surface. The high energy surface spin wave excitations in ultrathin cobalt films on Cu(100) were extensively studied by Etzkorn *et al.* with spin resolved energy loss spectroscopy [17, 21]. However, reliable data on the width of the surface spin wave signals do not exist: the moderate resolution available in those experiments restricted the observation of spin waves to the high wave vector regime. Moreover, the additional broadening of spin wave widths imposed by the finite acceptance angles of the spectrometer, which transforms into a finite $q_{\|}$-range (kinematic broadening), was neglected. As shown in Ref. [51], the effect of kinematic broadening on the width of the spin waves is significant, especially when the spectrometer is operated in a mode with low energy resolution. Another unresolved issue in the interpretation of the previous experiments was the absence of any sign of standing wave modes in the measured spin wave spectra. Such modes are predicted within the Heisenberg model and also by more advanced theories. Calculations which take the itinerant nature of electrons into account show that the higher energy standing modes are strongly damped. However, at least the first standing mode should have enough strength to be seen as a peak in the measured spectra [54–56].

Because of the open questions in the previous studies, the problem of spin waves in fcc cobalt films on Cu(100) was revisited in this thesis. The high energy resolution spectra rendered by the present spectrometer indeed show standing spin waves in addition to surface spin waves at small wave vectors. The spin waves were probed down to wave vectors of 0.23Å^{-1}. Moreover, the use of a standard thermal emission cathode in the present spectrometer enables the measurement of spin waves with arbitrary spin and wave vector orientation with equal intensity, whereas, the spin asymmetry is lower by a factor of two along the [010]-direction as opposed to the previously studied [011]-direction. Quantitative values for the full width at half maximum (FWHM) of the spin wave losses are obtained after taking the finite energy resolution and finite wave vector resolution of the spectrometer into account. Furthermore, the complete characterization of our spectrometer with respect to the transmission and the solid angle probed by the spectrometer (as shown in chapter 3) enabled the determination of the absolute scattering probability for inelastic scattering from measured spectral intensities.

The outline of the chapter is as follows: Section 4.2 provides an introduction to the Co/Cu(100) system. The sample preparation procedure, the geometry of electron scattering, the calculation of wave vectors and the data evaluation procedure are discussed in this section. Section 4.3 presents the results of spin wave measurements. Section 4.4 discusses the experimental dispersion with the classical theoretical approach, the Heisenberg model. A quantitative analysis of the FWHM and the stiffness of the spin waves is also presented. The section furthermore provides a comparison of the experimental data to a completely parameter-free theory [51] of the spin wave susceptibility that takes into account the itinerant nature of electrons of the ferromagnetic film/substrate combination.

4.2 The Co/Cu(100) system

Ultrathin cobalt films grown on Cu(100) are considered as a model system for low dimensional magnetism. The equilibrium phase of bulk Co at room temperature is hcp with a phase transition to fcc lattice occuring above 695 K [57]. The fcc phase can be stabilized at room temperature by pseudomorphic growth on a clean Cu(100) surface [58]. This is due to the small lattice mismatch of only 2% between fcc Co (3.56 Å) and Cu (3.61 Å) [59]. In fact, the presence of the small lattice mismatch gives rise to strain in the film which is accommodated by a slight expansion in the surface unit cell of the film and compression normal to the film plane [59]. This implies that the cobalt actually has a tetragonally distorted fcc structure [60] (equivalent to a body centered tetragonal structure, bct). This distortion however, is small and is mostly neglected in theoretical studies of spin waves. To ensure good quality epitaxial films, the thin films are often deposited at elevated temperatures or are annealed after room temperature or low temperature deposition. However, a known problem of this system is that the interdiffusion of Co and Cu begins at 490 K [61] though bulk Co and Cu are considered immiscible below $\approx$ 900 K [62]. Moreover, for lower coverages the system is known to exhibit intermixing between Co and Cu even at room temperature with one monolayer (ML, 1ML = 1.8Å) exhibiting 45 % Cu in the surface [63]. The growth mode is also found to deviate from the nearly layer-by-layer growth found at higher coverages at least up to a coverage of ≈ 2 ML where islands of the second layer nucleate long before the first layer is completed [64, 65]. The magnetic and electronic properties are strongly related to the morphology of the films. Thus, it is of vital importance to control Cu diffusion onto Co as this is the key to control the morphology.

Cobalt films exhibit a strong thickness dependence of the ferromagnetic ordering temperature. The Curie temperature (T_C) of ultrathin films is strongly reduced compared to the value of bulk Co $\left[T_C^{bulk} = 1388\mathrm{K}\right]$. The T_C of single fcc Co layer is about 50 K. The Curie temperature increases with film thickness reaching a value of about 900 K for 6 ML [58]. The onset of ferromagnetism at room temperature occurs at ≈ 1.7 ML coverage [62]. For films with Co thickness ≥ 2 ML, the easy axis of magnetization is along the $\langle 110 \rangle$ directions.

4.2.1 Preparation

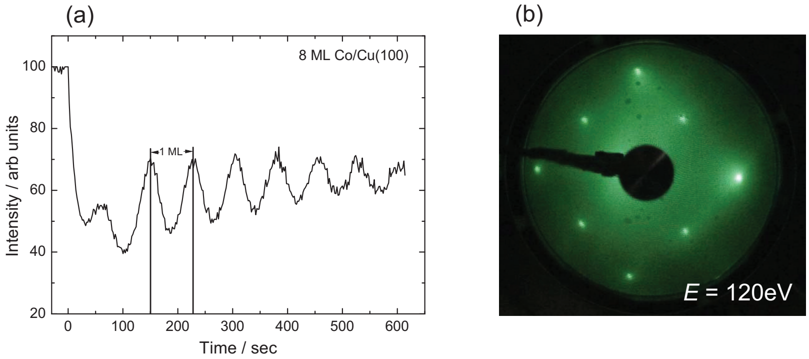

Figure 4.1: (a)MEED oscillations for an 8 ML Co film grown on a Cu(100) surface at room temperature. The maxima in intensity mark the most complete surface layer. The distance between the successive maxima corresponds to the deposition of one monolayer. (b) LEED diffraction pattern observed on an 8 ML Co/Cu(100) surface.

The Cu(100) substrates are prepared by repeated cycles of 1 keV Ar^+ ion sputtering followed by annealing at 700 K until a sharp well-ordered $p(1 \times 1)$ pattern was observed in low energy electron diffraction (LEED), and Auger electron spectroscopy (AES) indicated no contamination within the detection limit. Cobalt was deposited using electron beam stimulated evaporation from high purity rods onto the Cu substrate held at room temperature. The deposition rate was about 1.25 ML/min. The residual gas pressure during evaporation was better than 5×10^{-10} mbar. The film thickness was calibrated by Medium Energy Electron Diffraction (MEED) which was performed using rear view LEED optics and the electron gun of the Auger system. The electron beam energy was 3 keV. The intensity of the diffracted beams in a MEED experiment displays pronounced oscillations during epitaxial growth. The oscillations have monolayer periodicity, characteristic of a layer-by-layer growth mode [65,66]. Thus, the thickness of the film can be evaluated from the number of periods. Typical MEED oscillations are shown in Fig. 4.1(a) for the intensity variation of the specular beam. The relative intensity maxima are interpreted as the completion of a monolayer. The MEED oscillations were not monitored on the samples used for spin wave measurements. This is because it was found that the bombardment of 3 keV electrons from the electron gun of the Auger system could crack some hydrocarbons or CO rendering a sample showing vibrational spectra characteristic of C_xH_y contaminations. The flux monitor of the evaporator which was calibrated with the MEED oscillations was employed for monitoring the thickness of the films on which spin wave measurements were performed. All measurements were carried out on 8 ML thick Co films. The Co films adopt the fcc lattice of the Cu(100) substrate. This is confirmed by the nearly identical $p(1 \times 1)$ diffraction pattern observed in LEED for clean Cu and for Co films deposited on Cu(100) substrates. A typical LEED diffraction pattern observed on an 8 ML Co film is shown in Fig. 4.1(b).

After preparation, the samples were transferred to the “spectrometer chamber” housing the electron spectrometer. The samples were briefly annealed to ≈ 400 K (which is below the interdiffuion temperature of Co and Cu) to remove CO detected in energy loss spectra. An example energy loss spectrum of the prepared sample before and after annealing is shown in Fig. 4.2. Prior to annealing, the spectrum exhibits two vibrational loss lines at 57 and 243 meV. The peaks correspond to the metal-C and C-O stretching vibrations respectively [67] which almost disappear after the brief annealing. The energy loss spectra were measured in the specular direction. It was recently shown that even for a film prepared at room temperature, a noticeable amount of Cu diffuses through Co in about 20 h after preparation [61]. All the measurements presented here were carried out within 8 h after preparation of the sample.

4.2.2 Definition of scattering geometry

A schematic representation of the geometry of the electron scattering used in all spin waves measurements presented in this thesis is shown in Fig. 4.3(a). An electron beam of wave vector $\vec{k}^{(\mathrm{i})}$ is incident on the sample at an angle $\theta^{(\mathrm{i})}$ referenced to the surface normal. The electron beam of wave vector $\vec{k}^{(\mathrm{s})}$ emerges at an angle $\theta^{(\mathrm{s})}$ from the surface normal after transferring energy and momentum to excitations on the

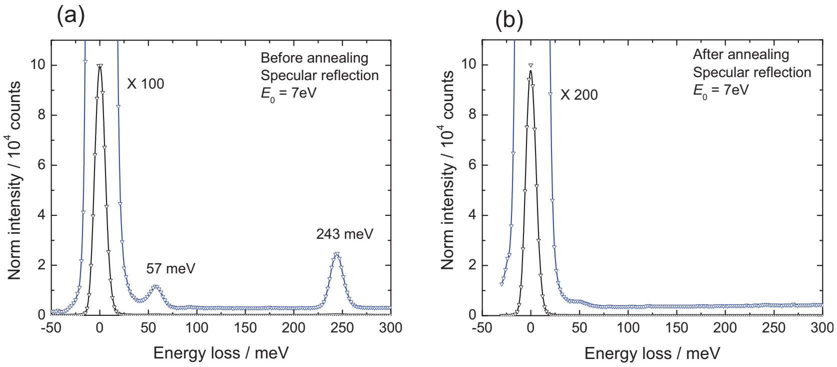

Figure 4.2: (a) Electron energy loss spectrum of an 8 ML Co film on Cu(100) measured in the specular direction prior to annealing showing energy loss due to CO contamination on the surface. (b) represents the spectrum after briefly annealing to ≈ 400K where CO is completely eliminated.

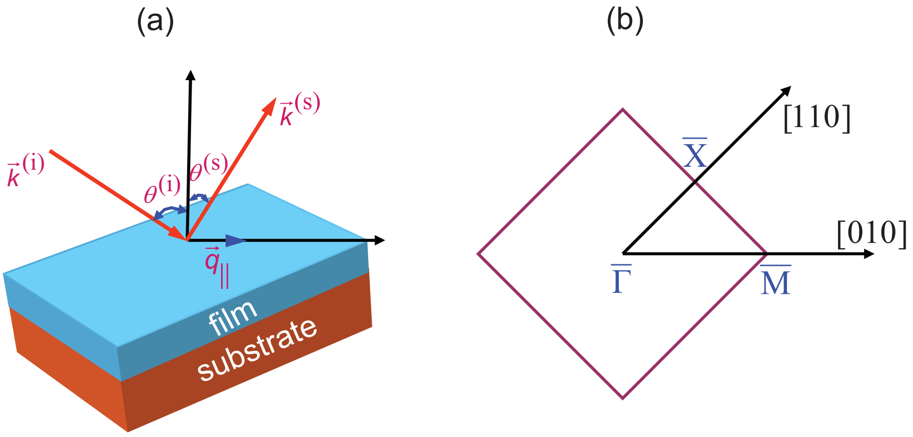
(a)
$\vec{k}^{(i)}$
$\vec{k}^{(s)}$
$\theta^{(i)}$
$\theta^{(s)}$
$\vec{q}_{\|}$
film
substrate
(b)
[110]
[010]
$\overline{X}$
$\overline{\Gamma}$
$\overline{M}$

Figure 4.3: (a) Schematic illustration of the scattering geometry used in our experiments. For all measurements, the angle between $\vec{k}^{(i)}$ and $\vec{k}^{(s)}$ is kept constant at 90°. (b) Surface Brillouin zone of an fcc (100) surface marking the high symmetry directions $\overline{\Gamma}\,\overline{X}$ and $\overline{\Gamma}\,\overline{M}$.

sample. The angle between the incident and the scattered beam is kept constant at 90° in the measurements. The wave vector parallel to the surface is given by

$$q_{\|} = -\Delta \mathrm{K}_{\|} = k^{(\mathrm{i})} \sin(\theta^{(\mathrm{i})}) - k^{(\mathrm{s})} \sin(\theta^{(\mathrm{s})}) \tag{4.1}$$

$\Delta \mathrm{K}_{\|}$ is the change of the wave vector parallel to the surface. The required $\Delta \mathrm{K}_{\|}$ is achieved by rotating the sample by an angle $\Delta\theta$ around an axis vertical to the scattering plane and is given by

$$\Delta \mathrm{K}_{\|}/\text{Å}^{-1} = \sqrt{2m/\hbar^2}\left[\sqrt{(E_0 - \hbar\omega)/\mathrm{eV}}\sin(45^\circ + \Delta\theta) - \sqrt{E_0/\mathrm{eV}}\sin(45^\circ - \Delta\theta)\right] \tag{4.2}$$

where E_0 is the incident electron energy and $\hbar\omega$ is the energy of the spin wave. For achieving positive $\Delta \mathrm{K}_{\|}$, the sample is rotated toward the incoming beam resulting in more normal incidence, whereas, for negative $\Delta \mathrm{K}_{\|}$ the sample is rotated away from the beam resulting in more grazing incidence of the beam. The spin wave measurements are performed by varying $\Delta \mathrm{K}_{\|}$ and recording the energy loss spectrum for each $\Delta \mathrm{K}_{\|}$. Since the spin wave energy $\hbar\omega$ is small ($\approx 0.05 - 0.2\,\mathrm{eV}$) compared to the incident electron energy ($6 - 7\,\mathrm{eV}$), the $\Delta \mathrm{K}_{\|}$ mentioned in individual spectra in the remaining chapters of the thesis are calculated neglecting the $\hbar\omega$ term in Eq. (4.2). However, the figures representing the properties of spin waves, like dispersion and widths are constructed with the precise $\Delta \mathrm{K}_{\|}$ obtained with the $\hbar\omega$ term in Eq. (4.2). The surface Brillouin zone (SBZ) of an fcc(100) surface is shown in Figure 4.3(b) indicating the high symmetry directions. The spin waves are probed with wave vector transfers along particular directions depending on the azimuthal orientation of the sample. The [011] direction corresponds to the $\overline{\Gamma}\,\overline{\mathrm{X}}$ direction and the [010] direction corresponds to the $\overline{\Gamma}\,\overline{\mathrm{M}}$ direction in the SBZ. The Brillouin zone boundary at the $\overline{\mathrm{X}}$-point and the $\overline{\mathrm{M}}$-point are at $\sqrt{2}\pi/a_0$ (1.23Å^{-1}) and $2\pi/a_0$ (1.74Å^{-1}), respectively with $a_0 = 3.61$Å the bulk lattice constant of copper.

4.2.3 Data evaluation procedure

A sample spin wave spectrum measured on an 8 ML cobalt film on a Cu(100) surface for wave vector transfer of $\Delta \mathrm{K}_{\|} = 0.267\text{Å}^{-1}$ along the [011]-direction is shown in Fig. 4.4(a). To achieve this wave vector transfer, the sample is rotated by an angle of 8° towards the incoming beam with respect to specular reflection. The primary beam energy is $E_0 = 7$eV. The spectrum is measured with a data accumulation time of 6 s in 1 meV intervals. The full width at half maximum (FWHM) of the diffuse elastic line is about 7 meV. The intense peak centered at zero loss energy is the quasielastic peak due to the electrons which have not suffered any energy loss during scattering but have scattered diffusely because of the surface disorder. The peaks at 27 meV and −27 meV (marked 1 in Fig. 4.4 (a)) correspond to the spin wave creation (energy loss) and spin wave annihilation (energy gain) peaks respectively.

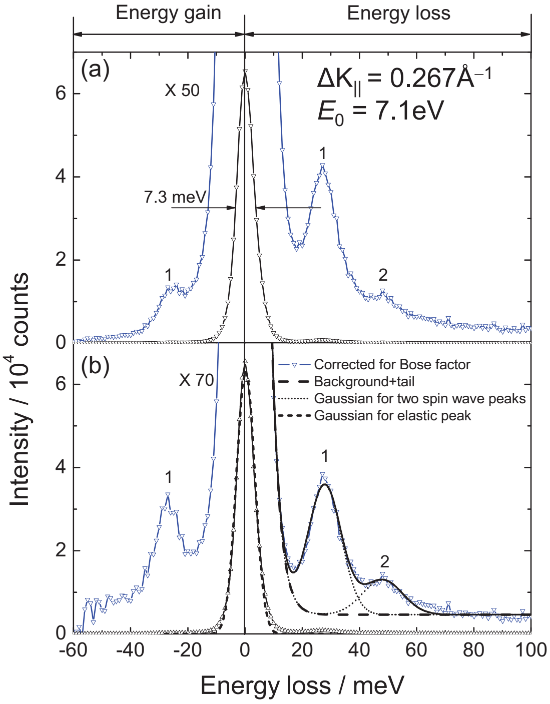

Figure 4.4: (a) Energy loss spectrum of spin waves measured for an 8ML pseudomorphic Co film on Cu(100) for momentum transfer $\Delta K_{\|} = 0.27\text{Å}^{-1}$ along the [011] direction. The FWHM of the diffuse elastic line is 7.3meV and the primary beam energy is $E_0 = 7.1$eV. Loss and gain peaks correspond to creation and annihilation of spin waves. (b) Data as in (a) after correcting for Bose occupation numbers (see text for details). The dashed line represents the fitting to a background consisting of the Gaussian tail of the elastic line and a constant. The dotted line represents the Gaussian fitting for the two spin peaks.

The creation and annihilation peaks are symmetric with respect to the diffuse elastic peak in accordance with Vollmer *et. al.* [17]. These authors have already suggested that the frequencies of spin waves in this system are independent of the sign of the wave vector. Unlike the case of phonons, time reversal symmetry is not obeyed by spin waves. An asymmetry of the loss and gain peaks is therefore possible for example through breaking of degeneracy of spin waves by the Dzyaloshinskii-Moriya interaction [68, 69]. Such an asymmetry in the spin wave dispersion was observed, for example, on 2 ML Fe/W(110) [23].

The relative probability of the spin wave creation and annihilation is given by the Bose factor, $n(\hbar\omega, T)$. The gain peak intensity is proportional to the number of occupied excitation states and is proportional to the Bose occupation number

$$n(\hbar\omega, T) = \frac{1}{\exp(\hbar\omega/k_{\mathrm{B}}T) - 1}.$$

The intensity on the energy loss side is proportional to $n(\hbar\omega, T) + 1$. Therefore, the ratio of the gain to loss peak intensity of a given excitation mode is given by $\mathrm{I}_{\mathrm{gain}}/\mathrm{I}_{\mathrm{loss}} = \exp(-\hbar\omega/k_{\mathrm{B}}T)$. The second mode at ≈ 46 meV is therefore visible only on the energy loss side (marked 2 in the figure) since $\exp(-\hbar\omega/k_{\mathrm{B}}T) = 0.17$ at

300 K. Moreover, because of the energy dependent weighting, peak 1 appears larger in relation to peak 2.

The energy, intensity and the width of the spin wave peaks are determined by applying a fitting procedure to the loss side of the spectrum. This is explained with the help of Fig. 4.4(b) which is the same as (a) but corrected for the Bose factor. For that purpose, the spectra are divided by $n(\hbar\omega, T)$ and $n(\hbar\omega, T) + 1$ on the gain and loss side, respectively. The spin wave spectra are first separated into a continuous background and the spin wave peak(s). The spin wave peak(s) are fitted with one or two Gaussian(s)

$$\propto \exp[-(E - E_{\mathrm{peak1}})^2/2s_1^2];\ \bigl(\exp[-(E - E_{\mathrm{peak2}})^2/2s_2^2]\bigr)$$

Here E is the energy loss, E_{peak1} (E_{peak2}) the peak position of the spin wave peak(s) and s_1 (s_2) the variance of the spin wave peak(s). The background consists of a Gaussian tail of the elastic peak and a constant count rate. The background is represented by dashed lines in (b). The dotted line represents the fitting of the two spin wave peaks by two Gaussians. The solid line represents the complete fitting function consisting of the background and the two Gaussians for the spin wave peaks.

The determination of the true width of the spin waves from experimental spectra requires the application of two correction terms namely, a correction for the broadening due to finite energy resolution and a correction for the finite wave vector resolution of the spectrometer. The first correction is straightforward as the width of the diffuse elastic peak has the shape of the instrumental energy resolution function. Hence the spin wave loss peak is to be unfolded from the elastic peak. The elastic peak is fitted with a Gaussian function (short dashed line in (b)) from which the variance s_{el} of the elastic peak is obtained. The determination of width is restricted to the first pronounced spin wave loss peak. The variance of the spin wave loss after correcting for the finite energy resolution is

$$s_p = \sqrt{s_1^2 - s_{\mathrm{el}}^2} \tag{4.3}$$

The effect of finite wave vector resolution of the spectrometer on the variance of the spin wave peak is described below.

Energy broadening of spin wave peak due to the sampled $q_\parallel$ range ("kinematic broadening")

Due to the finite acceptance angles of the lens/analyzer combination, the spectrometer inevitably samples spin waves within a finite range of α angles in the scattering plane [26]. A finite acceptance angle is equivalent to a finite range of wave vectors $q_\parallel$ probed by the spectrometer [26, 51]. The range of $q_\parallel$ transforms into a width of energies by virtue of the slope of the dispersion curve. This effect is called *kinematic energy broadening* [26]. Hence obtaining a quantitative account of the width of the spin wave energy loss requires the subtraction of the broadening due to the finite wave vector resolution. Etzkorn *et al.,* [21] calculated the range of acceptance angles in the scattering plane by measuring the specular intensity vs. spectrometer angle (α_{el}) and incorrectly [26] concluded that it had no effect on the width of the spin wave peak. The real acceptance angle is larger than α_{el} since during the rotation, the image of the monochromator sweeps across the entrance slit of the analyzer. The procedure for determining the acceptance angles is detailed in Section 3.3. Once the acceptance angles are known, the contribution of the scattering kinematics to the energy width in a spectrum can be calculated. Following [26, 51] one may assume a Gaussian for the distribution of angles accepted by the analyzer

$$P(\alpha) = \mathrm{e}^{-\frac{\alpha^2}{2s_\alpha^2}} \tag{4.4}$$

The natural width of the spin wave energy loss is also assumed to be a Gaussian

$$I(\omega) = I_0 \mathrm{e}^{-\frac{\left(\omega-\omega\left(q_\parallel\right)\right)^2}{2s_\omega^2}} \tag{4.5}$$

The intensity response function is then

$$R(\omega) = \int\limits_{-\infty}^{\infty} \mathrm{e}^{-\frac{\left[\omega-\omega\left(q_\parallel(\alpha)\right)\right]^2}{2s_\omega^2}} \mathrm{e}^{-\frac{\alpha^2}{2s_\alpha^2}} \mathrm{d}\alpha \tag{4.6}$$

As only small α angles contribute we can expand $\omega(q_\parallel)$ as

$$\begin{aligned} \omega(q_\parallel) &= \omega\left(q_\parallel(\alpha=0)\right) + \left.\frac{\partial\omega}{\partial\alpha}\right|_{\alpha=0} \alpha \\ &\equiv \omega_0 + c\alpha \end{aligned} \tag{4.7}$$

With the latter shorthand notation the response function becomes

$$R(\omega) = \mathrm{e}^{-\frac{(\omega-\omega_0)^2}{2s_\omega^2}} \int\limits_{-\infty}^{\infty} \mathrm{e}^{-\frac{c^2\alpha^2-2(\omega-\omega_0)c\alpha}{2s_\omega^2}} \mathrm{e}^{-\frac{\alpha^2}{2s_\alpha^2}} \mathrm{d}\alpha \tag{4.8}$$

The integral can be expressed in closed form to yield

$$\begin{aligned} &\int\limits_{-\infty}^{\infty} \mathrm{e}^{-\frac{c^2\alpha^2-2(\omega-\omega_0)c\alpha}{2s_\omega^2}} \mathrm{e}^{-\frac{\alpha^2}{2s_\alpha^2}} \mathrm{d}\alpha \propto \mathrm{e}^{\frac{(\omega-\omega_0)^2}{2s_0^2}} \text{ with} \\ &s_0^2 = s_\omega^2\left(1+\frac{s_\omega^2}{c^2 s_\alpha^2}\right) \end{aligned} \tag{4.9}$$

The final response function is then simply

$$\begin{aligned} R(\omega) &\propto \mathrm{e}^{-\frac{(\omega-\omega_0)^2}{2s_p^2}} \text{ with} \\ s_p^2 &= s_\omega^2 + c^2 s_\alpha^2 \equiv s_\omega^2 + \left(\left.\frac{\partial\omega}{\partial\alpha}\right|_{\alpha=0} \right)^2 s_\alpha^2 \end{aligned} \tag{4.10}$$

The derivative of ω with respect to α is split up into the part that comes from the dispersion and the part that comes from the dependence of $q_\parallel$ on α.

$$\left.\frac{\partial\omega}{\partial\alpha}\right|_{\alpha=0} = \left.\frac{\partial\omega}{\partial q_\parallel}\frac{\partial q_\parallel}{\partial\alpha}\right|_{\alpha=0} \tag{4.11}$$

where $\frac{\partial\omega}{\partial q_\parallel}$ is obtained from the experimental spin wave dispersion and $\frac{\partial q_\parallel}{\partial\alpha}$ is obtained from the scattering kinematics. From Eq.(4.1) one can write

$$\begin{gathered} q_\parallel(\alpha) = k^{(\mathrm{s})}\sin\left(\theta^{(\mathrm{s})}+\alpha\right) - k^{(\mathrm{i})}\sin\left(\theta^{(\mathrm{i})}\right) \\ \left.\tfrac{\partial q_\parallel}{\partial\alpha}\right|_{\alpha=0} = k^{(\mathrm{s})}\cos\theta^{(\mathrm{s})} \end{gathered} \tag{4.12}$$

Combining (4.3) and (4.10) one obtains the true variance of the spin wave peak after correcting for energy resolution and also for finite wave vector resolution

$$s_\omega = \sqrt{s_1^2 - s_{\mathrm{el}}^2 - \left(\frac{\partial\omega}{\partial q_\parallel}\right)^2 \left(k^{(\mathrm{s})}\right)^2 \cos^2\theta^{(\mathrm{s})}} \tag{4.13}$$

The full width at half maximum (FWHM) of the spin wave peak can be obtained from the variance using the relation

$$\mathrm{FWHM}_\omega = 2s_\omega\sqrt{2\ln 2} \tag{4.14}$$

4.3 Results of spin wave measurements

4.3.1 Experimental data

A series of spin wave spectra measured on eight monolayer cobalt films deposited on Cu(100) for a range of wave vector transfers $\Delta\mathrm{K}_\parallel$ along the [011]-direction is shown in Fig. 4.5. The primary electron beam energy is $E_0 = 7.1\,\mathrm{eV}$. The FWHM of the diffuse elastic peak representing the energy resolution is $7.3\,\mathrm{meV}$. The high resolution enables probing of spin waves down to $\Delta\mathrm{K}_\parallel = 0.235\text{Å}^{-1}$. The pronounced peak in (a) whose peak position increases from $20 - 60\,\mathrm{meV}$ with increasing $\Delta\mathrm{K}_\parallel$ corresponds to the surface spin wave mode. In the region of small wave vectors, i.e.

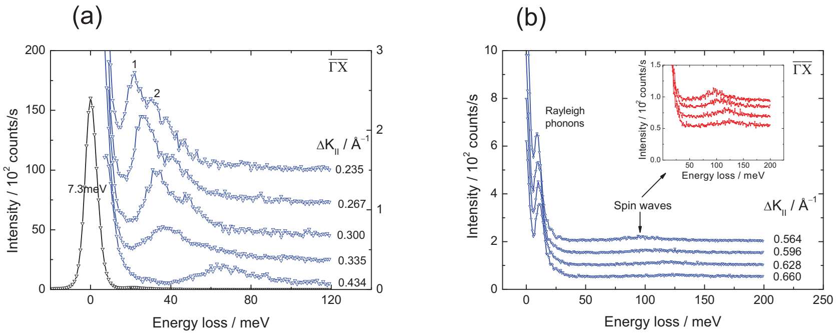

Figure 4.5: (a) Series of high resolution spin wave spectra measured along the [011]-direction. Spectra are corrected for the Bose occupation number. In the low $\Delta K_{\|}$ regime, two modes of spin waves are visible, marked 1 and 2. (b) Series of spectra measured for larger $\Delta K_{\|}$ under the same conditions as in (a). The Rayleigh phonons and spin waves are clearly distinguished. All spectra are measured with incident beam energy of 7.1 eV.

for $\Delta K_{\|} \leq 0.3\text{Å}^{-1}$, a second peak is clearly seen appearing as a shoulder to the first peak. The second peak represents a standing spin wave mode of the film as shown later. Fig. 4.5(b) shows spin wave spectra measured with the same energy resolution as in (a) however for larger wave vectors. At higher wave vectors, the spin waves becomes broad and the intensity also drops down rapidly. The inset shows the region of spin wave losses in higher magnification. The peaks at around 10 meV are due to the excitation of Rayleigh phonons. Rayleigh waves are the surface acoustic waves with polarization confined to the sagittal plane (which is the plane containing the substrate normal and the direction of propagation) [70]. The frequency of Rayleigh phonons depends linearly on the wave vector $q_{\|}$ for small $q_{\|}$ contrary to spin waves for which the energy dispersion is $\propto {q_{\|}}^2$ in the small wave vector regime.

It can be seen from Fig. 4.5 that the spin wave peak intensity drops down by a factor of 100 as $\Delta K_{\|}$ increases from $0.235 - 0.66\text{Å}^{-1}$. Therefore, to observe the weak spin wave signals at higher wave vectors, the spin wave measurements were performed with lower resolution to gain intensity. A series of spin wave spectra measured at higher wave vectors with an energy resolution of 34 meV is shown in Fig. 4.6. The spin waves are measured for both positive and negative wave vector transfers along the [011]-direction as shown in (a) and (b), respectively. The black dashed line is a guide to the eye connecting the peak positions of the individual spectrum. The spin wave energy increases as one moves into the Brillouin zone indicating their dispersion. The background seen in the spectra are partly due to the Stoner excitations [55,71]. At higher wave vectors, the continuum of these Stoner

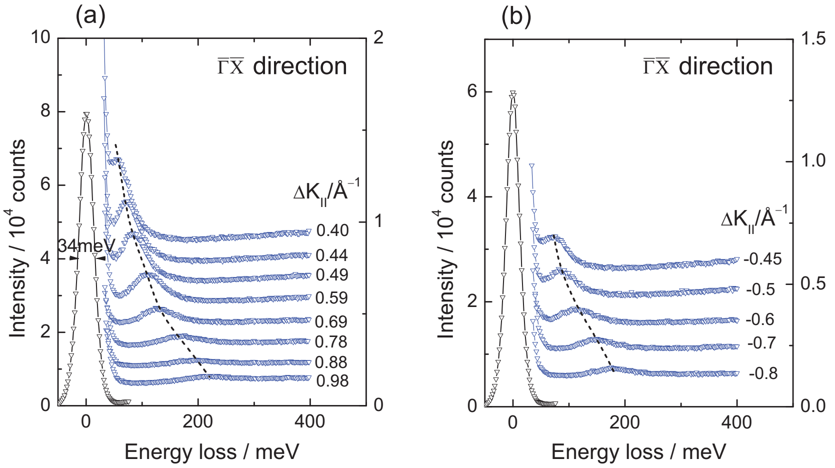

Figure 4.6: Selection of surface spin wave spectra from an 8ML Co/Cu(100) system for (a) positive wave vector transfers and (b) for negative wave vector transfers measured along the $\overline{\Gamma}\,\overline{\mathrm{X}}$ direction. The spectra are offset with respect to each other along the vertical axis. The impact energy on the sample is $E_0 = 7$eV. The elastic peak is for $\Delta \mathrm{K}_{\parallel} = 0.69\text{Å}^{-1}$.

excitations exhibit increased coupling to spin waves which imposes a strong *Landau damping* on the spin waves [56]. It is to be noted that in the case of negative $\Delta \mathrm{K}_{\parallel}$, the intensity of the spin wave is less than for the equivalent positive $\Delta \mathrm{K}_{\parallel}$. A possible reason could be due to the fact that for positive $\Delta \mathrm{K}_{\parallel}$, the sample is more perpendicular to the incoming beam. This implies that the area viewed by the analyzer is larger than the illuminated area, thus acquiring signal from a larger area of the sample which transforms to a increase in the intensity of the spectral features. For negative $\Delta \mathrm{K}_{\parallel}$, the reverse case holds true where the area viewed by the analyzer is smaller than the illuminated area.

The spin waves were also measured along the [010]- $\left(\overline{\Gamma}\,\overline{\mathrm{M}}\right)$ direction for both positive and negative wave vectors with low energy resolution of 34 meV. The corresponding series of spectra is shown in Fig. 4.7(a) and (b), respectively. The spin waves exhibit a similar trend as that observed along $\overline{\Gamma}\,\overline{\mathrm{X}}$-direction with the spin wave signal becoming broad and weak at higher wave vectors owing to Landau damping of spin waves.

Before proceeding with the results on further properties of spin waves (dispersion, intensity and width), the results on Rayleigh phonons (Fig. 4.5(b)) are briefly discussed here. Fig. 4.8 shows a selection of Rayleigh phonon spectra measured on 8ML Co/Cu(100) system along the [011]-direction with energy resolution of 7 meV. The

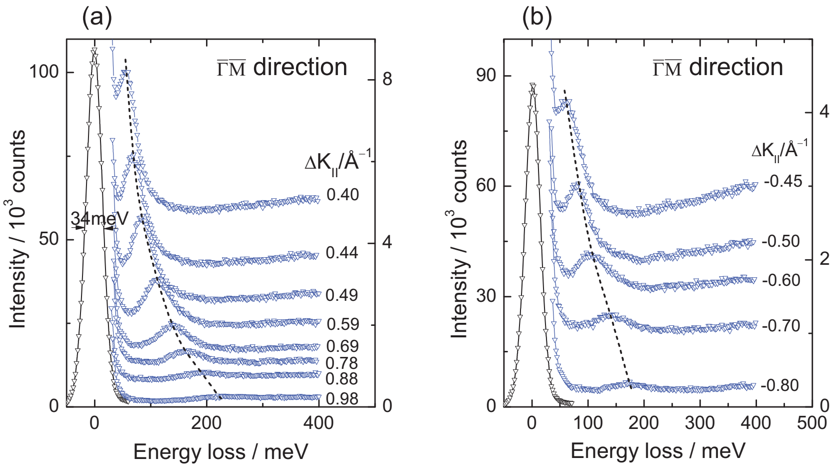

Figure 4.7: Selection of surface spin wave spectra from an 8ML Co/Cu(100) system for (a) positive wave vector transfers and (b) negative wave vector transfers measured along the $\overline{\Gamma}\,\overline{\mathrm{M}}$ direction. The impact energy on the sample is $E_0 = 7$eV. The elastic peak is for $\Delta K_{\|} = 0.69Å^{-1}$.

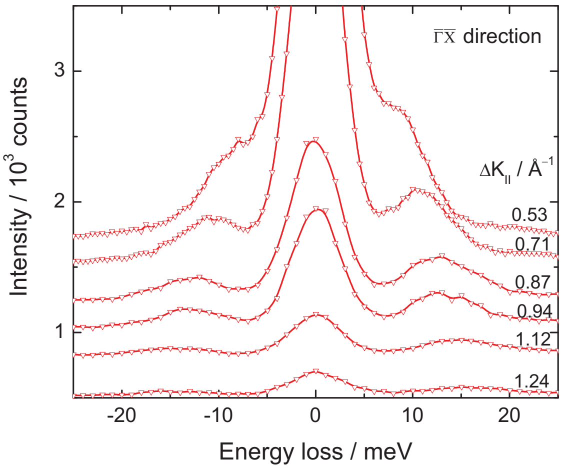

Figure 4.8: Series of EEL spectra showing the Rayleigh phonon excitation from an 8ML film of cobalt on Cu(100). The in-plane wave vector transfer is along the $\overline{\Gamma}\ \overline{\mathrm{X}}$ direction. The energy gain and loss peaks are due to phonon annihilation and phonon creation. The phonon energies are obtained by decomposition of the spectra into three peaks: energy gain, energy loss and diffuse elastic peaks. The incident beam energy is 7.1 eV and the energy resolution FWHM is 7.3 meV.

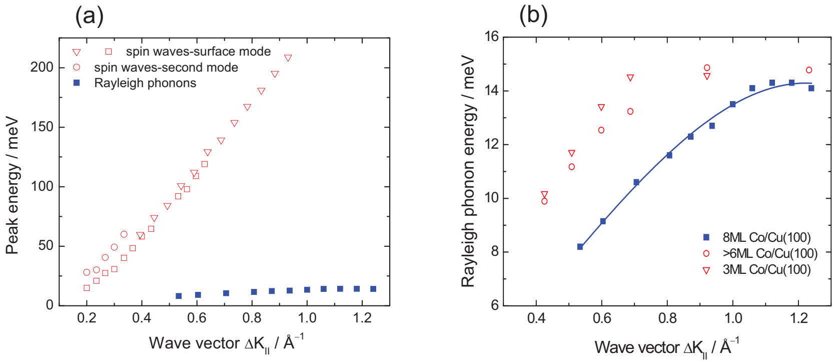

Figure 4.9: Dispersion of surface spin waves (open squares and triangles) and Rayleigh phonon dispersion (solid squares) measured for an 8ML fcc Co/Cu(100) system along the $\overline{\Gamma}\,\overline{X}$ direction. The circles represent the dispersion of the standing spin wave mode. The data points marked as solid and open squares and circles are obtained from high resolution spectra whereas the triangles are obtained from low resolution spectra. (b) Data of Rayleigh phonon dispersion (solid squares) compared with the data reported by Mohamed *et al.* [72] for various Co thickness (circles and triangles). The solid line is a guide to the eye.

peaks at positive energy loss are caused by the creation of the Rayleigh waves. The structures at negative energy loss are caused by the electrons which have annihilated a Rayleigh wave, the intensity of which is related to the corresponding loss peak by the Bose factor. An important feature of phonon dispersion is its inversion symmetry i.e. the frequency is independent of the sign of the wave vector. This is the consequence of the time reversal symmetry of the equation of motion. The creation and annihilation peaks are therefore symmetric with respect to the diffuse elastic peak. The energies of the Rayleigh phonons are determined by fitting energy loss, gain and the diffuse elastic peak to three overlapping Gaussian functions. The Rayleigh phonon energy at the zone boundary (1.23Å^{-1}) is about 14 meV, far less compared to the surface spin waves whose energy is about 220 meV for $\Delta K_{\parallel} = 1.0\text{Å}^{-1}$ and is hence easily distinguished from the spin waves.

4.3.2 Dispersion

The spin wave and Rayleigh phonon dispersion are constructed by plotting the energy of the individual peaks corresponding to each $\Delta K_{\parallel}$ from the series of figures shown above. The dispersion of spin waves and Rayleigh phonons along the $\overline{\Gamma}\,\overline{X}$ direction is shown in Fig. 4.9(a). The squares and triangles represent the data

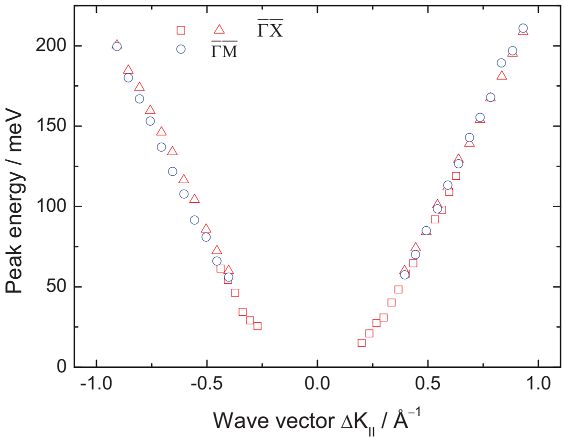

Figure 4.10: Spin wave dispersion measured with wave vector transfer $\Delta K_{\parallel}$ along $\overline{\Gamma}\,\overline{X}$ (squares and triangles) and along $\overline{\Gamma}\,\overline{M}$ direction (circles).

points for spin waves measured with high resolution (7.3 meV) and low resolution (34 meV), respectively. It can be seen that the data agree well with each other in the overlapping region. The circles represent the dispersion of the second mode of the spin waves.

The dispersion of Rayleigh phonons is represented by solid squares and is also shown separately in Fig. 4.9(b). The solid line is a guide to the eye with a fit of the phonon dispersion relation. As a comparison, the data of Rayleigh phonon dispersion reported by Mohamed *et al.* [72] is shown as open symbols. The triangles and circles represent the data for 3 ML Co and 6 ML Co films on Cu(100), respectively. It can be seen that the data of Mohamed *et al.* lie above the dispersion of an 8 ML Co film obtained in the present study. The data of Mohamed *et al.* were obtained from spectra with the same energy resolution as that used in the present study, albeit at a much higher impact energy (81 eV). The higher phonon energies in the previous study could be due to the presence of longitudinal surface modes [73] which may appear with similar intensity as Rayleigh modes depending on the impact energy.

The complete surface spin wave dispersion with data points for positive and negative wave vectors and for the $\overline{\Gamma}\,\overline{X}$ and $\overline{\Gamma}\,\overline{M}$ direction is shown in Fig. 4.10. The squares and triangles represent the spin wave dispersion along the $\overline{\Gamma}\,\overline{X}$ direction and circles represent that along the $\overline{\Gamma}\,\overline{M}$ direction. It is easily shown that in the absence of a Zeeman field and the Dzyaloshinskii-Moriya interaction and in the limit of small $q_{\parallel}$, the spin wave dispersion is quadratic in $q_{\parallel}$, hence, $\hbar\omega = Dq_{\parallel}{}^{2}$ where D is the exchange stiffness of the film. Because of the quadratic dispersion and the four fold symmetry of the cubic system, the spin waves are isotropic for small $q_{\parallel}$. It can be seen from Fig. 4.10 that the dispersion remains isotropic even for larger wave vectors, as far as one can tell in view of the width of the peaks.

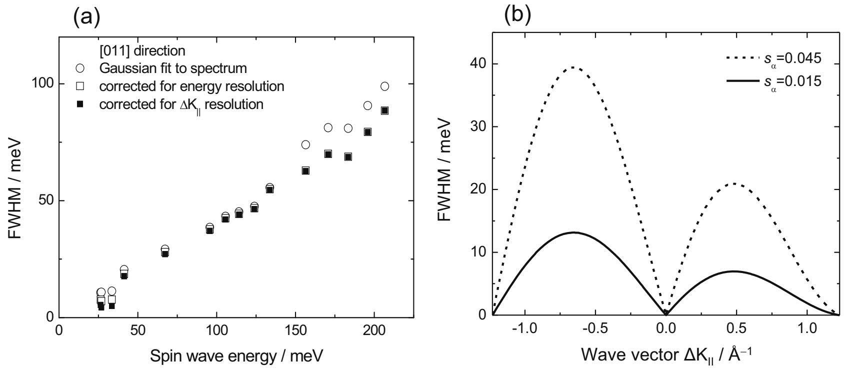

Figure 4.11: Full width at half maximum (FWHM) of the spin wave peaks vs. spin wave energy. Up to an energy of ≈ 130 meV ($\Delta K_{\|} = 0.66\text{Å}^{-1}$), the experimental spectra were obtained with high resolution settings. The higher energy spectra were obtained with low resolution settings. The circles represent the experimental FWHM obtained from a fitting procedure. The open- and solid squares represent the values after correction for energy resolution and after additional correction for finite wave vector resolution, respectively. (b) calculated FWHM of the spectra resulting from finite wave vector range probed by the spectrometer. The variance of the Gaussian distribution of the accepted angles for high resolution- and low resolution settings are $s_\alpha = 0.015$ and 0.045, respectively.

4.3.3 Energy width of spin waves

As mentioned before, the FWHM of the spin wave peak becomes broad as one progresses from the center into the Brillouin zone. The width of the spin wave peaks are determined by applying the fitting procedure described earlier. The width becomes very broad beyond $\Delta K_{\|} = 1.0\text{Å}^{-1}$ (see Fig. 4.6 and 4.7) so that no clear peak structure could be observed. Fig. 4.11(a) shows the FWHM of the spin wave peaks as a function of energy. The data points until $\Delta K_{\|} = 0.6\text{Å}^{-1}$ corresponding to a spin wave energy of 130 meV are obtained from high resolution spectra. The data points for higher energies are obtained from low resolution spectra. The FWHM obtained by fitting a Gaussian to the energy loss spectra is represented by open circles. The open squares represent the FWHM obtained after correcting for the finite energy resolution of the spectrometer as described in Section 4.2.3. The solid squares represent the FWHM after taking into account the additional broadening due to the finite $\Delta K_{\|}$ range probed by the spectrometer. The calculation of kinematic broadening from the dispersion of Co spin waves is treated in Ref. [51] and is outlined below:

As shown in Eq. (4.10), the additional broadening to the spin wave energy losses due to finite wave vector resolution is given by

$$s_p^2 = s_\omega^2 + \left(\frac{\partial\omega}{\partial\alpha}\right)^2 s_{\alpha^2} \tag{4.15}$$

where

$$\frac{\partial\omega}{\partial\alpha} = \frac{\partial\omega}{\partial q_\parallel}\frac{\partial q_\parallel}{\partial\alpha} \tag{4.16}$$

$\partial q_\parallel/\partial\alpha$ is obtained from Eq. (4.12).
To obtain $\partial\omega/\partial q_\parallel$ for the case of cobalt spin waves with wave vector along the $\overline{\Gamma}\,\overline{X}$ direction, the dispersion can be parametrized as (See Section 4.4)

$$\hbar\omega = 120\text{meV}\left(1 - \cos\left(\pi q_\parallel/q_{\text{BZ}}\right)\right) \tag{4.17}$$

Here, q_{BZ} is the wave vector at the boundary of the Brillouin zone which is 1.23Å^{-1}. Therefore,

$$\frac{\partial\hbar\omega}{\partial q_\parallel} = 120\text{meV}\pi/q_{\text{BZ}}\sin\left(\pi q_\parallel/q_{\text{BZ}}\right) \tag{4.18}$$

The variance of the distribution of acceptance angles α in the scattering plane for the high resolution settings and the low resolution settings are $s_\alpha = 0.015$ and 0.045, respectively. Using these values of s_α and the Equations (4.18) and (4.12), the FWHM resulting from kinematic broadening can be calculated. The result is shown in Fig. 4.11(b) for the high resolution and low resolution modes. The additional broadening due to kinematic effects is subtracted from the energy resolution corrected FWHM. The result is represented by solid squares in (a). It can be seen that the effect of kinematic broadening on the FWHM is very small especially at higher spin wave energies. The correction at lower energies is also not substantial due to the high resolution settings used for the measurement of the spectra. However, the usage of low resolution settings at small $\Delta\text{K}_\parallel$ will lead to a significant overestimation of the widths if kinematic broadening is not considered. See also Ref. [21], where the effect of kinematic broadening on the widths of spin waves was neglected.

4.3.4 Intensity of spin waves

Another property of interest is the dependence of spin wave intensity on the primary electron energy E_0. The spin wave intensities are drastically enhanced at lower energies with a maximum around $6 - 7\,\text{eV}$ for measurements along both the $\overline{\Gamma}\,\overline{\text{X}}$ and $\overline{\Gamma}\,\overline{\text{M}}$ direction as shown in Fig. 4.12(a) and (b), respectively. The measurements are shown for $\Delta\text{K}_\parallel = 0.7\text{Å}^{-1}$. The energy dependence of the intensity is in good agreement with that reported by Etzkorn *et al.* [21]. The peak in the energy dependence could be due to the increasing cross section for exchange scattering

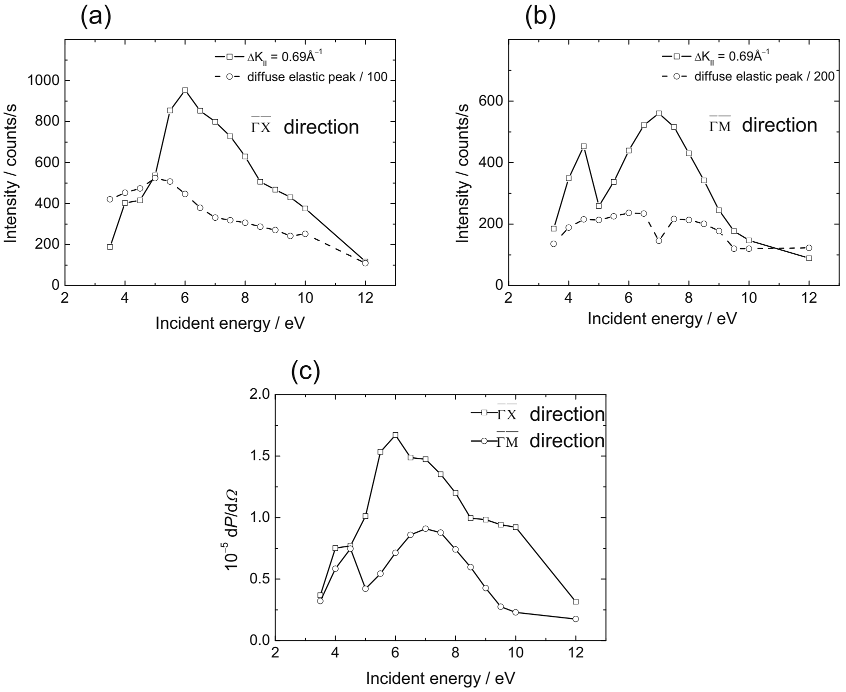

Figure 4.12: Energy dependence of the spin wave peak intensity and the diffuse elastic peak intensity of an 8ML Co film deposited on a Cu(100) surface for $\Delta K_{\parallel} = 0.69\text{Å}^{-1}$ measured along the (a) $\overline{\Gamma}\,\overline{X}$ direction and (b) $\overline{\Gamma}\,\overline{M}$ direction. The inelastic and the elastic peak intensities are depicted by squares and circles. (c) The spectral intensities converted into scattering probability per unit solid angle for inelastic scattering. The absolute cross section has a peak around $6 - 7\,\text{eV}$. The fine structures have their origin in scattering of electrons from surface resonances.

(which is responsible for spin wave excitations) at lower E_0 [9, 11] in combination with the falling sensitivity of the spectrometer at lower energies. However, the precise mechanism which is responsible for the peak in the energy dependence could not be determined in earlier measurements by Etzkorn *et al.* due to the lack of knowledge of the spectrometer properties i.e., the solid angle probed by the spectrometer and the transmission of the lens/analyzer system as a function of energy. The present spectrometer is completely characterized with respect to the solid angle and the transmission as described in chapter 3 and Ref. [26]. It was shown that the experimental intensity is related to the scattering probability according to

$$\mathrm{d}P/\mathrm{d}\Omega = \frac{I_{\mathrm{peak}} s_{\omega}}{I_{\mathrm{in}} T \mathit{\Delta\Omega} s_{\mathrm{el}}} \tag{4.19}$$

The spectral intensities of Fig. 4.12(a) and (b) are converted into the scattering probability per unit solid angle using this equation. The result for $\mathrm{d}P/\mathrm{d}\Omega$ is shown in Fig. 4.12(c). It can be seen that the absolute cross section for exciting spin waves is strongly enhanced at lower energies with a peak around $6-7\,\mathrm{eV}$ similar to the experimental intensities. The scattering probability decreases by more than a factor of three as the primary electron energy is increased (or decreased) by a few eV from 7 eV. It is to be noted from the figure that the intensity is not smoothly varying as function of electron energy. Rather, narrow oscillations and fine structures are visible in the intensity (and absolute scattering probability) vs. energy curve. These fine structures may have their origin in temporary trapping of incident or scattered electrons in the image potential in a region within a few Å above the surface [74, 75]. The captured electron is re-emitted after some time, longer than the time for direct scattering of electrons. The longer lifetime of electrons in the vicinity of the surface causes peaks in the scattering cross section depending on incident electron energy E_0 and wave vector $\Delta \mathrm{K}_{\parallel}$. These resonances can occur in both elastic and inelastic scattering events as indicated by the appearance of fine structures in both diffuse elastic peak and inelastic peak intensities in Fig. 4.12. The fine structures may exhibit dip or peak depending on the phase of the superposition of the resonant and non resonant scattering events [75].

4.4 Discussion

So far the experimental results of the elementary excitations on an 8 ML Co/Cu(100) system were presented. This section provides a detailed analysis of the spin waves and the associated properties. The first part of the section treats the surface spin waves and standing waves in the Heisenberg model. The second part of the section compares the experimental data to a theoretical study of spin waves that is based on the itinerant electron description of ferromagnetism in films and takes into account the realistic electronic structure of the film and the substrate.

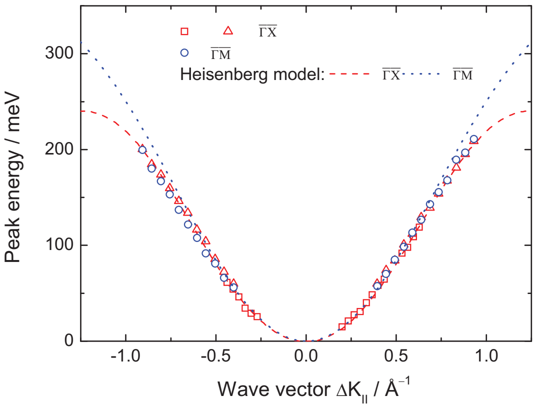

Figure 4.13: Peak positions of the spin waves for an eight monolayer cobalt film deposited on Cu(100) measured with in-plane wave vector transfer along the $\overline{\Gamma}\,\overline{\mathrm{X}}$ (squares and triangles) and $\overline{\Gamma}\,\overline{\mathrm{M}}$ (circles) directions. The dashed and dotted lines represent the surface spin wave mode of a semi-infinite fcc film derived from the Heisenberg model along the $\overline{\Gamma}\ \overline{\mathrm{X}}$ and $\overline{\Gamma}\ \overline{\mathrm{M}}$ directions, respectively. The JS value is taken as 15meV. The surface mode obtained for the $\overline{\Gamma}\,\overline{\mathrm{X}}$ direction represents a good fit to the data owing to the nearly isotropic nature of the experimental spin wave dispersion.

4.4.1 Spin waves in the Heisenberg model

In the case of magnetic layer systems, the common approach to understand the short wavelength spin waves is to use the Heisenberg model with localized spins attached to each lattice site. Although the method is commonly employed for 3d ferromagnets, one should bear in mind that the underlying physics of spin excitations in 3d-metals is very different from the one that is considered in the Heisenberg model. As we have seen in chapter 2, for an 8 ML film there are eight eigenmodes for each $q_{\|}$. Associated with each mode is an eigenvector which indicates the amplitude of the mode in a particular layer. The lowest eigenmode is the acoustic surface spin wave mode which involves the in-phase precession of spins in all layers, albeit with a decreasing amplitude the deeper the layer is in the stack. As shown in chapter 2, the surface spin wave dispersion of a semi-infinite fcc crystal in the nearest neighbor Heisenberg model is given by the following relations

$$\hbar\omega = 8JS\left(1 - \cos(q_{\|}a)\right) \tag{4.20}$$

$$\hbar\omega = 2JS\left(7 - 6\cos\left(\frac{q_{\|}a}{\sqrt{2}}\right) - \cos^2\left(\frac{q_{\|}a}{\sqrt{2}}\right)\right) \tag{4.21}$$

for wave vector transfers along the $\overline{\Gamma}\,\overline{\mathrm{X}}$ and $\overline{\Gamma}\,\overline{\mathrm{M}}$ directions of an fcc (100) surface, respectively. The experimental dispersion together with the surface spin wave dispersion given by the above equations is shown in Fig. 4.13. The dashed and the dotted lines represent the surface mode dispersion along the $\overline{\Gamma}\,\overline{\mathrm{X}}$ and $\overline{\Gamma}\,\overline{\mathrm{M}}$ direction within the Heisenberg model, respectively. The value of JS is taken as 15 meV. The high energy spin wave studies on the same system along the $\overline{\Gamma}\,\overline{\mathrm{X}}$ direction by Etzkorn *et al.* indicated an adequate fit to the experimental data using the same value of JS [17, 21]. This value of JS is in good agreement with the value of $JS = 14.7 \pm 1.5$ meV derived from a neutron scattering experiments on fcc bulk Co with 8% Fe to stabilize the fcc phase at room temperature [76]. According to the Heisenberg model, the surface spin waves should have higher energies along the $\overline{\Gamma}\,\overline{\mathrm{M}}$ direction compared to the $\overline{\Gamma}\,\overline{\mathrm{X}}$ direction with the difference becoming more pronounced at higher wave vectors (Fig. 4.13). However, this anisotropy is not seen in the experimental data. Rather, the surface mode dispersion along the $\overline{\Gamma}\,\overline{\mathrm{X}}$ direction represents a good fit to all experimental data.

The experimental dispersion of the surface mode observed along the $\overline{\Gamma}\,\overline{\mathrm{X}}$ direction together with the second mode is shown in Fig. 4.14(a). The solid and dashed lines are the acoustic mode and the first optic mode in the hierarchy of spin wave modes obtained from the Heisenberg model for an 8 ML fcc(100) slab along the $\overline{\Gamma}\,\overline{\mathrm{X}}$ direction. The JS is taken as 15 meV. A good agreement between the experimental data and the Heisenberg model is observed for both modes. The first optical mode given by the Heisenberg model represents the anti-phase combination of two surface modes of the eight layer film. The next standing mode, according to the Heisenberg model, has much higher energy which is shown by the blue dash-dotted line in the figure. The frequency of the standing wave mode at low wave vectors depends on the thickness of the film and on the exchange coupling at the surface. The dispersion of the antiphase surface mode as a function of layer thickness obtained from the Heisenberg model is shown in Fig. 4.14(b). It can be seen that the energies of the spin waves go up as the thickness is reduced. A careful study of these modes may therefore give access to the exchange coupling constants as a function of the number of layers.

4.4.2 Stiffness of spin waves

In the limit of very long wavelengths, the dispersion relation of the acoustic spin wave mode can be written as $\hbar\omega = D{q_\parallel}^2$ as mentioned before, with D the exchange stiffness of the film. By applying the above relation to the data of low wave vector surface spin waves (squares in Fig. 4.15(a)) the value of D is estimated as 346 meV Å^2 and is represented by the solid line in the figure. The standing wave modes are characterized by the additional perpendicular component of the wave vectors which assumes the values of $q_\perp \approx n\pi/d$, with d the film thickness and n an integer. The first order standing wave mode with $n = 1$ has a node in the center of the film and has a wavelength of twice the film thickness. For the case of an 8 ML cobalt film one obtains $\lambda/2 = 8 \times d$, $q_\perp = 2\pi/\lambda \approx 0.217\text{Å}^{-1}$ for the first standing wave mode. Therefore, the total wave vector for the standing wave mode is $q = \sqrt{q_\parallel^2 + q_\perp^2}$. The

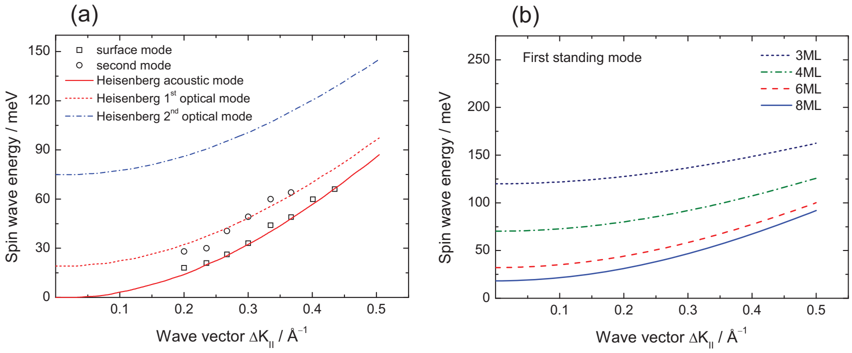

Figure 4.14: (a) The dispersion of the surface mode (squares) and the standing mode (circles) as obtained experimentally. The red solid and dashed lines represent the acoustic mode and the first optic mode along the $\overline{\Gamma}\,\overline{\mathrm{X}}$ direction obtained from the Heisenberg model with $\mathrm{JS} = 15\,\mathrm{meV}$. The first optic mode in the Heisenberg model represents the anti-phase precession of magnetic moments in the two surface layers. The next standing mode has far higher energy according to the Heisenberg model as indicated by the blue dash-dotted line. (b) The dispersion of the first standing wave mode as a function of layer thickness obtained from the Heisenberg model. The thinner layers exhibit higher energies.

data points of the standing wave mode energy as a function of the total q is shown as diamonds in Fig. 4.15(b). The data points can be well represented by the quadratic dispersion relation with the same value of stiffness obtained for the acoustic modes i.e. $D = 346\mathrm{meV}\mathring{\mathrm{A}}^2$ (blue solid line). For comparison, the data points of the acoustic modes are also shown.

4.4.3 Qualitative discussion of the width of spin waves

The FWHM of the experimental spin wave spectra as a function of spin wave energy and wave vector is shown in Fig. 4.16(a) and (b), respectively. The data fit well to a linear relation between the width and the energy(wave vector) of the spin wave peaks. Quite generally, the width of the spin wave losses reflects the lifetime of the spin wave before it decays into Stoner excitations. Because of the itinerant nature of the magnetism in 3d-metals, the damping of spin waves is quite severe, particularly near the zone boundary [77,78]. The linear relation between the FWHM and the spin wave energy (wave vector) reflects the approximate linear increase of the possibilities for a decay into Stoner excitation. The origin of the offset on the energy (wave vector) scale may be related to the spectrum of available Stoner excitations which in turn depends on details of the band structure. As shown in the schematic representation of Stoner excitation spectra and the spin wave dispersion

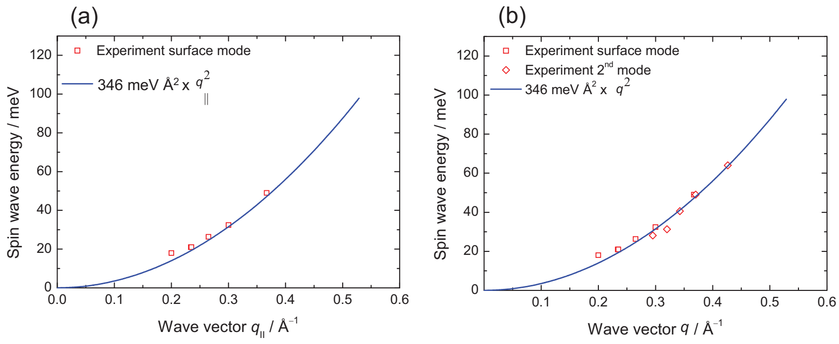

Figure 4.15: The surface spin waves are characterized by the wave vector parallel to the surface. The data for small wave vectors (squares in (a)) are fitted with a parabolic dispersion relation, $\hbar\omega = Dq_{\|}^2$ with $D \approx 346\,\mathrm{meV\AA}^2$ as shown by the solid line. The standing waves have an additional $q_\perp$ component and hence the total wave vector will be given by $q = \sqrt{q_{\|}^2 + q_\perp^2}$. A plot of the standing mode energy as a function of the total wave vector is shown in (b) as diamonds. It can be seen that the standing modes can be well represented by the same value of the stiffness as that of the acoustic mode (solid lines in (a) and (b)). For comparison, the data points of the acoustic mode are also shown (squares).

at surfaces (Fig. 2.2), the Landau damping does not set in until a critical wave vector is reached as one moves from the centre of the Brillouin zone. One notices from the band structure of fcc cobalt (Fig. 2.3) that the main channel for Stoner excitations with $q_{\|}$ along the [011] direction closes at a minimum wave vector of the order of $q_\mathrm{c} \approx 0.2\mathrm{\AA}^{-1}$ [38], which corresponds to a spin wave energy of ≈20 meV (Fig. 4.16(a)). This critical q_c is shown in the figure as an arrow pointing to the corresponding spin wave energy (wave vector). The closing of the decay channel at a finite energy explains why the linear slope is offset on the spin wave energy (wave vector) scale.

4.4.4 Spin waves in itinerant electron theory

In the Heisenberg model, the strict localization of spins on the atoms is equivalent to a flat, dispersionless d-band. Hence the electrons reside in d-bands of zero width. The spin waves are excitations out of the ground state and hence have infinite lifetimes [28]. However, in the case of 3d ferromagnets, the electrons reside in a series of energy bands where the width of the 3d bands is typically 4 eV. The spin waves

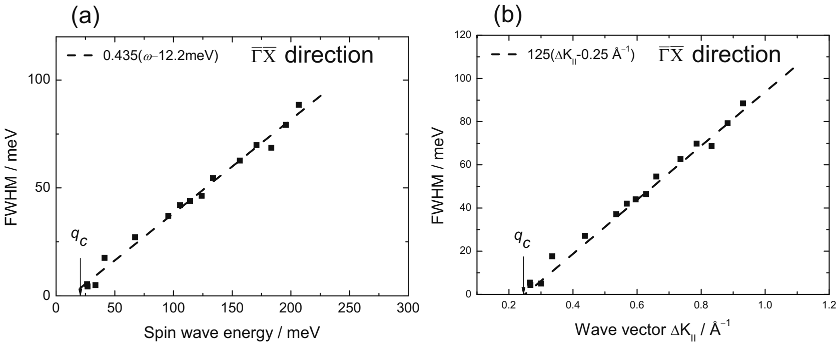

Figure 4.16: FWHM of the spin wave spectra as a function of (a) energy and (b) wave vector. The data are well fit by a linear relation, indicating increased coupling of spin waves to Stoner excitations as the energy (wave vector) increases. The linear fit approaches zero at a finite energy (wave vector) indicating the closing of the main decay channel for spin waves at a critical wave vector q_c [38].

in these systems are embedded in the Stoner continuum and are therefore strongly damped (save for small wave vectors, see discussion above). In order to get a correct description of spin wave excitations in these thin film systems, Mills and co-workers formulated a theory within the framework of an itinerant electron description [54–56, 79,80]. The theory was applied in the calculation of spin waves in thin films of bcc Fe on W(110) [56,79] and fcc Co films on Cu(100) [54,55]. The initial calculations were performed assuming bulk electronic structure of the film/substrate combination. In a recent work, Costa *et al.* have performed calculations for the 8 ML Co/Cu(100) system assuming thin film geometry in the calculation of the electronic structure [51]. The outline of the calculations elaborated in the above publications is as follows:

The first step in the calculation is the generation of the electronic structure of the itinerant magnetic film and the substrate. The electronic energy bands of the film and substrate are generated from an empirical tight-binding Hamiltonian. Nine bands (five d states and four sp complexes) are used to describe the electronic structure of the film and the substrate. The hybridization between the 3d states of the film and the 4sp states of the substrate is taken into account by appropriate hopping terms. The effective tight-binding parameters and the hopping integrals were extracted from density-functional theory (DFT) based calculations performed *ad-hoc* for the 8 ML Co/Cu(100) system. Ferromagnetic exchange splitting in the Co film is driven by Coulomb repulsion between the electrons within the 3d shell. The strength of the Coulomb interaction is also extracted from the DFT calculations [81]. The spin wave excitation spectra are obtained by calculating a quantity called the wave vector

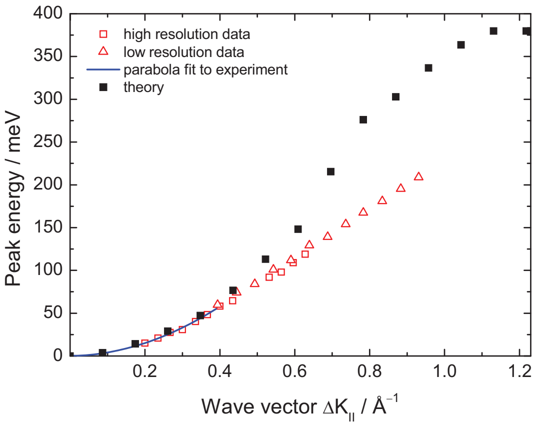

Figure 4.17: Comparison of the spin wave dispersion obtained from the calculations of Costa *et al.* [51] (solid squares) and the experimental data (open squares and triangles).

and frequency dependent transverse spin susceptibility $\left[\chi^{+,-}\left(\vec{q}_{\|},\omega\right)\right]$ [55, 56, 79, 82]. The spectral density is proportional to the imaginary part of this transverse susceptibility. If the layer index l is introduced, the spectral density provides a spin wave fluctuation spectrum as a function of frequency $\omega(\vec{q}_{\|})$ for a fixed wave vector $\vec{q}_{\|}$ on the particular layer l. Spin waves appear as peaks in this function with resonant frequency at $\omega\left(\vec{q}_{\|}\right)$ [56, 79]. It should be mentioned that the quantity of transverse susceptibility takes proper account of the spin wave region but underestimates the integrated strength of the Stoner transitions. A complete microscopic theory which takes proper account of spin waves and Stoner excitations requires the calculation of a different response function referred to by theorists as $\chi_{\mathrm{SPEELS}}\left(\vec{q}_{\|},\omega\right)$. Such calculations are at present developed only for bulk 3d ferromagnets [14, 83].

For the case of the 8 ML Co/Cu(100) system, Costa *et al.* calculated the spectral densities for the outermost layer for each value of $\vec{q}_{\|}$ [51]. The dispersion relation of spin waves is constructed by plotting the peak energies as a function of wave vector. The theoretical and the experimental spin wave dispersions are depicted in Fig. 4.17 by solid and open symbols, respectively. The wave vector transfer is along the [011]-direction. A good agreement between the experiment and theory is obtained for low wave vectors. The solid line is a parabola fit to the experiment from which the stiffness is obtained as 346 meV Å^2 as mentioned before. The exchange stiffness that results from a parabola fit to low wave vector energies in calculations is about 400 mev Å^2 which is only 12% higher than the experimental value. However, at higher wave vectors the spin waves from experiments are considerably softer than those obtained from calculations. The discrepancy at higher wave vectors is explained by Costa *et al.* as being due to the sensitivity of the spin wave spectra to small uncertainties in the determination of the electronic structure. It was noted that the short wavelength spin waves are very sensitive to the strength of the Coulomb

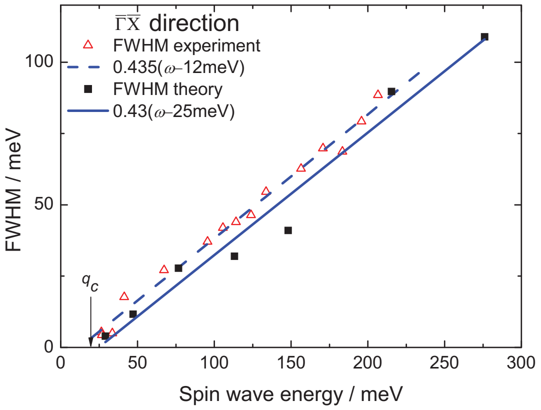

Figure 4.18: Comparison of the FWHM extracted from the spectral density calculations of Costa *et al.* [51] (squares) and the experimental FWHM (triangles). The data are well represented by a linear fit with a slight shift in the energy scale between the two fits. q_c represents the critical wave vector where Landau damping sets in.

interaction within the 3d shell [54]. The effective exchange interactions in itinerant 3d ferromagnets have very long ranges, with the interactions becoming smaller for distant neighbors. Hence, the long wavelength spin waves are less sensitive to small changes in the nearest-neighbor Coulomb interaction. However, small changes in the nearest-neighbor Coulomb interaction by as little as 20% lead to large variations of the short wavelength spin wave modes [54].

A comparison between the theoretical (solid squares) and experimental (triangles) line-widths as a function of spin wave energy is shown in Fig. 4.18. The theoretical line widths are extracted from the transverse susceptibility spectra for spin fluctuations [51]. The dashed and the solid line represent linear fits to the experimental and theoretical FWHM with a slope of 0.43. The data agree reasonably well with each other. The small shift in the energy scale between the two fits may not be significant. This could be attributed to the uncertainty in the determination of the experimental FWHM at small wave vectors from the fitting procedures. The good agreement of the calculated and experimental linewidth indicates the proper accounting of Landau damping in theory. The linear fit to the theoretical FWHM approaches zero for a finite spin wave energy similar to experimental line-width, reiterating the closing of the decay channel for Stoner excitations at a critical wave vector q_c as explained in Section 4.4.3.

4.5 Summary

The surface spin waves of eight monolayer fcc cobalt films were studied with high energy resolution. For small wave vectors, the spectra show a standing spin wave mode of the film in addition to surface spin waves. The standing wave mode is the anti-phase combination of the surface spin waves on the two surfaces of the film package. Hence the amplitude of that mode vanishes at the midpoint of the film. The surface spin waves were studied for wave vector transfers along the $\overline{\Gamma}\,\overline{\mathrm{X}}$ and $\overline{\Gamma}\,\overline{\mathrm{M}}$ directions of the Brillouin zone of the fcc(100) surface. The spin wave dispersion was found to be isotropic even for large wave vectors.

The widths of the spin waves were quantitatively studied by subtracting the broadening due to finite energy and wave vector resolution. The finite wave vector resolution of the spectrometer can result in substantial broadening of the energy width of spin waves especially when the low wave vector spin waves are probed with low energy resolution. A linear relationship between the line-width and spin wave energy (and wave vector) is found, indicating a linear increase in the Landau damping of spin waves. The linear fit between line width and energy (wave vector) approaches zero for a finite spin wave energy (wave vector) indicating the closing of a major decay channel for spin waves.

The conversion of spin wave intensities into absolute scattering probabilities indicated a maximum of the cross section for spin wave excitations for electron energies between 6 eV and 7 eV. The cross section decays rapidly on either side of this peak.

5 Search for spin waves on fcc Ni layers grown on Cu(100)

5.1 Introduction

The search for short wavelength spin excitations in nickel layers began 20 years ago with the advent of high resolution electron energy loss spectrometers [10, 84]. However, all attempts to observe surface spin waves in Ni layers by inelastic electron scattering have failed so far. Merely a broad band of low-lying Stoner excitations has been detected [84]. On the other hand, in bulk Ni the large wave vector spin waves are clearly observed in neutron scattering [85]. The failure to detect surface spin waves in Ni in the early electron scattering experiments could be, in part, ascribed to the fact that the spectrometers used were not of optimum design to study spin waves. The spectrometers used by Abraham and Hopster [84] and Kirschner *et al.*, [10] in their studies of magnetic excitations in Ni featured energy dispersive elements and lens systems which were not built following electron optical calculations for optimum transmission due to the unavailability of efficient numerical methods at that time. Early attempts were followed up later by Ibach *et al.*, using a high resolution spectrometer developed for studying vibrational excitations at surfaces [86]. With the development of our specifically designed high resolution spectrometer to study spin waves, we decided to revisit the issue of surface spin waves in nickel. The search for spin waves covers a wide range of fcc Ni layer thicknesses ($\approx 2-10$ ML) grown on Cu(100).

The chapter begins with the description of the sample preparation procedure and experimental details which is followed by the presentation of energy loss spectra measured for Ni layers of varying thickness on Cu(100). The final part of the chapter provides a discussion of the experimental results.

5.2 Preparation and characterization

Nickel on Cu(100) represents a good epitaxial system since they both have the same fcc crystal structure with a lattice mismatch of only 2.5 %. The growth of Ni on

Figure 5.1: MEED intensity oscillations of the specular beam for Ni grown on Cu(100) at room temperature. The intensity oscillations are obtained with an electron beam energy of 3 keV.

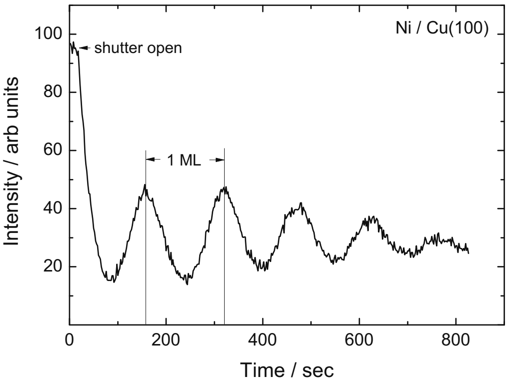

Cu(100) is pseudomorphic up to about 10 ML [87]. The lattice mismatch of 2.5% results in a small tetragonal distortion with elongated Ni-Ni distance in the film plane and contraction along the surface normal [88]. In general, for ultrathin films where the domain size is large compared to the film thickness, an in-plane easy axis of magnetization is expected owing to the shape anisotropy that results from the demagnetizing energy [1]. However, the Ni/Cu(100) system exhibits a reorientation of magnetization from in-plane to out-of-plane as the film thickness increases. Films thinner than seven ML exhibit in-plane magnetization with an abrupt transition to out-of-plane magnetization at higher coverages [87]. This reorientation could be explained by the combined effect of various competing anisotropies i.e., magnetoelastic, shape, surface and interface anisotropies. The magnetoelastic anisotropy results from the strain induced by the tetragonal distortion. For very thin films, the surface and interface anisotropies cause the magnetization to be in-plane. As the thickness increases, the magnetoelastic anisotropy in combination with the reduced influence of surface and interface anisotropies results in an out-of-plane magnetization for thicker films [65, 87, 89].

The Cu(001) single crystal substrate was cleaned and characterized as described in Section 4.2.1. Nickel films are deposited using electron beam stimulated evaporation from rods onto the Cu(001) substrate held at room temperature. It is known that under this growth condition, the films are stable against interdiffusion even for the thinnest films [65, 90]. The thickness of the deposited layer was calibrated by the observation of well defined oscillations in the intensity of the diffracted beam of 3 keV electrons. A typical MEED oscillation is shown in Fig. 5.1. The pseudomorphic growth of Ni films on Cu(100) was confirmed by the sharp $p(1 \times 1)$ LEED

---

[1] The demagnetizing energy density for perpendicular magnetization is $2\pi M^2$ (cgs units).

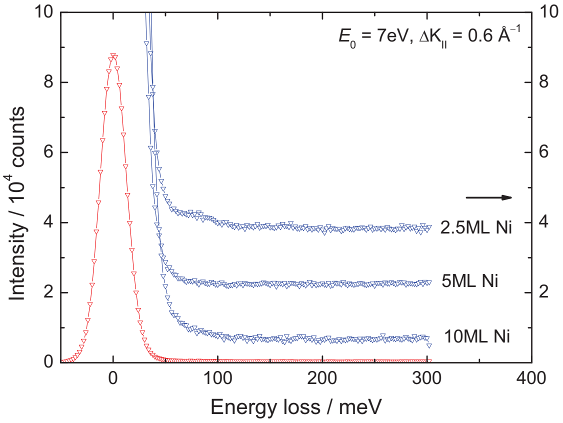

Figure 5.2: A series of energy loss spectra measured for varying Ni coverage on Cu(100). The wave vector transfer of $\Delta K_{\|} = 0.6\text{Å}^{-1}$ is along the [011]-direction. The spectra show no spin wave features in the loss regime.

pattern observed for these films. The spin wave measurements were performed for Ni film thicknesses ranging from 2.5 ML−10 ML covering the region of both in-plane and out-of-plane magnetization. The measurements were carried out along the [011] ($\bar{\Gamma}\,\bar{X}$) direction of the surface Brillouin zone (see Chapter 5). All spectra were measured at room temperature. The primary beam kinetic energy was set at 7 eV and the scattering angle was kept constant at 90°.

5.3 Electron energy loss spectra

In a picture where an electron scatter inelastically from an array of fluctuating spins with the substrate moments assumed as rigid entities, the excitation cross section scales as the square of the magnetic moment per atom. Since compared to cobalt the ground state magnetic moment of Ni is smaller, [2] one may expect the Ni spin wave signature to be weak. To increase the sensitivity the energy loss measurements were performed using a relatively low resolution. A series of energy loss spectra measured for Ni layers of thicknesses ranging between $2 - 10\,\text{ML}$ is shown in Fig. 5.2. The nominal wave vector transfer is $\Delta K_{\|} = 0.6\text{Å}^{-1}$. The FWHM of the quasi elastic peak which represents the energy resolution for diffuse scattering is about 30 meV.

The quantum energy of the bulk spin waves at $\Delta K_{\|} = 0.6\text{Å}^{-1}$ measured along the [111] and the [100] direction is about 130 meV. The number of nearest neighbors at the surface is 8 as opposed to 12 in the bulk. Based on a simple picture of the Heisenberg model, the reduced number of nearest neighbors leads to a reduction of spin wave energy at the surface, which will be about 85 meV for $\Delta K_{\|} = 0.6\text{Å}^{-1}$.

---

[2] The magnetic moment of bulk Ni is about $0.61\mu_\text{B}$ and that of Co is $1.72\mu_\text{B}$ [40].

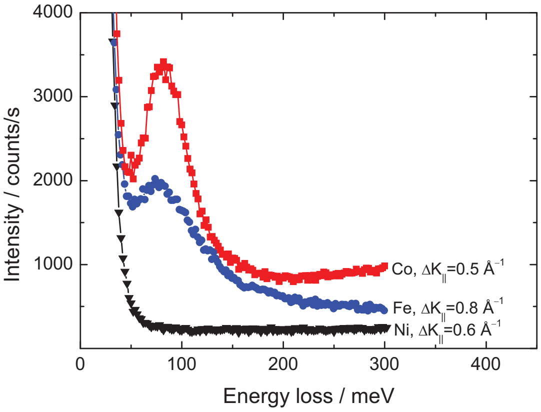

Figure 5.3: Comparison of energy loss spectra measured on Ni/Cu(100) with Co/Cu(100) and Fe/Cu(100). In the case of Fe and Co clear spin wave signals can be seen. The spin wave signal in nickel was theoretically predicted to be a factor of 10 smaller than in iron [8]. However, the absence of spin wave signature in nickel suggests that this ratio may be more than a factor of 10. See text for details.

As can be seen from Fig. 5.2, no signature of spin waves is found in the appropriate loss regime. Some possible reasons for this puzzling behavior are discussed below.

Nickel evaporated under UHV conditions exhibits a clear ferromagnetic response even below 2 ML [91]. The Curie Temperature T_C of the Ni/Cu(100) system is below room temperature for coverages less than 5 ML [65] with the T_C of a 3 ML film at 210 K. It is not surprising that one could not observe spin waves for a 2.5 ML Ni film at room temperature due to the loss of long range order above T_C [92]. The T_C of a 5 ML and a 10 ML films is 325 K and 485 K, respectively, with the remanent magnetization oriented parallel to the surface and out-of-plane, respectively. Nevertheless, even in this region, no spin-wave features are observed (Fig. 5.2).

Theoretical calculations show that the absolute cross section for exciting spin waves on Ni surfaces should be high enough to exhibit detectable features in EELS [8]. The excitation probability in Ni was predicted to be an order of magnitude lower than that for iron for impact energies investigated in the range of 30 eV to 150 eV. Since we have performed spin wave measurements on iron layers deposited on Cu(100) and found spin waves there (Chapter 7), it may be useful to compare the spectra of Fe and Ni. A series of spin wave spectra measured on 8 ML Co, 4 ML Fe and 5 ML Ni evaporated on Cu(100) substrate is presented in Fig. 5.3. The impact electron energy used for the measurements is between $6 - 7$ eV. The energy loss spectrum for Ni is shown for $\Delta K_\parallel = 0.6 \text{Å}^{-1}$ for which the spin wave energy is expected to be about 85 meV as noted before. The spin wave spectra for Co and Fe are shown for $\Delta K_\parallel = 0.5 \text{Å}^{-1}$ and 0.8Å^{-1}, respectively to be close to the energy of 85 meV. It can be seen that the surface spin waves in cobalt layers exhibit the highest intensity. Here we will concentrate on the comparison of Fe and Ni intensities with the theoretical prediction stated above. It can be seen from

Fig. 5.3 that the spin wave peak intensity in iron is about 1500 counts/sec. The intensity of the Ni spectrum at 85 meV is about 250 counts/sec and no hump is seen. If the intensity ratio of Fe and Ni is about a factor of 10 or slightly lower as predicted by theory [8], one might have still observed some weak structures at 85 meV. It is essential to note an important difference between the experiment and the theory. The calculations were performed for impact energies ranging from 30 eV to 150 eV whereas the experiments are performed with low impact energies of $6-7$ eV. The reason for choosing low energies in the experiments is two-fold. Firstly, it is known that at low energies (energies close to the Fermi energy), there is a strong enhancement of the exchange scattering cross section. The probability of the exchange process falls off rapidly at higher energies [9, 11]. Secondly, the energy versus intensity measurements in cobalt (see Fig. 4.12) as well as in iron revealed fine structure resonances induced by the surface image potential [74] at low energies with the peak intensity around $6-7$ eV. The intensity drops by a factor of 10 as the energy approaches 12 eV (Fig. 4.12).

The non-observability of spin waves in Ni could be due to the following reasons: The spin wave signals in Ni are very weak with an intensity ratio (to iron) of more than an order of magnitude smaller in the low impact energy regime examined. It is also possible that the image potential induced resonances, which exhibit maximum cross sections at $6-7$ eV for Co and Fe occurs at a different, as yet unknown, energy for Ni. One also cannot eliminate the possibility of the non-existence of such image potential induced structures for the excitation cross sections in Ni. A theoretical knowledge of the energy variation of the excitation cross sections covering a broad range of energies would benefit any further attempt to look for surface spin waves in nickel.

5.4 Summary

The electron energy loss spectra measured up to 10 ML coverage of fcc Ni on Cu(100) revealed no signature of spin waves. A quantitative comparison of the energy loss intensities in various 3d ferromagnetic systems indicates that the spin wave signals in Ni should be very weak i.e, weaker by more than an order of magnitude compared to iron.

6 Spin waves at interfaces

6.1 Introduction

A ferromagnetic (FM) film deposited on a nonmagnetic (NM) substrate is separated from the bulk of the substrate by a NM/FM interface. Magnetic multilayer systems consisting of layer sequences of FM/NM/FM and so forth give rise to multiple interfaces. Interface-induced magnetic properties are a key characteristic of ultrathin magnetic films. The important properties of magnetic multilayers with alternating magnetic and nonmagnetic layers are oscillating interlayer exchange coupling [1] and *giant magnetoresistance* (GMR) [2,3], which have a panoply of practical applications. The interfaces exert considerable influence on the electronic structure of the FM layers, which in turn determine their magnetic properties. In the case of Ni thin films grown on Cu(100), the Ni interface magnetism is known to be reduced due to the hybridization of Ni and Cu [93, 94]. Similarly, capping Co films grown on a Cu(100) substrate with a few monolayers of Cu is known to decrease the magnetic moment of cobalt [95,96]. Furthermore, the contact of a FM film with another metal surface (substrate or cap layer) provides additional damping mechanisms of the spin motions which are not present in the bulk materials. A frequently encountered mechanism of damping for long wavelength spin waves is referred to in the literature as "spin pumping". When a spin wave is excited in a 3d ferromagnetic layer, the spin motion results in a spin current normal to the interface between the film and the substrate as well as to the cap layer, if there is one [97, 98]. Thus the substrate and the capping layer act as spin sinks which relax the excited spins and provide an intrinsic damping of the magnetization in the ferromagnetic layer. The additional magnetic or nonmagnetic overlayers also provide an additional reservoir of Stoner excitations. The consequence of these damping processes is the large energy width ΔE of the interface spin waves. Since the energy width of the spin wave ΔE is $\hbar/\tau$, where τ is the lifetime of the spin wave, the larger energy width indicates a shorter lifetime of spin waves [28, 42, 79].

In this chapter, it is shown that by virtue of the finite penetration depth of low energy electrons, inelastic electron scattering can be conveniently employed to probe spin waves even at metal/metal interfaces. The effect of the additional magnetic or nonmagnetic overlayers on the energy and the width of the spin waves is studied experimentally. The system that we study is the surface of an eight monolayer (ML) fcc cobalt film grown on Cu(100) after additional deposition of $1-3$ ML of pseudomorphic nickel and up to 12 ML of copper. In both cases the intensity and the peak energy of the spin wave signal drops down considerably upon deposition of $1-3$ layers. Beyond the initial drop, the energy stays constant while the intensity decays exponentially with the thickness. It is shown that the exponential decrease in intensity is well characterized by the mean free path model for electrons in nickel and copper. The agreement between the experimental intensity and the mean free path model suggests that Ni and Cu layers do not contribute to the observed spin waves. Rather, the spin waves are localized at the Co side of the Ni/Co and Cu/Co interfaces.

The chapter is divided into three sections. Section 6.2 explains the procedure for quantitative analysis of the spectra. Section 6.3 presents the results of the spin waves after deposition of up to three layers of Ni on 8 ML Co/Cu(100). Section 6.4 comprises the results of spin waves after deposition of up to 12 layers of Cu on 8 ML Co/Cu(100).

6.2 Data evaluation procedure

The energy, intensity and widths of the spin wave losses are determined by applying a fitting procedure as explained in section 4.2.3. The spectra are separated into a continuous background, consisting of the Gaussian tail of the elastic peak and a constant count rate, and a Gaussian for the spin wave peak. The measured spectra are not corrected for the Bose factor as only the energy loss peaks are considered. All measurements are performed in a low resolution mode and are limited to high wave vectors i.e., $\Delta \mathrm{K}_{\parallel} \geq 0.4\text{Å}^{-1}$. The widths of the spin wave peaks obtained from the Gaussian fitting are corrected only for the finite energy resolution. The broadening of the widths due to finite wave vector resolution (kinematic broadening) is neglected. As shown in Section 4.3.3, the kinematic broadening is not substantial while probing higher $\Delta \mathrm{K}_{\parallel}$ with low resolution settings.

The intensity of the spin wave is proportional to the FWHM of the diffuse elastic peak as long as the intrinsic width of the spin wave is significantly larger than the width of the energy distribution of the specularly scattered electrons. For accurate comparison of the intensities of spectra with slightly different energy resolution, a quantity called "*specific intensity* I_{specific}" is introduced as a measure of the spin wave intensity. The "specific intensity" is obtained by dividing the count rate at the maximum of the spin wave Gaussian by the FWHM of the diffuse elastic peak. This quantity then serves as a comparison of experimental spectra among each other. The continuous background which is a mixture of spin wave contributions and Stoner excitations [54, 55] is disregarded in our analysis.

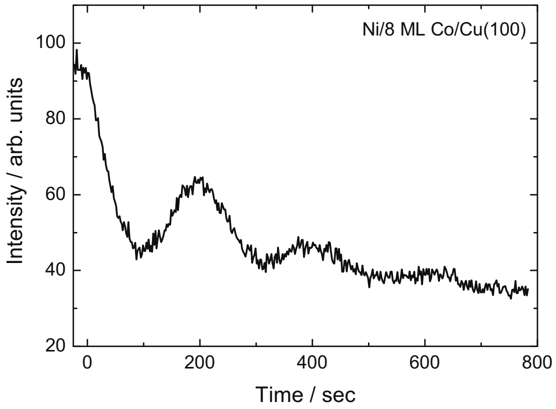

Figure 6.1: MEED intensity oscillations of the specular beam for Ni grown on 8 ML Co(100) at room temperature.

6.3 The Ni/Co(100) interface

6.3.1 Experimental details

The Cu(100) substrate was prepared by repeated cycles of Ar^+ sputtering followed by annealing until a sharp $p(1\times1)$ LEED pattern is observed (see Section 4.2.1). The Co(100) film was grown by depositing 8 ML Co on to the Cu(100) substrate held at room temperature. The Co deposition was followed by the deposition of Ni at similar temperatures. The thicknesses of the deposited layers were calibrated via medium-energy electron diffraction (MEED) oscillations. A typical MEED oscillation of the specular beam intensity observed for Ni layers deposited on 8 ML Co is shown in Fig. 6.1. The oscillations are less pronounced compared to the direct deposition of Ni on Cu(100) (See Fig. 5.1). This is due to the fact that the 8 ML Co film is already rough, which induces higher scattering of the electron beam that lowers the reflection of the specular beam. The amplitude of the MEED oscillations vanishes quickly as growth proceeds due to the increasing roughness of the growth front with time. Hence the first three oscillations were used for the calibration of the deposition rate of Ni. The thickness of the Ni layers for spin wave measurements ranged between $1-3$ layers. After preparation, the samples were transferred to the spectrometer chamber. The electron energy loss spectra indicated no traces of contaminants.

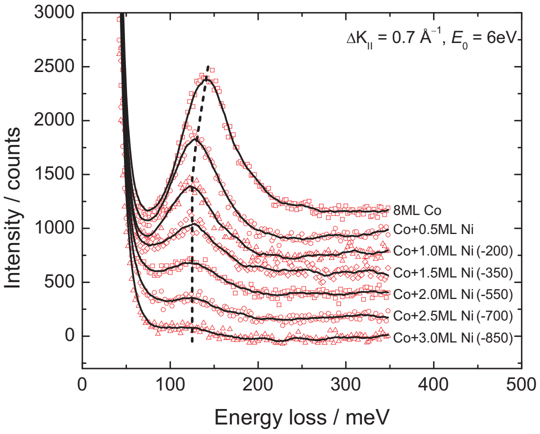

Figure 6.2: Series of spin wave spectra measured for $0-3$ ML Ni coverage on an 8 ML Co film. The wave vector transfer is $\Delta K_{||} = 0.7\text{Å}^{-1}$ directed along the [011]-direction. The spectra are vertically offset with respect to each other (number in brackets). The black solid and dashed lines serve as guides to the eye.

6.3.2 Spin wave spectra

A series of spin wave spectra measured for various Ni coverages on 8 ML Co is shown in Fig. 6.2. The wave vector transfer of $\Delta K_{||} = 0.7\text{Å}^{-1}$ is along the [011] direction. The incident electron energy is $E_0 = 6\,\text{eV}$. The angle between the incident and the scattered beam i.e., the scattering angle is kept at 90°. The spectra are measured with a data accumulation time of 2 s in 2 meV intervals. The spectra are vertically displaced with respect to each other by subtracting the counts as indicated in the figure. The black solid line is a 11 point gliding average to serve as a guide to the eye. The black dashed line connects the maxima of the loss peaks. The spectrum for the bare surface of 8 ML Co is shown in the upper spectrum. The spin wave peak energy is centered at about 140 meV. As the Ni coverage increases, the spin wave energy reduces until about 1 ML Ni where the loss peak is centered at ≈ 125 meV. Beyond 1 ML, the spin wave energy stays constant at this reduced value. The intensity of the spin wave shows a continuous reduction upon Ni deposition. The peak count rate reduces from a few hundred to a few tens on increasing the coverage from 0.5 ML to 3 ML. The experiments were repeated with freshly prepared surfaces to ensure reproducibility.

The peak energy and specific intensity I_{specific} of the spin wave losses as a function of nickel coverage is plotted in Fig. 6.3 by solid and open symbols, respectively. Squares and triangles represent the results of independently prepared samples. The estimated scattering in the spin wave peak energy for different independent measurements is indicated as error bars. Owing to the stability of the spectrometer, the differences in intensities of spin wave spectra of samples prepared on different days are smaller than 8%. The open circles mark the specific intensity for the case

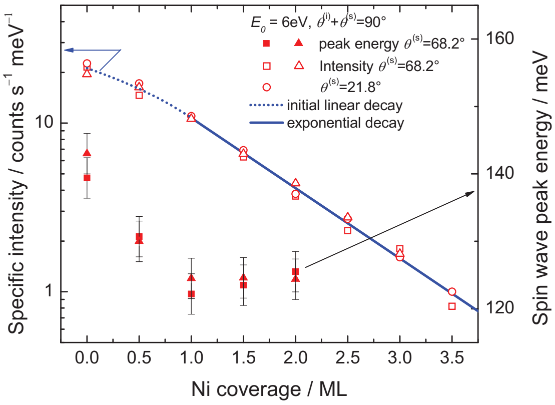

Figure 6.3: Specific intensity and peak energy of the spin wave energy loss as a function of Ni thickness for $\Delta K_{\parallel} = 0.7$Å. The energy shifts downward until a monolayer is completed and stays constant thereafter. The intensity exhibits linear decay until 1 ML coverage of nickel beyond which the intensity decays exponentially as represented by dotted and solid lines, respectively. Note the logarithmic scale for intensity.

when the angle of incidence and the angle of emerging beam are inversed so that the nominal wave vector $\Delta K_{\parallel} = -0.7\text{Å}^{-1}$. The specific intensity is the same for both cases within the limits of error. The blue line represents a fit to the observed specific intensities. The intensity exhibits a linear decrease up to 1 ML Ni coverage (dotted line) beyond which there is an exponential decay of intensity (solid line) (note the logarithmic scale on the y-axis).

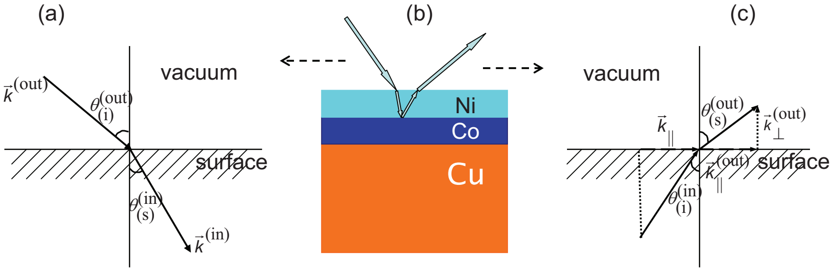

Figure 6.4: A scheme of the electron scattering process at the Ni/Co interface is shown in (b). The presence of the inner potential V_0 inside the Ni layer results in the refraction of electrons at the surface. The component of the wave vector parallel to the surface is conserved upon transmission through the surface as represented in (a) and (c).

The exponential decay of intensity beyond one monolayer coverage can be taken as a clue that the Ni layers do not contribute to the spin waves. The spin waves are localized at the Co/Ni interface. To verify this hypothesis, let us assume that the

Figure 6.5: Calculated density of states of Ni by Callaway and Wang [99]. The figure is taken from Ref. [39]. The exchange interaction shifts the electronic states of the majority spins and minority spins on the energy scale. The Stoner gap Δ marks the energy separation between the upper edge of the majority spin electrons and the Fermi energy.

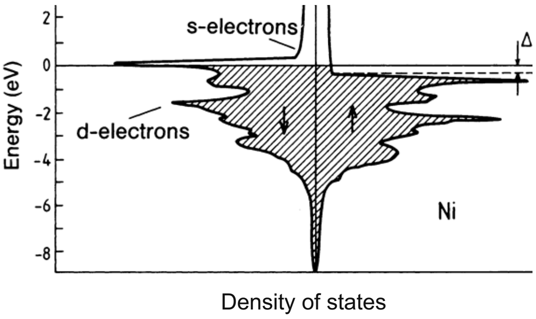

electrons first traverse the Ni layer without any energy loss on their way into the interface and secondly on their way out after exciting a spin wave at the interface. In that case, the change in the intensity of the spin wave dI is related to the change in the thickness dh of the Ni film by

$$\mathrm{d}I/I = -\mathrm{d}h/\lambda \tag{6.1}$$

Let N be the number of monolayers of Ni deposited. The spin wave intensity at the interface after deposition of N monolayers of Ni is then,

$$I_{\text{specific}}(N) = I_0 \exp(-\Lambda(N)/\lambda) \tag{6.2}$$

with $\Lambda(N)$ the path length inside the Ni layer and λ the mean free path. To estimate the path length inside the Ni layer, a knowledge of the path traversed by the electron beam inside the Ni layer is required. A scheme of an electron traversing through the Ni layer, its scattering at the Ni/Co interface and the travel of the scattered electron to the surface is shown in Fig. 6.4(b). The electron beam undergoes refraction at the interface due to the presence of the inner potential V_0. The inner potential is approximately the difference between the vacuum energy level and the bottom of the sp conduction band. The work function, which is the difference between the Fermi level and the vacuum level, is about 5 eV for Ni [52]. The bottom of the sp conduction band is at 9 eV from the Fermi level as can be seen from the density of states picture of Ni (see Fig 6.5). The figure is reproduced from [39]. Thus the inner potential V_0 of Ni is $\approx$ 14 eV. Owing to the 2D translational symmetry, the wave vector component parallel to the surface is conserved during transmission of electrons through the surface into the vacuum. This is represented in Fig. 6.4(a) and (c) for the path followed by the electrons inside the Ni layer before and after scattering at the interface. $\theta^{(\mathrm{in})}_{(\mathrm{i,s})}$ and $\theta^{(\mathrm{out})}_{(\mathrm{i,s})}$ are the angles of the incident and scattered beam with respect to the surface normal for electrons inside and outside the Ni layer. From the geometry defined in Fig. 6.4(a) and (c)

$$\vec{k}_{\parallel}^{(\mathrm{out})} = \vec{k}_{\parallel}^{(\mathrm{in})} \tag{6.3}$$

The values of $\vec{k}_{\parallel}^{(\mathrm{out})}$ and $\vec{k}_{\perp}^{(\mathrm{out})}$ for an electron on the vacuum side can be determined from the energy conservation requirement and is given by

$$k_{\parallel}^{(\mathrm{out})} = \sin\theta\sqrt{\frac{2m}{\hbar^2}E_0} \tag{6.4}$$

$$k_{\perp}^{(\mathrm{out})} = \cos\theta\sqrt{\frac{2m}{\hbar^2}E_0} \tag{6.5}$$

From (6.4) one directly obtains the wave vector component $k_{\parallel}^{(\mathrm{in})}$ inside the surface according to (6.3). However, the perpendicular component of the wave vector for an electron inside the Ni layer is altered due to the presence of the inner potential V_0. The $k_{\perp}^{(\mathrm{in})}$ component can be written as

$$k_{\perp}^{(\mathrm{in})} = \cos\theta\sqrt{\frac{2m}{\hbar^2}(E_0+V_0)} \tag{6.6}$$

Thus kinetic energy of the electron inside the solid will be larger than the energy of the electron in the vacuum far from the surface. Hence the angles $\theta_{(\mathrm{i})}^{(\mathrm{in})}$ and $\theta_{(\mathrm{s})}^{(\mathrm{in})}$ are smaller than the angles outside. The relation between polar angle inside and outside is

$$\theta_{(\mathrm{i,s})}^{(\mathrm{in})} = \arctan\left[\frac{k_{\parallel}^{(\mathrm{in})}}{k_{\perp}^{(\mathrm{in})}}\right] = \arctan\left[\frac{\sin\theta_{(\mathrm{i,s})}}{\cos\theta_{(\mathrm{i,s})}}\sqrt{\frac{E_0}{E_0+V_0}}\right] \tag{6.7}$$

The path length of electrons inside the Ni layer is therefore given by

$$\Lambda(N) = (a_0/2)N\left(\frac{1}{\cos\left(\theta_{(\mathrm{i})}^{(\mathrm{in})}\right)} + \frac{1}{\cos\left(\theta_{(\mathrm{s})}^{(\mathrm{in})}\right)}\right) \tag{6.8}$$

with a_0 the lattice constant of nickel.

A fit to the experimental specific intensity beyond 1 ML coverage with Eq. (6.2) and making use of equations (6.7) and (6.8) is shown as the blue solid line in Fig. 6.6. The value of the inner potential V_0 is taken as 14 eV as explained earlier. The value of the mean free path obtained from the fit is $\lambda = 5$Å.

In a theoretical paper, Hong and Mills have calculated the spin dependent inelastic mean free path of electrons for propagation in bulk Ni [47]. The calculations were performed for electron energies ranging from $1 - 15$ eV above the Fermi level.

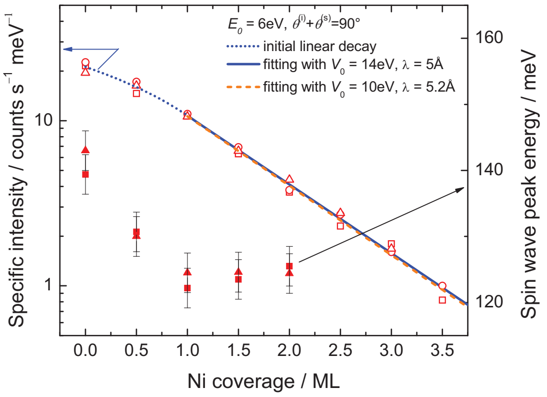

Figure 6.6: Data are the same as Fig. 6.3. The exponential decay of intensity is now described by the path length of electrons inside the Ni layer. A fit with the mean free path model assuming $V_0 = 14\,\text{eV}$ gives $\lambda = 5\text{Å}$ in good agreement with theory [47] (solid line). Assuming $V_0 = 10\,\text{eV}$ leads to only 5% increase in mean free path giving a value of $\lambda = 5.2\text{Å}$ and is represented by the dashed line.

The calculations indicate large spin asymmetry in the mean free path within a few eV of the vacuum level [47]. The vacuum level is roughly 5 eV above the Fermi level. The large spin asymmetry is attributed by the authors to the strong spin-flip scattering suffered by minority spin electrons from excitations in the d-band. Thus the inelastic mean free path of minority spin electrons is very small for energies close to the vacuum level. The inelastic mean free path is found to be about 9Å for spin-up electrons and 4.5Å for spin-down electrons at the vacuum level for Ni. The asymmetry decreases as the kinetic energy of the electrons increases above the vacuum level. The inelastic mean free path for electrons with energy 11 eV above the Fermi level (6 eV above the vacuum level) is about 5.5Å for spin-up electrons and 5Å for spin-down electrons. This is the energy at which the spin wave measurements presented in this Chapter were performed. The measurements are however performed with an unpolarized electron beam. Hence, one is interested in the spin-averaged mean free path for electrons which is about 5.25Å according to the calculations of Hong and Mills [47]. This value is quite consistent with the value of 5Å obtained from the mean free path fit to the experimental data obtained above.

The assumption of 14 eV for V_0 is not critical. Assuming e.g. $V_0 = 10\,\text{eV}$ results in only 5 % increase of path length. A fit with $V_0 = 10$ eV is shown by the orange dashed line in Fig. 6.6 which gives $\lambda = 5.2\text{Å}$.

The good agreement between the mean free path model and the experimental intensities demonstrates that the observed spin wave is indeed an interface mode. The electrons lose their characteristic energy at the Co side of the Co/Ni interface. Moreover, the intensities are the same for positive and negative wave vectors (i.e., angle of incoming and outgoing beam inversed). This is expected since both path in and path out in the Ni layer lead to decay of intensity, confirming further that the spin waves stem from the interface. This conclusion moreover gains support from

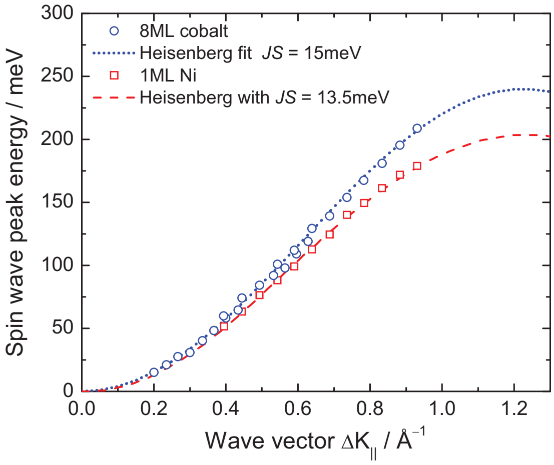

Figure 6.7: Dispersion of the 8 ML Co/Cu(100) surface spin waves (circles) and the 1 ML Ni/8ML Co/Cu(100) interface spin waves (squares). The wave vector transfer is along the [011]-direction. The dotted and dashed lines are fit to the Heisenberg model with different JS values to match the experimental data.

the fact that neither Ni layers deposited on Cu (Chapter 5) nor thicker Ni films on Co/Cu(100) show any sign of spin waves. Furthermore, we can exclude that the Ni layer at the interface directly contributes to the spin waves since otherwise the mean free path obtained from the experimental data would have come out at a much shorter value.

6.3.3 Dispersion of Ni/Co interface spin waves

Figure 6.7 compares the dispersion of a 1 ML Ni/Co interface spin waves (open squares) with the surface spin waves of an 8 ML Co film (solid circles). The dotted and dashed lines represent the surface mode of a semi-infinite film along the [011]-direction obtained from the Heisenberg model (see Chapter 2) which is given by the following equation

$$\hbar\omega = 8JS(1 - \cos q_{\|} a_0) \tag{6.9}$$

The coupling constants are taken as $JS = 15\,\text{meV}$ and $13.5\,\text{meV}$, respectively, to fit the surface mode and the interface mode. These fits are to be considered merely as an interpolation scheme to heuristically describe the experimental data on the dispersion curve. The energies of the interface spin waves are down shifted from bare Co spin waves. One can imagine the shift as the consequence of stronger Landau damping provided by the additional Ni overlayer, which leads to the renormalization of spin wave energies. The spin wave peak energy in that case will reflect not only the product of spin S and exchange coupling J as in the Heisenberg model but also the strength of the Landau damping. To explore this possibility, the widths of the spin wave peaks are determined and analyzed in the next section.

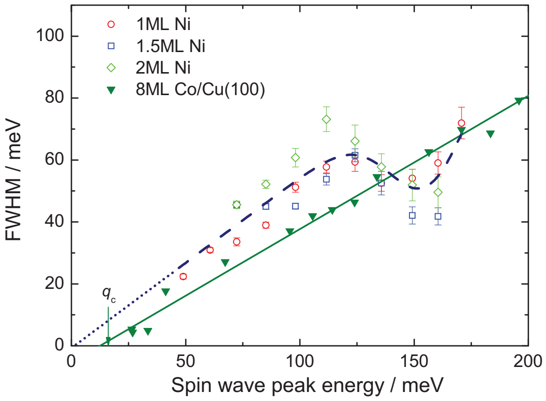

Figure 6.8: FWHM of spin wave energy loss signals as a function of spin wave peak energies for the 8 ML Co/Cu(100) system (solid symbols) and the Ni/Co/Cu(100) system (open symbols). The solid line is a linear fit to the Co data. The dashed line a fit to roughly represent the mean data of the FWHM of the interface spin waves composed of a linear and a Gaussian function. The FWHM of the interface spin waves exhibit a dip at higher energies indicating reduced damping which could be a consequence of the changes in the interface electronic structure.

6.3.4 Widths of the Ni/Co interface spin waves

The full widths at half maximum (FWHM) of the Ni/Co interface spin waves (obtained from the fitting procedure) as a function of spin wave energy are shown as open symbols in Fig. 6.8. The data of 1 ML Ni, 1.5 ML Ni and 2 ML Ni are depicted by circles, squares and diamonds, respectively. The solid triangles are the line widths for the bare cobalt film reproduced from Fig. 4.16(a). The solid line is a linear fit to the bare Co data (Fig. 4.16). The dashed line is a fit to roughly represent the mean of the interface spin wave widths composed of a linear and a Gaussian function. The FWHM of the interface spin waves exhibit a peculiar feature. In the region of low energies (wave vectors), the interface spin wave widths are higher than the bare cobalt spin wave widths. The linear relation in the low energy regime extrapolates to zero width at zero spin wave energy. This increase in width could be attributed to the increased Landau damping of spin waves with an additional (magnetic) overlayer. As we shall see later a similar behavior is observed for Cu overlayers (Section 6.4.4). At higher spin wave energies however, the widths of the interface spin waves exhibit a dip at about 150 meV corresponding to $\Delta K_{\parallel} = 0.84\text{Å}^{-1}$. It is interesting to note that in the narrow region of spin wave energies of about 140 – 170 meV ($\Delta K_{\parallel} = 0.75\text{Å}^{-1} - 0.9\text{Å}^{-1}$), the FWHM of the interface spin waves are actually lower than the width of the bare Co spin waves. The reduction is observed for the entire range of Ni overlayer thicknesses investigated, although it may differ in detail. The spin wave peak positions and widths could be determined only until $\Delta K_{\parallel} \approx 0.9\text{Å}^{-1}$ (and energy of $\approx$ 170 meV), beyond which the

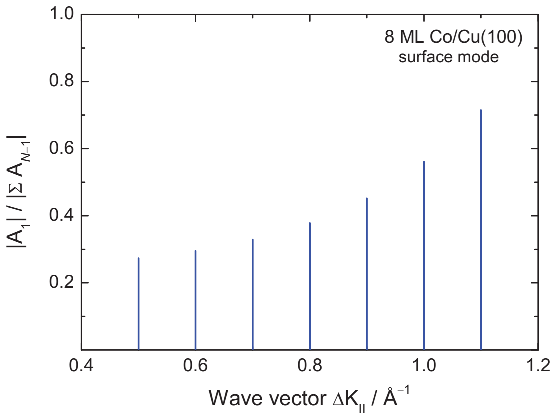

Figure 6.9: The weighted amplitude of the acoustic mode on the surface layer of an 8 ML fcc film as a function of wave vector, obtained from the Heisenberg model. The amplitude increases as wave vector increases indicating localization of spin waves on the surface layer.

spin waves become very broad and asymmetric. Hence, one could not ascertain the behavior of the FWHM near the zone boundary.

The reduction in width points to the fact that the damping of spin waves on capping Co films with Ni layers is lower than that for the bare Co surface. Despite the reduced damping, the spin wave energies exhibit a continuous down shift from the bare Co spin wave dispersion in the entire range of wave vectors investigated (Fig. 6.7). This indicates that the observed shift in energies cannot be explained by the effect of Landau damping.

6.3.5 Electronic and magnetic structure of the Ni/Co interface

The reduced damping of interface spin waves compared to the bare Co spin waves requires that the addition of Ni capping imposes changes in the electronic structure of the cobalt film. The observed deviation from the linear behavior of the FWHM at higher wave vectors may be a consequence of the modification of the electronic structure of the cobalt layer at the interface only. This hypothesis gains support from the fact that the penetration depth of spin waves decays rapidly at higher wave vectors. As shown chapter 2 (Eq. (2.28)), the decay factor for surface spin waves in the Heisenberg model for thick films is given by $\exp(-\alpha a) = \cos\left(q_{\|}a\right)$. This means the amplitude of the surface mode penetrates throughout the film when its wavelength parallel to the surface is long compared to the lattice constant. At larger wave vectors, the amplitude is more localized to the surface. Fig. 6.9 shows the relative weight of the amplitude at the interface as a function of the wave vector calculated from the Heisenberg model. It can be seen that as one moves into the

Brillouin zone, the relative weight increases. This substantiates the assumption that only the surface electronic structure of Co is changed by the Ni overlayer.

Dhesi *et al.* reported a marked change in the Ni/Co interface electronic and magnetic structure based on a series of measurements using x-ray absorption spectroscopy (XAS) and x-ray magnetic circular dichroism (XMCD) [100–102]. The modifications are significant for Ni films of thickness $\leq 2\,\mathrm{ML}$. It has been shown from XAS spectra that the Co d-state occupancy decreases and Ni d-state occupancy increases. This change in the d-occupation indicates redistribution of charge from Co to Ni d-states. The redistribution of charge would result in the change of minority and majority density of states of Co and Ni at the interface [101,102]. The change in the density of states would affect the interface magnetic moment. Dhesi and co-workers found an enhancement in the Co magnetic moment and reduction in the Ni magnetic moment on capping Co films with Ni from XMCD spectra [100,101]. The spin moment of Co was found to increase from $\approx 1.4\mu_{\mathrm{B}}$ to $1.9\mu_{\mathrm{B}}$ on capping 4 ML Co/Cu(100) with 1 ML of Ni [102]. The Ni spin moment on the other hand reduces to $0.18\mu_{\mathrm{B}}$ [101]. This clearly indicates the effect of Ni on Co magnetic structure.

Owing to the increased spin moment of cobalt one would expect an increase in spin wave energy rather than a downshift. However, one cannot exclude the possibility of a change in the exchange coupling constant J due to the charge transfer between the Co and Ni d-states. The modified exchange coupling could reduce the spin wave energies. The charge redistribution changes the exchange splitting and the density of states near the Fermi level of both Co and Ni at the interface. The modified electronic structure of Co at the interface may close some decay channels, reducing the damping of spin waves. For further understanding of the interface spin waves and their widths, calculations of the band structure and the combined density of spin-flip states of the Ni/Co interface are required.

6.4 The Cu/Co(100) interface

6.4.1 Experimental details

The cobalt and copper films were grown from high purity rods at room temperature on Cu(100) substrates. The Cu(100) substrates were prepared as described earlier (Section 4.2.1). The thickness of the Co film was 8 ML. The deposition rate for cobalt was calibrated via MEED oscillations as shown in Chapter 4. Although Cu films are widely studied in the literature as overlayers on FM films or sandwiched between two FM films, the details of the preparation procedures of Cu films are rarely discussed. Copper is a high vapor pressure material. The temperature for a vapor pressure of 10^{-4} Torr is $\approx 1020°\mathrm{C}$ which is close to the melting point of copper (1085°C). The range of heating power and flux at which Cu evaporates without

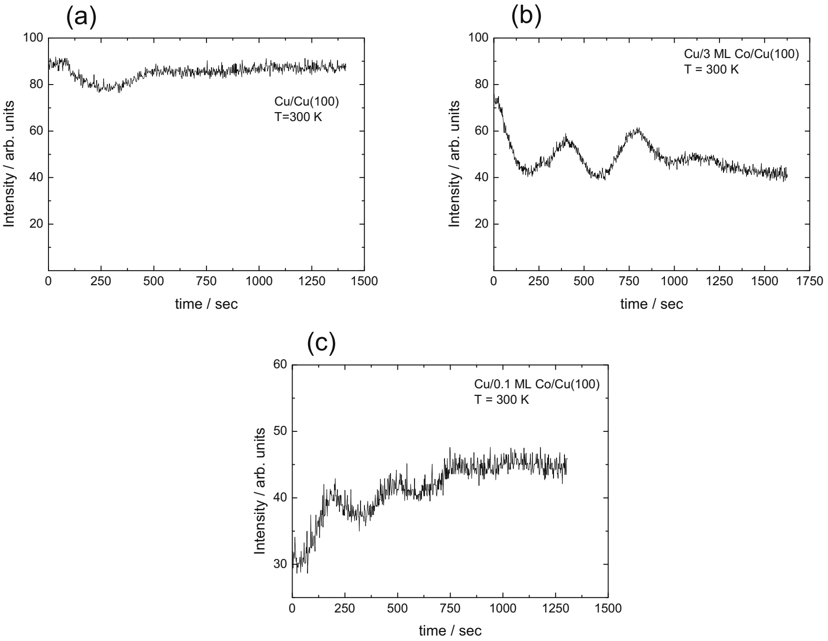

Figure 6.10: MEED intensity oscillations of the specular beam for (a) homoepitaxial growth of Cu on Cu(100) (b) Cu grown on 3 ML Co and (c) Cu grown on 0.1 ML Co.

melting is very narrow. The typical heating power used for the preparation of Cu films presented in this work is about 8W. Furthermore, the evaporation rate played a crucial role in the preparation of Cu films. The typical evaporation rate used was about $0.15 - 0.2$ ML/min. Higher evaporation rates resulted in the formation of melt bubbles on the tip of the Cu rod which hindered further evaporation. The thickness of the Cu layer was calibrated by means of MEED. The oscillations in the intensities of the diffraction beam were not observed for homoepitaxial growth of Cu on Cu(100) at 300 K. The specular intensity as a function of deposition time for Cu/Cu(100) growth is shown in Fig. 6.10(a). The specular intensity stays at a high level without any decay. This indicates that at this temperature, the diffusion is so fast that the deposited adatoms diffuse to the surface steps which act as sinks and the film growth proceeds by the lateral displacement of the steps. It is known that the 2D layer-by-layer growth proceeding via nucleation of islands occurs at temperatures slightly below room temperature (250 K) and oscillations in MEED diffraction intensity can be observed [103]. However, at the time of the measurements presented in this chapter, the manipulator lacked the facility for cooling the sample. In order to observe intensity oscillations, the following procedure was adopted. Three monolayers of cobalt were deposited on the Cu(100) crystal to make the surface rough and provide nucleation centers for the growth of copper. The copper adatoms attach to the nucleation centers provided by the rough cobalt surface resulting in the growth of 2D islands. The islands merge into a flat terrace and the growth process continues resulting in the observation of oscillations (Fig. 6.10(b)). Even 0.1 ML of cobalt is sufficient to provide the nucleation centers required for the observation of oscillations as shown in Fig. 6.10(c). The initial transient in Fig. 6.10(b) goes down whereas in 6.10(c) it goes up. The initial transient is due to the scattering of incident electrons from the isolated adatoms. In the case of (b), the Cu atoms are deposited on a complete 3 ML Co film which has a nearly smooth surface. Hence, the addition of Cu atoms results in a reduction of diffraction intensity. In the case of (c), the reverse process takes place. Copper is deposited on an initially rough surface which eventually becomes smooth when a monolayer is completed. The MEED intensity oscillations obtained from the above procedures were used to calibrate the flux meter of the evaporator. The thickness of the films prepared for spin wave measurements was calculated according to the exposure time. The spin waves were measured on copper films of thickness ranging from $1 - 12$ ML on 8 ML Co/Cu(100).

6.4.2 Spin wave spectra

The 3d-band of copper is fully occupied and hence has no possibilities for low energy excitations. Hence, the mean free path of electrons of sufficiently low energy in copper should be larger than in Ni. Thus, electrons of 6 eV energy in vacuum are expected to look through thicker cover layers. This is indeed the case. The loss features due to excitation of spin waves could be identified for up to 12 layers of Cu on Co. A series of spin wave spectra as a function of $\Delta K_{\parallel}$ measured for deposition of six layers of Cu on a Co film is shown in Fig. 6.11(a). The spectra are measured with a data accumulation time of 2 s. The specific intensity of the spin wave loss for a particular wave vector $\Delta K_{\parallel} = 0.6\text{Å}^{-1}$ as a function of copper coverage is shown in Fig. 6.11(b) (open symbols). The figure also shows the spin wave peak energy as a function of copper coverage for $\Delta K_{\parallel} = 0.6\text{Å}^{-1}$ (solid symbols). Similar to the case of Ni, the energy shifts down upon deposition of Cu and the down shift continues until about three monolayers coverage beyond which it stays constant. The down shift is about 25 meV. The specific intensity shows a steep decrease until about three monolayers coverage. Beyond that, the intensity exhibits an exponential decay which is less steep than for a Ni overlayer. A mean free path fit following the procedure described in Section 6.3.2 in the coverage regime between $3 - 12$ ML with Eq. (6.2) yields a value of $\lambda = 37\text{Å}$. As in the case of Ni overlayers, the good fit of the experimental intensities with the mean free path model indicates that the observed spin waves arise from the Co surface of the Cu/Co(100) interface.

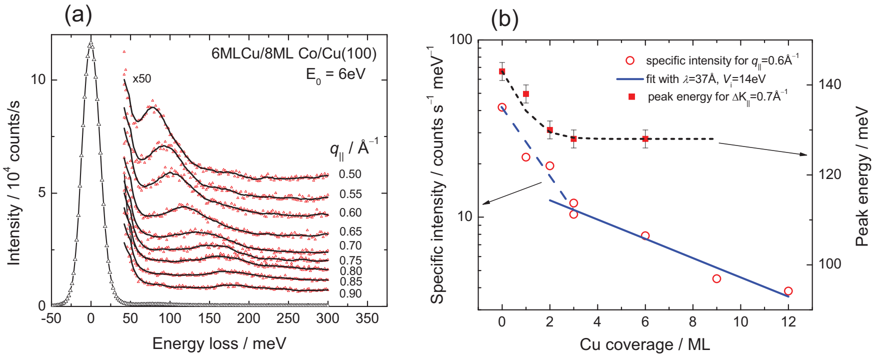

Figure 6.11: (a) Series of spin wave spectra of the 6ML Cu/8ML Co/Cu(100) system as a function of the wave vector $\Delta K_{\|}$. The spectra are offset with respect to each other along the vertical axis. (b) Specific intensity and peak energy of the spin wave energy loss at $\Delta K_{\|} = 0.6\mathring{A}^{-1}$ as a function of Cu thickness in monolayer units. The peak energy drops down until a coverage of about 3 ML Cu beyond which it stays constant. The intensity exhibits rapid linear decay until about three monolayers coverage (dashed line). Beyond that thickness the intensity decays exponentially (solid line). However, the decay is less steep than in nickel (see Fig. 6.6).

6.4.3 Dispersion of Cu/Co interface spin waves

A comparison of the dispersion of the 6 ML Cu/Co interface spin waves with the surface spin wave dispersion of an 8 ML cobalt film measured along the [011]-direction is shown in Fig. 6.12. The solid circles and open diamonds represent the dispersion of an 8 ML Co film and the Cu/Co interface, respectively. It can be seen that the dispersion curve of the interface spin waves is slightly downshifted compared to bare cobalt. However, the downshift is smaller compared to the Ni/Co interface spin waves (see Fig. 6.7). The dotted line represents the surface mode of a semi-infinite fcc(100) film obtained from the Heisenberg model with $JS = 15\,\text{meV}$. Some possible reasons for the reduction of interface spin wave energies are discussed in the next two sections.

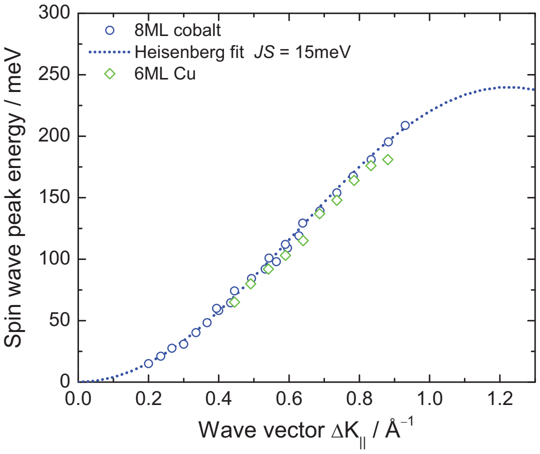

Figure 6.12: Dispersion for the surface spin waves (circles) of 8 ML Co/Cu(100) and the interface spin waves of 6 ML Cu/8 ML Co/Cu(100) (diamonds). The in-plane wave vector transfer is oriented along the [011]-direction. The dotted line is a fit to the Heisenberg model which merely serve to guide the eye.

6.4.4 Width of Cu/Co(100) interface spin waves

Figure 6.13(a) presents the FWHM of the spin wave spectra as a function of energy on a bare cobalt surface (solid symbols) and on a cobalt surface covered with copper overlayers (open symbols). The open triangles and circles represent the data for 3 ML and 6 ML Cu coverage, respectively. Within the error bars, the interface spin waves exhibit similar widths for both Cu overlayer thicknesses. The solid line is a least square linear fit to the Co/Cu(100) data (see also Section 4.4.3). The dashed line is shifted upwards by 25 meV to match the data of interface spin waves. In the case of Co spin waves, the linear relation between linewidth and energy passes zero width at a spin wave energy of ≈ 20 meV indicating a closing of the main decay channels (see also Section 4.4.3). However, one can see that an extrapolation of the linear fit for the Cu/Co interface spin waves would lead to finite width even at zero energy. This suggests that the additional non-magnetic Cu overlayer provides a significant reservoir of spin flip excitations that damp the spin waves even at small energies.

In the following paragraph, we explore the question as to whether the reduction in the spin wave energy can be attributed entirely to the increased damping. For that purpose, let us consider the linear response susceptibility of the form

$$\chi(\omega) \propto \frac{1}{\omega_0^2 - \omega^2 - \mathrm{i}\gamma\omega} \tag{6.10}$$

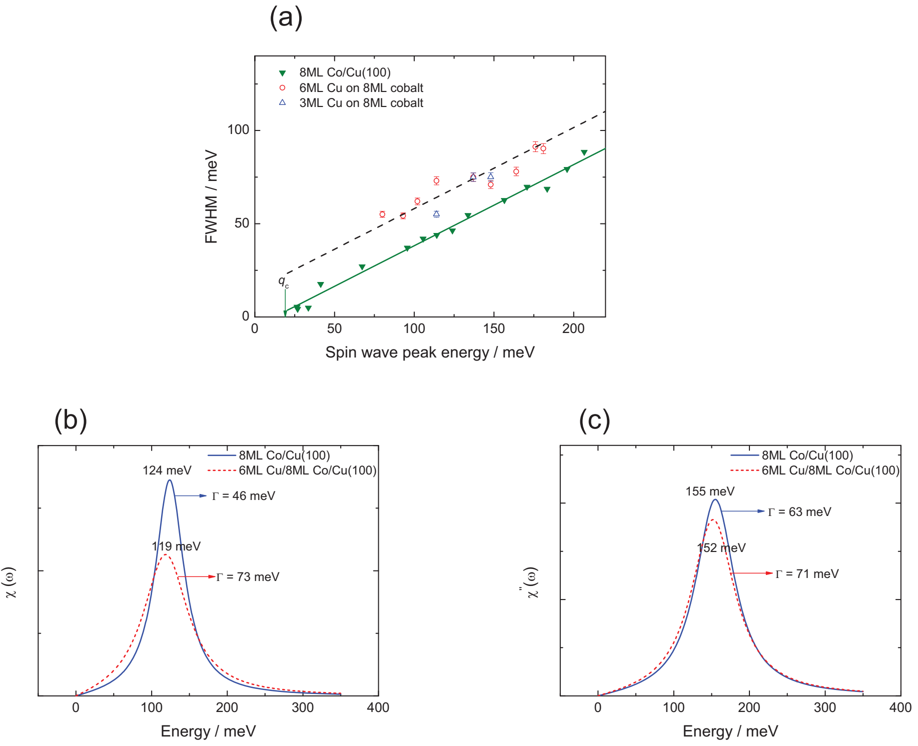

Figure 6.13: (a) FWHM of spin wave energy loss signals as a function of the spin wave peak energy for the 8 ML Co/Cu(100) system (solid symbols) and the Cu/Co/Cu(100) system (open symbols). The solid and dashed lines are linear fits with the same slope to the Co spin waves and the interface spin waves, respectively. The fits are offset on the energy scale by 25 meV. (b) and (c) represent the imaginary part of the susceptibility for two different peak energies and widths, respectively. The solid curves in (b) and (c) are obtained with spin wave energies and FWHM of a bare Co surface at $\Delta K_{\parallel} = 0.64 \text{Å}^{-1}$ and 0.74Å^{-1}, respectively. The dotted curves are obtained by an additional broadening of the widths as indicated in (a). The downward peak shift by about $3 - 5$ meV is not enough to explain the observed energy shift just by the increased Landau damping.

with γ the damping constant. The imaginary part of the response function is peaked at the frequency $\omega = \omega_0$ and has a Lorentzian line shape with FWHM equal to γ. The imaginary part of the response function is

$$\chi''(\omega) \propto \frac{\gamma\omega}{\left(\omega_0^2 - \omega^2\right)^2 + \gamma^2\omega^2} \tag{6.11}$$

This imaginary part of the susceptibility can be matched to the resonance energy and FWHM of the cobalt spin wave data. One can then increase the FWHM by an appropriate amount to match the observed increase of the width of the interface spin waves and study the shift in the resonance energy resulting just from the increase in the FWHM. If the shift in the peak position matches the experimental peak shift upon deposition of the Cu capping layers (Fig. 6.12), this would be an evidence that the observed energy shift with the overlayer addition is just a consequence of the increased damping.

As an example, consider the spin wave energies of bare Co and a Co/Cu interface at $\Delta K_{\parallel} = 0.64\text{Å}^{-1}$ from Fig. 6.12. The peak energies of the Co spin wave and the Cu/Co interface spin wave are 124 meV and 114 meV, respectively. From Fig. 6.13(a), the widths of the spin waves at these energies are 46 meV and 73 meV, respectively. The Lorentzian curve given by χ'' for $\omega_0 = 124$ meV and $\gamma = 46$ meV is shown by solid line in Fig. 6.13(b). Now increasing the width to $\gamma = 73$ meV yields a Lorentzian shape curve (dashed curve) with a peak centered at $\omega_0 = 119$ meV. As mentioned above, the experimental peak energy of the Cu/Co interface spin wave at this wave vector is 114 meV, however. The effect is also shown for another wave vector $\Delta K_{\parallel} = 0.74\text{Å}^{-1}$ in Fig. 6.13(c). The spin wave energies (widths) should be 155 meV (63 meV) and 148 meV (71 meV) for Co and the Cu/Co interface, respectively. The peak of the Lorentzian response function with $\gamma = 71$ meV, however, is at 152 meV (dashed curve), 4 meV higher than the experimental peak energy. This discrepancy indicates that the model is in qualitative accord with the experimental trend i.e., that the spin wave energies shift down with increased damping. However, the experimental shift is higher compared to that calculated from the linear response susceptibility. Hence, there should be additional mechanisms responsible for the energy shift upon capping cobalt layers with copper.

6.4.5 Effect of interface magnetic moment

It has been reported that the Curie temperature and the magnetic moment of the cobalt films are reduced on capping Co with copper [95, 96]. The effect is saturated after the growth of $\approx 2-5$ ML of Cu on top of cobalt. Capping Co films with $2-5$ ML Cu reduced the magnetic moment per Co atom from $2.28\mu_{\mathrm{B}}$ to $\approx 1.4\mu_{\mathrm{B}}$ [95, 96]. The Curie temperature of a 2 ML Co film is found to be reduced by about 100 K on capping with 2 ML copper [95]. The reduced T_{C} and the reduced magnetic moments suggest that the Cu capping induces modifications in the electronic structure of the cobalt films, possibly due to the hybridization effects between the cobalt d states and the sp states of copper [95]. Since the spin wave energy approximately scales with the Curie temperature, the observed reduction is consistent with the aforementioned experimental studies.

6.5 Summary

The spin waves of an 8 ML Co film on Cu(100) with capping of $1-3$ ML Ni and $1-12$ ML Cu are investigated. The intensities of the spin waves as a function of overlayer thickness can be explained by a mean free path model for Ni and Cu. This indicates that the observed spin waves are interface spin waves localized at the Co side of the Ni/Co and Cu/Co interface, respectively. The interface spin waves are softer compared to the bare cobalt spin waves. The downshift is more pronounced for the Ni/Co interface. In the case of the Ni/Co interface spin waves, the FWHM reduces below that for the Co spin waves at higher wave vectors, indicating a reduced damping of the spin waves. The effect could be the outcome of a modified interface electronic structure upon capping with Ni layers. For Cu/Co, the FWHM of the interface spin waves is larger than in the case of Co spin waves for the entire range of wave vectors investigated. The softening of spin wave energies in both systems is attributed to the changes in the electronic structure at the interface.

7 Surface spin waves of ultrathin iron layers

7.1 Introduction

Iron, which is located between antiferromagnetic Mn and ferromagnetic Co in the periodic table is an extensively studied magnetic element. While body-centered cubic (bcc) Fe ($\alpha-$Fe) is the prototypical ferromagnet in its thermodynamically stable phase, the face-centered cubic (fcc) phase of iron ($\gamma-$Fe) is known to exhibit a variety of magnetic phases with varying lattice spacing. Fcc Fe can exist in a non-magnetic or antiferromagnetic phase, in a low-spin or in a high-spin ferromagnetic phase [104–106] or exhibit a spiral-spin-density-wave character [107] depending on the lattice constant. In the bulk, the fcc phase ($\gamma-$Fe) is stable in the paramagnetic state in the high temperature regime (1183K $< T <$ 1663K) [108]. In the hope of stabilizing fcc structures at room temperature with different magnetic phases, researchers have investigated pseudomorphic growth of iron on various substrates. Growth of Fe films on Cu(100) attracted much attention due to the small lattice misfit between Cu ($\mathrm{a}_{\mathrm{Cu}} = 3.615$Å) and fcc Fe ($a_{\text{Fe-fcc}} = 3.58$Å) [109–112]. As a function of film thickness, three different regimes with distinct magnetic properties have been observed [111]. Films thinner than four monolayers (region I) are ferromagnetic and the magnetization is oriented perpendicular to the surface. Films between $5-11$ ML (region II) exhibit a ferromagnetic surface layer with perpendicular magnetization and antiferromagnetic ordering in the interior of the film. Films thicker than 11 ML (region III) are ferromagnetic with magnetization parallel to the surface. The structure of the films in region I and II, which was believed to be fcc with a slight tetragonal distortion for decades, was corrected by the scanning tunneling microscopy (STM) studies of Biedermann *et al.* [113–115]. These authors showed that within the $3-5$ ML system, the local coordination of the surface atoms resembles the (110) surface of the bcc structure. The new structure was termed *nanomartensite.* Films in region II exhibit a mixture of fcc- and bcc- like phases, whereas films in region III exhibit the native bcc structure of iron. Because of such rich variety of structural and magnetic phases for iron films on Cu(100), the system is particularly interesting with respect to the spin wave behavior. I have particularly studied the dispersion of large wave vector spin waves of $3-5\,\mathrm{ML}$ Fe films epitaxially grown on Cu(100) which exhibit ferromagnetic ordering and perpendicular orientation of the magnetization. As a comparison, I have furthermore studied the spin waves of four monolayers of iron deposited on 8 ML Co/Cu(100). There, the iron film exhibits the same structure as in the case of four monolayer Fe/Cu(100), however with in-plane magnetization [116, 117]. This serves as a good reference to study any possible effect of crystalline anisotropy of the sample on spin waves. For all the layers the spin wave dispersion is found to be nearly identical to the dispersion reported for ferromagnetically coupled bcc Fe(110) layers on W(110). This indicates that the observed spin wave signal stems entirely from the bcc-like sections of the surface.

The chapter is divided into four sections. Section 7.2 comprises the results of surface spin waves on $3-5\,\mathrm{ML}$ epitaxial iron films on Cu(100) surfaces. Section 7.3 deals with the results of spin waves on a 4 ML Fe film grown on an 8 ML fcc Co(100) surface stabilized on a Cu(100) substrate. Section 7.4 presents the results of energy loss spectra of iron clusters on an 8 ML Co surface. Section 7.5 provides an analysis of the results and explores the correlation between structure and spin waves. A model is proposed to explain the spin waves in 3 ML and 5 ML Fe films.

7.2 The Fe/Cu(100) system

The section begins with a review of selected results from previous studies that leads to the present understanding of the structural and magnetic properties of Fe films on Cu(100). The review is followed by the description of the preparation and characterization of the films used in our studies. The results of spin wave measurements on $3-5$ ML Fe films on Cu(100) are presented in the last part.

7.2.1 Structure and magnetic properties

Iron films grown on Cu(100) substrates display striking changes in their magnetic properties which are related to the structural changes within the films [111,118]. The information on magnetic properties has been predominantly obtained from surface magneto optic Kerr effect (SMOKE) measurements [111, 112]. Fig. 7.1 summarizes the thickness dependence of the Kerr ellipticity for Fe films deposited on Cu(100). The figure is taken from Ref. [111]. The Kerr signals were obtained by recording the hysteresis loops in longitudinal (open circles) and polar geometry (solid circles) for films grown at room temperature. The Kerr ellipticity in regions I and III increases linearly with coverage indicating that the entire film is ferromagnetic, however with perpendicular and in-plane magnetization, respectively. On the other hand, for coverages between 5 and 11 ML, the polar Kerr ellipticity is relatively small and constant indicating that only a small and constant number of Fe layers contribute to the ferromagnetic signal. The Curie temperatures (T_{C}) of these films are also

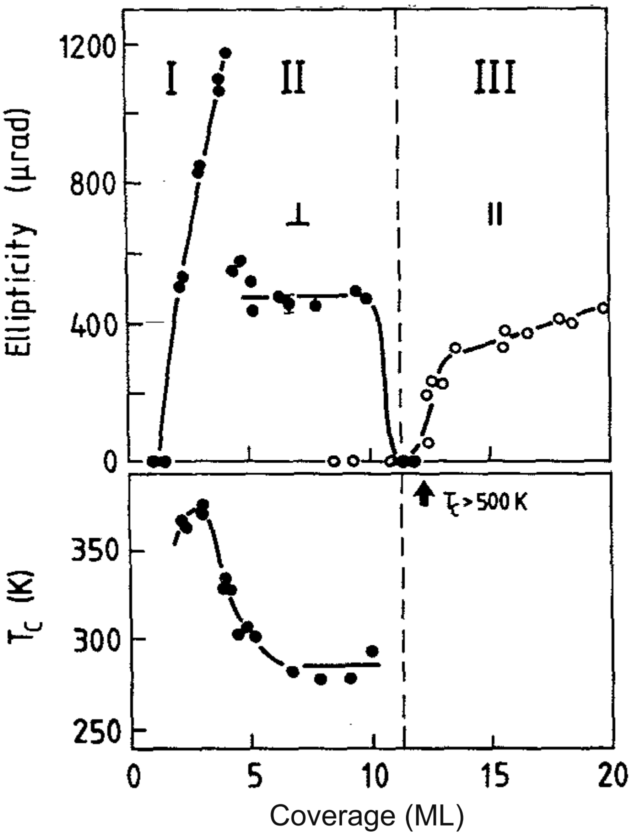

Figure 7.1: Kerr ellipticities as a function of the thickness of the iron film grown on Cu(100). The solid and open circles denote the Kerr signals obtained in polar and longitudinal geometry, respectively. Three regions with different magnetic properties can be distinguished. In region I, which is the region of interest in this thesis, the Kerr signal increases linearly with thickness indicating the ferromagnetic state of the whole volume of the film. The film is perpendicularly magnetized in this region as indicated by the polar Kerr signal. The figure is reproduced from Ref. [111].

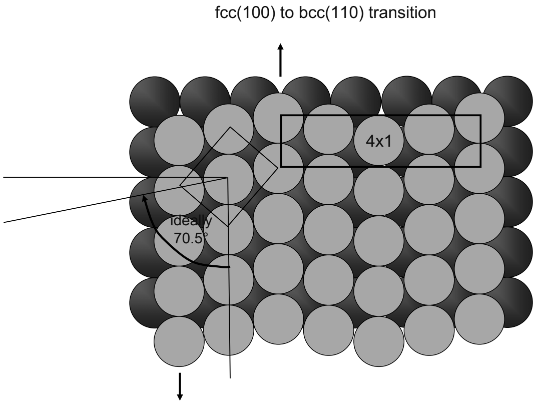

Figure 7.2: Illustration of an fcc(100) to bcc(110) transition resulting in a (4×1) reconstruction. The black spheres represent an fcc(100) lattice and the gray balls represent the bcc(110) film on top of the fcc lattice.

thickness dependent. The T_{C} of films in region I is above room temperature with a maximum of 370 K around 3 ML. In region II, T_{C} drops to values below room temperature whereas in region III T_{C} is above 500 K.

The three regions of different magnetic behavior can be distinguished by their different crystallographic structures identified by low energy electron diffraction (LEED) patterns. Previous LEED studies indicate that several superstructures evolve on the Cu(100) surface with increasing film thickness [113, 119]. A (4×1) reconstruction occurs for films of 2 ML thickness which gradually transforms into a (5×1) phase as the coverage approaches 4 ML [119]. At higher coverages i.e., in region II, the system is known to exhibit a (2×2) superstructure with $p4g$ symmetry [114, 120] or a closely related $p2mg(2 \times 1)$ symmetry [112, 114]. Above 11 ML, a LEED pattern close to the positions expected for a (3×1) structure is seen due to the formation of bcc(110) islands [112]. According to these LEED studies, the films should exhibit a tetragonally distorted fcc structures in regions I and II with expanded atomic volume [112,118]. The position of surface atoms and interlayer distances determined experimentally from LEED studies were in good agreement with theoretical LEED intensities [118, 119] supporting the fcc structure of these films. According to theory, the expanded interatomic distances cause the ferromagnetic coupling between the surface layer and the second layer [104, 106].

However, the LEED results predicting an fcc structures of the films in regions I and II have been disputed later in scanning tunneling microscopy (STM) studies by Biedermann *et al.* [113, 114]. These authors showed that the lateral shifts in the surface layer atoms on the $3-4$ ML films are much larger than assumed previously and that the local coordination of the surface atoms resembles the (110) surface of the bcc structure [113, 121]. The local bcc structure consists of narrow stripes of strained bcc(110) twins to minimize the mismatch to the fcc(100) substrate. The reconstructions can be understood as a Bain transition involving a shear along the $[\bar{1}10]$ and $[1\bar{1}0]$ directions of the (100) surface. The shear angle was found to be 14°, somewhat smaller than the 19.5° shear angle that would lead to a relaxed bcc structure. The new structure was termed *nanomartensite.* A schematic view of this fcc(100) to bcc(110) transition giving rise to a (4×1) reconstruction is shown in Fig. 7.2. The black balls represent an fcc(100) lattice. The grey balls depict the bcc(110) lattice, obtained by shifting the left top row of an fcc structure down and the right top row up. The observed $(n \times 1)$ surface structure can be made up by the combination of such shifts.

The fraction of the film that is in the nanomartensitic phase depends on the layer thickness, the temperature and the hydrogen coverage [115, 121]. The 3 ML system is in the nanomartensitic phase at all temperatures between 80 K and 340 K. The 4 ML film is in the nanomartensitic phase only in the presence of small doses of hydrogen, a dose which is inevitably adsorbed on the surface from the residual gas in all but Extreme High Vacuum (XHV) systems. The fraction of nanomartensitic phase at 4 ML increases strongly on reducing the temperature by as little as 40 K [115]. The 5 ML film exhibits a nanomartensitic phase only after exposing the surface to large doses of hydrogen. The series of papers by Biedermann *et al.*, in particular [115] appears to provide a clear picture of the structure of films in regions I and II. According to this picture, the transition from region I to II corresponds to a transition from a phase dominated by nanomartensite to an fcc phase with a surface reconstruction. The studies could well account for the observed ferromagnetic behavior in films of $3-5$ ML thickness. The biaxial strain which is required to make the bcc film commensurate to the fcc(100) substrate results in interlayer expansion which is correlated to the ferromagnetic ordering. Biedermann's conclusions are furthermore consistent with an ion channeling study of Bernhard *et al.* [109].

7.2.2 Preparation

Prior to the preparation of iron films, the iron rod was cleaned in the following procedure to get rid of any carbon contamination from the rod: The preparation chamber is filled with hydrogen by opening a leak valve to a pressure of about 1×10^{-6} mbar. The molecular hydrogen is thermally dissociated at the hot filament. The atomic hydrogen reacts with the carbon contamination on the surface of the Fe rod and other parts of the evaporator resulting in the formation of hydrocarbons. The hydrocarbons, once they are saturated do not bind to the surface of the Fe rod and are effectively pumped off. This "hydrogen purging" treatment was performed until carbon was below the detection limit in the Auger spectrum of Fe deposition on Cu(100). After this treatment, the energy loss spectra indicated no signature of hydrocarbons.

The Cu(100) single crystal was sputter cleaned and annealed as described in Section 4.2.1 until a sharp $p(1 \times 1)$ LEED pattern was observed. After the annealing

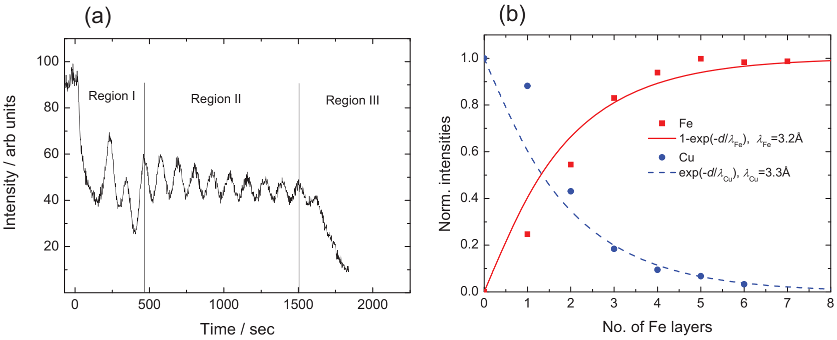

Figure 7.3: (a) A typical MEED intensity oscillation for Fe layers grown on Cu(100) at room temperature. The three regions labelled are correlated with different regimes of growth. (b) Intensities of the 66 eV Cu and the 50 eV Fe Auger lines versus Fe coverage. Intensities are normalized to their initial and final value, respectively. The solid and dashed lines are fits to a mean free path model. See text for details.

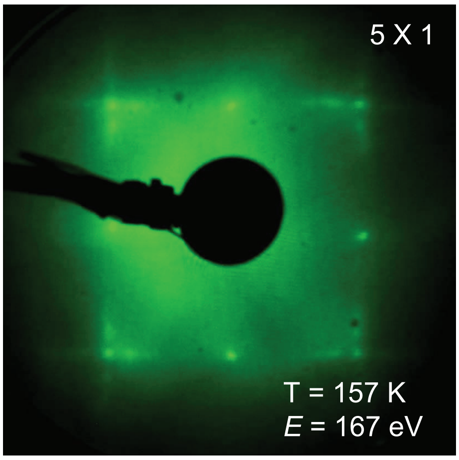

Figure 7.4: A (5×1) LEED pattern observed for 4 ML Fe films grown on Cu(100).

stage of the preparation, the Cu substrate was completely cooled down to room temperature to avoid any thermal activation of diffusion processes during deposition of iron. Iron films were evaporated from a rod (which was cleaned by “hydrogen purging” treatment) of 99.995% purity by electron-beam evaporation onto a Cu(100) substrate held at room temperature. The typical evaporation rate was 0.5 ML/min as determined by MEED intensity oscillations. A typical MEED measurement taken during the growth of Fe on Cu(100) is shown in Fig. 7.3(a). The diffraction intensity oscillations exhibit a complex pattern during the initial stages of growth with the absence of the first oscillation peak that should correspond to the completion of one atomic layer. This is due to the intermixing of Fe and Cu which is, however, limited to the first two monolayers [122] as evident from our intensity study of the low energy Auger peak (Fig. 7.3(b)). Fig. 7.3(b) indicates the intensities of the Cu (66 eV) and Fe (50 eV) peaks as a function of Fe coverage. The intensities are normalized to their initial and final value, respectively. The observed intensities are fit by a mean free path model assuming that the electron beam penetrates the sample with exponentially decaying intensity. The fit equations for Fe and Cu are given by $I_{\mathrm{Fe,norm.}}(d) = 1-\exp(-d/\lambda_{\mathrm{Fe}})$ and $I_{\mathrm{Cu,norm.}}(d) = \exp(-d/\lambda_{\mathrm{Cu}})$, respectively with d the path length as a function of coverage and λ_{Fe} and λ_{Cu}, the mean free path of electrons in Fe and Cu, respectively. A good fit is observed beyond 2 ML Fe coverage and the mean free path of electrons in Fe and Cu is obtained as 3.2 Å and 3.3 Å, respectively. For coverage ≤ 2 ML the intensity of the peaks deviates from the fitted curve with the Cu intensity being higher and the Fe intensity lower than the expected value. This indicates intermixing and possible flipping of Cu and Fe layers in the initial growth stages. Beyond 2 ML coverage there is no visible intermixing. A LEED pattern observed on 4 ML Fe/Cu(100) is depicted in Fig. 7.4. The pattern shows a sharp (5×1) structure as expected for this system [112, 118].

7.2.3 Spin waves of the 4 ML Fe/Cu(100) system

In this section, the results of the spin wave measurements of four monolayer Fe films on Cu(100) surfaces are presented. The spin waves were probed along the [011] and the [010] directions which correspond to the $\overline{\Gamma}\,\overline{\mathrm{X}}$ and $\overline{\Gamma}\,\overline{\mathrm{M}}$ directions, respectively in the substrate reciprocal space (see Fig. 4.3). The scattering angle for all measurements was kept constant at 90°. The incident electron energy is $E_0 = 6$ eV.

Figure 7.5 depicts a series of spectra measured for $\Delta \mathrm{K}_{\parallel} = 0.85\mathrm{\AA}^{-1}$ along the [011]-direction as a function of temperature. It can be seen that at room temperature only a tail in the elastic peak exists without any peak structure. However, the tail develops into a peak corresponding to spin wave excitation as the temperature is lowered. A clear peak is visible at about 100 K with the structure becoming more pronounced as the temperature reaches 90 K. The time between the recording of the spectra at 300 K and 90 K was 20 minutes. The pressure was better than

Figure 7.5: Series of energy loss spectra measured on four monolayers of Fe/Cu(100) as a function of temperature. The wave vector transfer of 0.85Å^{-1} is oriented along the [011]-direction. The incident electron energy is 6 eV. A tail in the elastic peak at room temperature develops into a peak structure as the temperature is lowered. The peak structure is pronounced at 90 K.

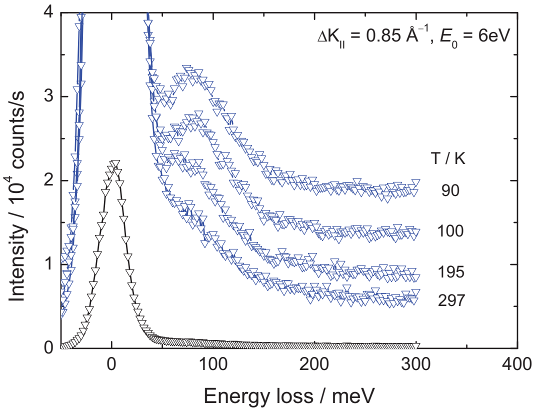

2×10^{-11} mbar. 90 K is the minimum temperature that can be achieved with our experimental setup. Hence all the spin wave measurements presented in this section were performed at 90 K.

Figure 7.6 presents a sample spin wave spectrum measured for wave vector transfer $\Delta K_{\parallel} = 0.8\text{Å}^{-1}$ along the [011]- direction. The complete spin wave spectrum is represented by the black curve (circles) while the blue curve represents (squares) the magnified spectrum (by a factor of 10) to clearly see the spin wave. The energy of the spin wave peak is determined by applying a fitting procedure. The procedure begins with fitting a background which consists of the Gaussian tail of the elastic peak and a constant. This is indicated by the black dashed line in the figure. The spin wave peak represented by the red curve (triangles) is obtained after subtraction of the background from the original spectrum. The spectrum is asymmetric as in the case of cobalt layers on Cu(100), possibly because of the contribution of overdamped standing waves (see for e.g., Fig. 4.5). To determine the peak position from this background subtracted spectrum, a parabola fit is applied to a limited set of data points around the peak. This is depicted in the inset of Fig. 7.6 from which the peak energy is determined to be 76.7 meV. The FWHM of the quasi elastic peak is about 31 meV. The FWHM of the spin wave peak directly measured from the spectrum is about 80 meV. The FWHM of the spin wave signal measured on Co/Cu(100) for a spin wave energy of 74 meV is about 28 meV (see Fig. 4.16). Thus, the width of the spin wave peaks in the Fe/Cu(100) system is more than a factor of 2 larger than that measured on the Co/Cu(100) system. This broad nature of the spin waves in this system restricts the observation of spin waves to wave vectors larger than 0.6Å^{-1}.

A series of spin wave spectra measured for wave vectors ranging from $\Delta K_{\parallel} = 0.6\text{Å}^{-1} - 1.0\text{Å}^{-1}$ is presented in Fig. 7.7. The experiments were repeated several

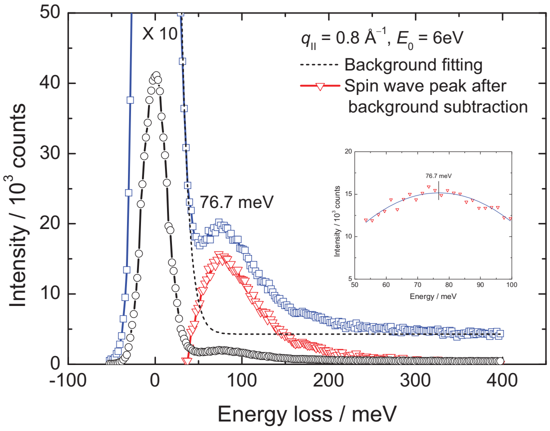

Figure 7.6: Spin wave spectrum measured for 4 ML Fe/Cu(100) for an in-plane wave vector transfer of $\Delta K_{\parallel} = 0.8\text{Å}^{-1}$ along the [011]-direction. The incident electron energy is 6 eV. The blue curve (squares) represents the measured spin wave spectrum magnified by a factor of 10. The red curve (triangles) represents the spin wave peak after subtraction of background. The background consists of a Gaussian for the tail of the elastic peak and a constant count rate (black dashed line). The spin wave peak energy is determined by fitting a parabola to a limited set of data around the peak position (see inset).

times with a fresh sample prepared each time to account for the reproducibility of the data. The samples were prepared in an identical procedure for all the experiments. The results of three such experiments are shown in Fig. 7.7 (a), (b) and (c). The tiny shoulder at around 120 meV visible in all the measurements is a vibrational excitation peak due to the adsorption of hydrogen atoms on the surface [123]. The amount of hydrogen adsorbed on the surface is different for the three sets of measurements depending on the residual gas pressure in the preparation chamber and the spectrometer chamber. The series of spectra represented in Fig. 7.7(c) has the highest contamination of hydrogen. The series of spectra in (a) has an additional peak at about 90 meV corresponding to the vibrational excitation of an OH-bending mode on the surface [124]. The energy loss spectra depicted in Fig. 7.7(b), which exhibit the smallest amount of adsorbate is considered to be our best data.

To study the effect of hydrogen (and OH) contamination on the energy of spin waves, the spin wave spectra measured on the three different samples are plotted for a particular wave vector of $\Delta K_{\parallel} = 1.0\text{Å}^{-1}$. This is depicted in Fig. 7.8(a). The spectra marked (a), (b) and (c) are taken from the series (a), (b) and (c) shown in Fig. 7.7, respectively. It can be seen that (a) has the lowest spin wave energy of 93.6 meV. From Fig. 7.7(a) it is known that this sample had OH contamination with the OH bending mode at $\approx$90 meV. Spectrum (b) has the peak energy of 102.6 meV which corresponds to spin waves from a nearly clean sample as shown in Fig. 7.7(b). Spectrum (c) which had the highest hydrogen adsorption with a loss feature at about 120 meV indicates the highest spin wave energy of 106.8 meV. Thus

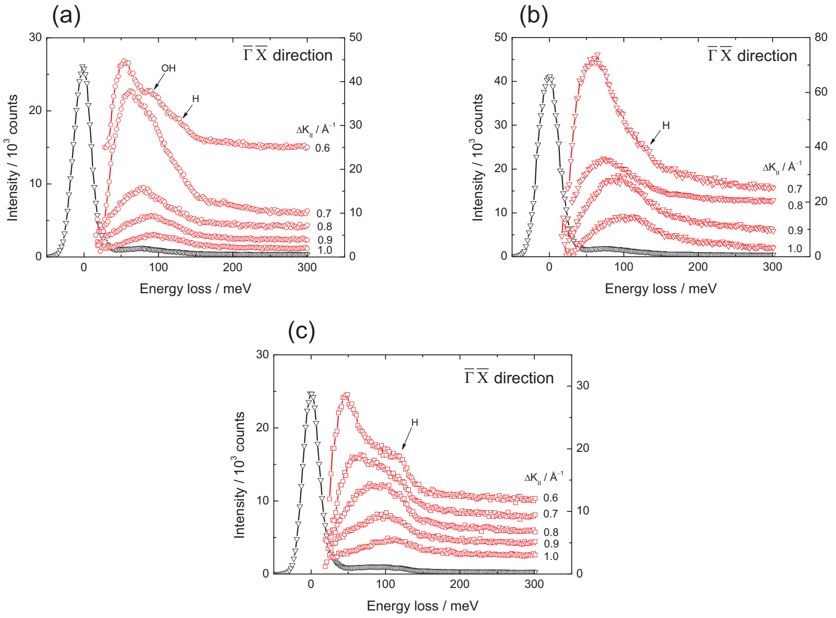

Figure 7.7: Series of spin wave spectra for 4 ML iron films measured with in-plane wave vector transfer along the [011]-direction. The wave vector transfer $\Delta K_\parallel$ is from $0.6Å^{-1} - 1.0Å^{-1}$. (a), (b), (c) represent the spectra measured on three different samples prepared identically. In (a) and (c) one could observe vibrational losses due to the presence of small amounts of adsorbates on the surface. (b) appears nearly contamination free and hence is considered to be our best data.

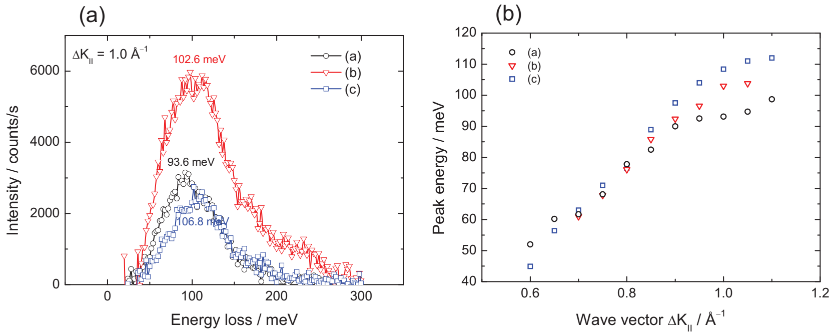

Figure 7.8: (a) Spin wave spectra of three different identically prepared 4 ML Fe/Cu(100) films. All spectra are for $\Delta K_{\|} = 1.0\text{Å}^{-1}$. (a), (b) and (c) represent the spectra taken from the series (a), (b) and (c) shown in Fig. 7.7, respectively. The presence of adsorbates shifts the spin wave energies slightly. (b) Dispersion of spin waves for the three different samples shown in (a).

it is apparent that the presence of an even very small quantity of adsorbates slightly shifts the peak position of the broad spin wave signal.

The spin wave dispersion can be constructed by plotting the peak positions of energy for each wave vector $\Delta K_{\|}$ as a function of the wave vector. However, because of the large width of the spin wave signal and the influence of minute amount of impurities on the apparent peak position, the dispersion curve has to be taken with a grain of salt. The peak positions for the series of spectra shown in Fig 7.7 were determined by applying the fitting procedure described earlier. The dispersion of surface spin waves for all the three samples (a), (b) and (c) as noted in Fig. 7.7 are shown in Fig. 7.8(b). As noted in the last paragraph, the dispersion curve for the sample with the OH (or clear H) excitation peak is lower (or higher) than the nearly clean sample.

The spin wave measurements were also performed on the 4 ML Fe/Cu(100) system for wave vector transfers along the [010]-direction. A selection of spin wave spectra taken for positive wave vector transfers along the [010]-direction is shown in Fig. 7.9(a). The spectra were measured under conditions identical to those used for measurements along [011]-direction i.e. the incident electron energy is $E_0 = 6\,\text{eV}$ and the scattering angle is 90°. Figure 7.9(b) provides a comparison of the dispersion of spin waves measured along both the [011] and [010]-directions. Within limits of accuracy, the dispersion is isotropic in this system as in the case of spin waves of 8 ML fcc Co on Cu(100)(see Fig. 4.10).

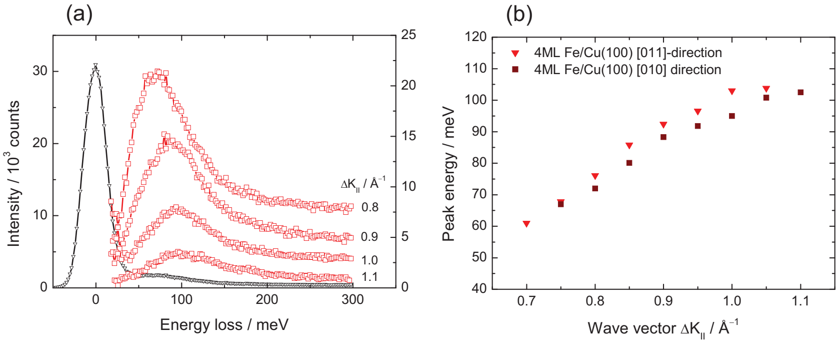

Figure 7.9: (a) Selection of spin wave spectra for 4 ML Fe/Cu(100) measured with $\Delta K_{||}$ along the [010]-direction. (b) comparison of the dispersion of spin waves measured with $\Delta K_{||}$ along the [011] and the [010]-direction.

7.2.4 Spin waves of the 3 ML Fe and 5 ML Fe on Cu(100)

As an extension to the work of spin wave measurements on 4 ML Fe/Cu(100), the experiments were performed on Fe films of varying thickness. A series of spin wave spectra measured on 3 ML and 5 ML Fe is presented in Fig. 7.10(a) and (b), respectively. It is known that Fe films of $1-2$ ML thickness exhibit intermixing between Fe and Cu (see Fig. 7.3). The exact amount of intermixing is variable for each film preparation. To look for the possible effect of this intermixing and hence the morphology of films on the spin waves, the measurements on 3 ML Fe were repeated a few times with freshly prepared samples. The spin wave spectra for a particular wave vector transfer, $\Delta K_{||} = 0.8\text{Å}^{-1}$ along the [011] direction for 3 ML, 4 ML and 5 ML films are summarized in Fig. 7.11(a). The Figure includes spectra of two individual experiments conducted on a 3 ML film. The 4 ML films exhibit the highest intensity. In the case of 3 ML films, the intensity depends sensitively on the particular preparation condition and will be discussed later. The 5 ML film exhibits lower intensity compared to the 4 ML Fe, however, the experiments were not repeated to ensure reproducibility. A comparison of the dispersion of 3, 4, and 5 ML films is shown in Fig. 7.11(b). The 3 ML and 4 ML films exhibit nearly identical dispersion. The dispersion of the 5 ML film appears to be slightly lowered compared to the 3 ML and 4 ML films. However, taking into account, the large width of spin waves combined with the low intensity of spin wave signals for the 5 ML film, the small shift in dispersion may not be significant.

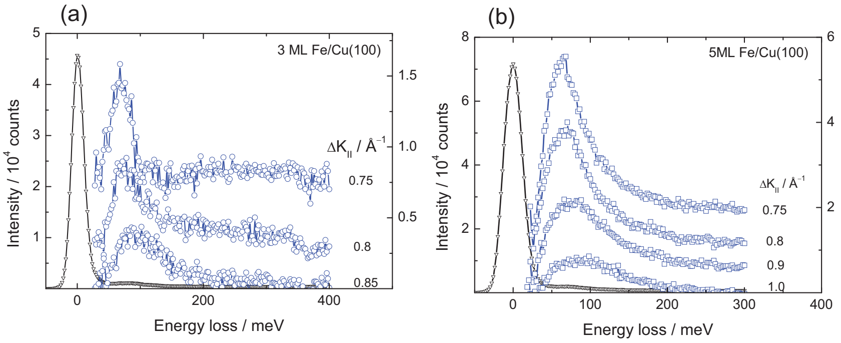

Figure 7.10: Series of spin wave spectra measured for (a) 3 ML and (b) 5 ML Fe films deposited on Cu(100). The spin waves were measured along the [011]-direction. The incident electron energy is 6 eV and $T = 90\,\text{K}$.

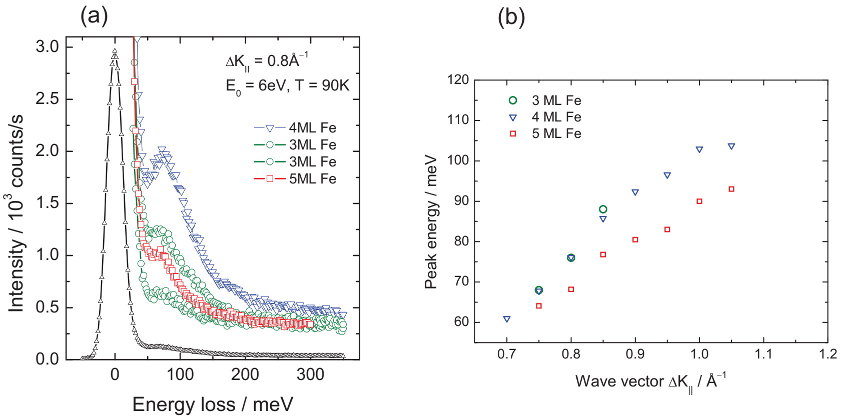

Figure 7.11: (a) Comparison of spectra for a 4 ML film to the spectra obtained for two nominally equal 3 ML films and a 5 ML film. All spectra are for $\Delta K_{\|} = 0.8\text{Å}^{-1}$ measured along the [011]-direction. (b) Comparison of spin wave dispersion of 3 ML, 4 ML and 5 ML Fe/Cu(100).

Figure 7.12: Magnetic dichroism intensity of iron as a function of film thickness for Fe films grown on 10 ML fcc Co(100). The Figure is taken from Ref. [116]. Three regions of different magnetic behavior are distinguished corresponding to the different crystallographic structures identified by LEED. The dichroism signals are observed at room temperature for in-plane magnetization of the sample. A non-zero dichroism intensity in region II indicates in-plane magnetization with the Curie temperature above room temperature as opposed to the Fe/Cu(100) system. See text for details.

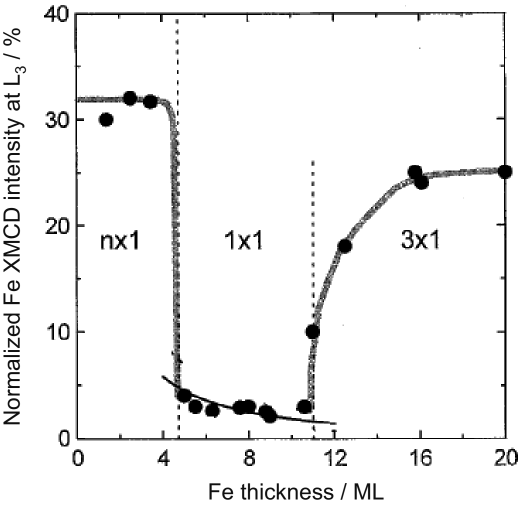

7.3 The Fe/Co(100) system

7.3.1 Structure and magnetic properties

Face centered cubic cobalt can be stabilized on Cu(100) for at least 15 ML due to the very small lattice mismatch between fcc Co (3.56Å) and Cu (3.61Å) [59, 125] (See also Chapter 4). Co grows in a nearly layer-by-layer fashion on Cu(100). Hence there is a strong likelihood that Fe films evaporated onto fcc Co(100) would assume a structure very similar to that on Cu(100). This is actually the case as evident from the previous LEED and MEED experiments on this system [116, 117, 126]. The LEED pattern of Fe deposited at room temperature on Co(100) exhibit a sequence of surface reconstructions identical to the Fe/Cu(100) case. MEED oscillations for the room temperature growth of Fe on Co(100) show three distinct regions similar to that of Fe/Cu(100) deposition [117] giving further indication of the similar structure in both cases.

Similar to the Fe/Cu(100) system, the X-ray dichroism magnetometry measurements revealed three magnetic phases for the Fe/Co(100) system: Region I with a ferromagnetic phase, region II with a ferromagnetic live monolayer and region III with a ferromagnetic phase [116]. This is depicted in Fig. 7.12 taken from Ref. [116]. However, there are two significant differences: in the case of Fe layers on Co(100) the easy axis of magnetization lies in the film plane in all the three regions. This

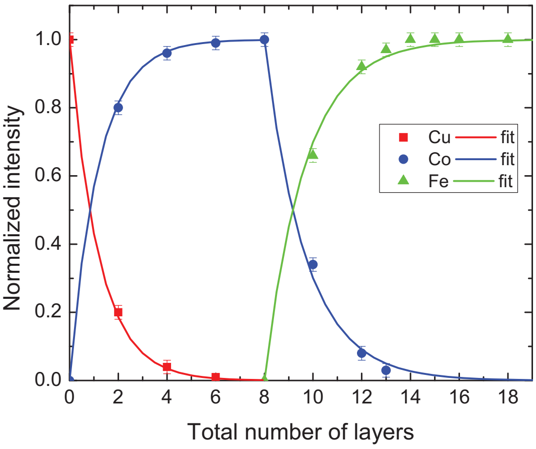

Figure 7.13: Normalized intensities of the Cu (66eV), Co (57eV) and Fe (50eV) Auger lines as function of cobalt and iron coverage. The observed intensities are well fit by the mean free path model indicating no prominent intermixing of the Cu, Co and Fe layers.

is in contrast to the Fe/Cu(100) system, where the magnetization is perpendicular to the film plane in regions I and II and in-plane in region III. Another important difference is that the magnetic live layer in region II in the case of the Fe/Co system exists at the interface of Fe and Co and not on the surface as in the Fe/Cu(100) system [116, 117]. According to the authors of Ref. [116], this is evident from the non-zero dichroism intensity at room temperature in region II (Fig. 7.12). The non-zero dichroism intensity is explained as being due to the ferromagnetic ordering of Fe at the Fe/Co interface induced by the ferromagnetic Co layer. In the case of the Fe/Cu(100) system, the dichroism intensity at room temperature in region II was found to be zero due to the lower Curie temperature in this region i.e. T_C below room temperature. The presence of additional magnetic interaction between the ferromagnetic Co and Fe overlayer was predicted to change the magnetic direction as well as the Curie temperature of the Fe overlayer to well above the room temperature [116, 117].

7.3.2 Preparation

The Cu(100) single crystal was prepared (sputter cleaned and annealed) as described in Section 4.2.1 until a sharp $p(1 \times 1)$ LEED pattern was observed. Cobalt and iron films were evaporated from rods of 99.995 % purity by electron-beam evaporation. The residual gas pressure during evaporation was better than 5×10^{-10} mbar. The typical evaporation rate was 1.25 ML/min and 0.5 ML/min for Co and Fe, respectively as determined from MEED intensity oscillations. The cobalt surface was first formed by epitaxially growing 8 ML Co onto Cu(100) at room temperature followed by the deposition of Fe overlayers on cobalt. The intensities of the low

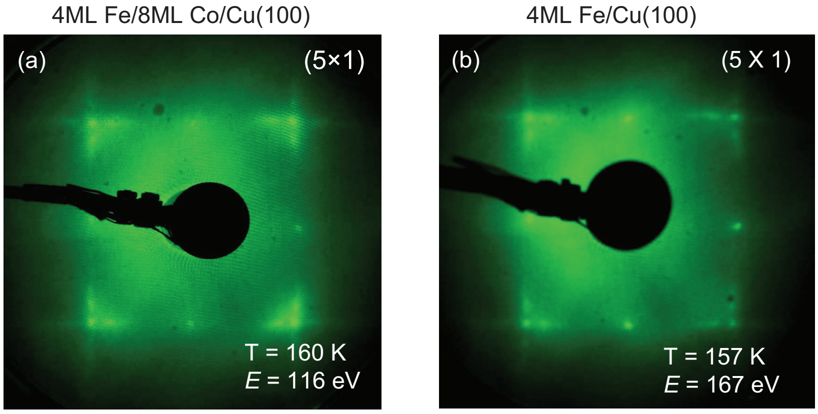

Figure 7.14: (a) LEED pattern of 4 ML Fe on 8 ML Co/Cu(100). (b) LEED pattern of 4 ML Fe/Cu(100). Both systems exhibit a (5×1) reconstruction.

energy Auger peaks (Cu: 66eV, Co: 57eV, Fe: 50eV) are well fit by the mean free path model indicating no visible intermixing at the Cu:Co and Co:Fe interfaces (see Fig. 7.13). A typical LEED pattern observed on 4 ML Fe/8 ML Co/Cu(100) is shown in Fig. 7.14(a). As a comparison, the LEED pattern observed on 4 ML Fe/Cu(100) is shown in Fig. 7.14(b). Both systems exhibit a (5×1) reconstruction indicating their similar structures.

7.3.3 Spin waves of the 4 ML Fe/8 ML Co/Cu(100) system

A selection of spin wave spectra measured on 4 ML Fe/8 ML Co/Cu(100) for wave vector transfers along the [011]-direction is shown in Fig. 7.15(a). The measurements were performed at T = 90 K with an incident electron beam of energy $E_0 = 6$ eV. A comparison of the dispersion of 4 ML Fe/Co(100) and 4 ML Fe/Cu(100) is shown in Fig. 7.15(b). The dispersion is nearly identical in the range of wave vectors investigated.

7.4 Iron clusters on 8 ML Co/Cu(100)

The growth mode, structure and magnetism of iron films depend sensitively on the growth conditions, such as substrate temperature, contamination etc. [127–129]. Depending on the preparation conditions and contamination, the films are known to exhibit many different superstructures in LEED [128,130] and consequent changes in

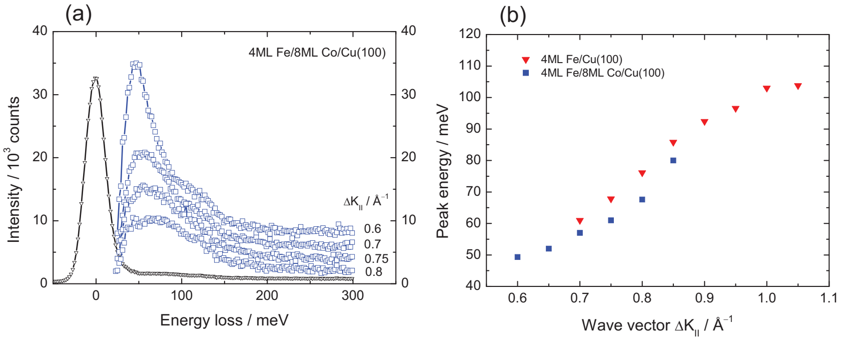

Figure 7.15: (a) Selection of spin wave spectra measured on 4 ML Fe/8 ML Co/Cu(100) for $\Delta K_{||}$ along the [011]-direction. The spectra are for $E_0 = 6\,\text{eV}$ and $T = 90\,\text{K}$. (b) Comparison of the dispersion of spin waves of the 4 ML Fe/Co(100) and 4 ML Fe/Cu(100) systems. The dispersion is nearly identical in the range of wave vectors investigated.

the magnetic properties. For films prepared at low temperature (around 100 K) and annealed to room temperature, the magnetization reorientation from perpendicular to in-plane is known to occur at about 5 − 6 ML [1] and the system exhibits bcc structure [118, 131]. The presence of a small amount of CO shifts the transition point between region II and III from 11 ML to 13 ML [111]. The deposition of iron at slightly different growth conditions than that presented until now and the results of subsequent energy loss spectra are discussed in this section.

7.4.1 Preparation

The cobalt and iron films were evaporated onto a cleaned Cu(100) substrate held at room temperature as described in Section 7.3.2. After preparation the films were briefly annealed to about 475 K for a few minutes. The LEED pattern of nominal 4 ML Fe film on 8 ML Co/Cu(100) deposited at room temperature and the film annealed to higher temperatures after room temperature deposition is shown in Fig. 7.16 (a) and (b), respectively. It can be see that the film after annealing exhibits a $p4g(2 \times 2)$ reconstruction which is different from the (5×1) pattern expected for this system as shown in (a).

---

[1] Note that this reorientation transition occurs around 11 ML for room temperature prepared films.

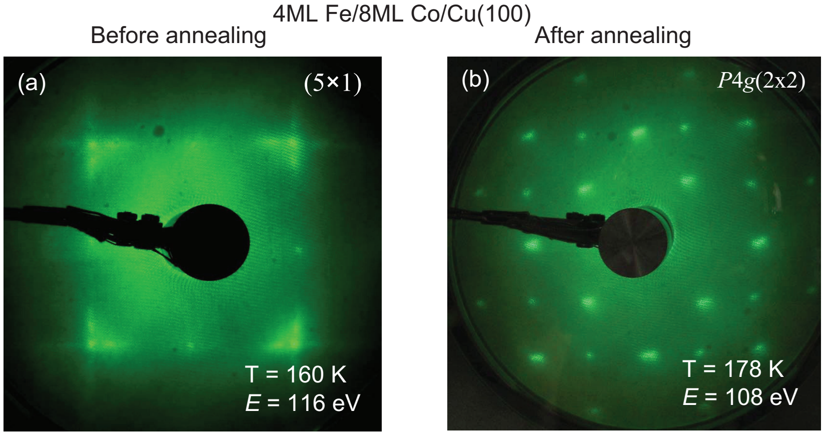

Figure 7.16: LEED pattern of 4 ML Fe/8 ML Co/Cu(100) recorded (a) before annealing and (b) after annealing of the room temperature deposited film briefly to 475 K. The film after annealing exhibits a $p4g(2 \times 2)$ reconstruction which is different from the (5×1) pattern expected for this system (a).

7.4.2 Energy loss spectra

Fig. 7.17 presents an example of the energy loss spectrum of the 8 ML Co/Cu(100) system after deposition of a nominal quantity of 4 ML iron. The wave vector of $\Delta K_{\parallel} = 0.8 \text{Å}^{-1}$ is along the [011]-direction. The measurement was performed at room temperature with an incident electron beam energy of $E_0 = 6$ eV. A pronounced spin wave peak is observed at the energy loss of 161 meV. The excitation peak at about 85 meV can be attributed to the vibrational signature of a small amount of contamination on the surface.

Fig. 7.18(a) presents a series of spin wave spectra measured on a nominal four layers of Fe (blue squares) and ten layers of iron (green circles) deposited on an 8 ML cobalt substrate. The results are shown for wave vectors ranging from $\Delta K_{\parallel} = 0.6 \text{Å}^{-1} - 0.8 \text{Å}^{-1}$. The spin waves measured on an 8 ML Co/Cu(100) film are also shown (red triangles) for comparison. It can be seen that the spin waves of four layers of Fe on Co and ten layers of Fe on Co are close in energy, intensity and width to the bare Co layers on Cu(100). The spin wave dispersion is presented in Fig. 7.18(b) for all three systems. The spin wave dispersion of a Co surface covered with Fe overlayers exhibits a small downward shift compared to the spin wave dispersion of bare cobalt layers. However, the spin wave dispersion with Fe overlayers indicates

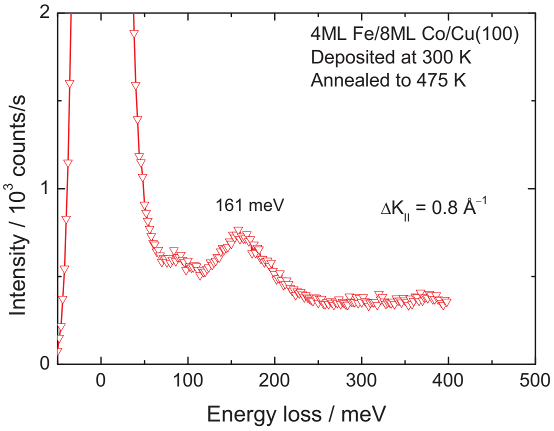

Figure 7.17: Spin wave spectrum of 4 ML Fe deposited on 8 ML Co/Cu(100) at room temperature. The film was briefly annealed to 475 K after deposition. The incident electron energy is 6 eV and the wave vector transfer of $\Delta K_{\parallel} = 0.8$Å^{-1} is oriented along the [011] direction. The spectrum was measured at room temperature.

no thickness dependence, and the dispersion of nominal four ML and ten ML Fe is nearly the same. This is in contrast to the case of Ni and Cu layers on Co where the intensity decayed exponentially with overlayer thickness (see Chapter 6) indicating that the spin waves are localized at the Ni/Co and Cu/Co interfaces. In the present case of Fe/Co, if the observed spin waves excitations were localized at the interface, then the spin wave intensity should exhibit similar exponential decay behavior since the mean free path of electrons in Fe is about the same as that of Ni (about 5Å) [47]. However, as indicated by Fig. 7.18, the spin waves are clearly resolved up to ten ML coverage of Fe on Co without a significant decay in intensity. This suggests that the observed spin waves are not interface modes but true surface spin waves which are slightly modified compared to Co spin waves.

To explore whether the observed spin waves correspond to true surface spin waves of iron, one has to consider the following arguments:
It is known that Fe films in region I exhibit ferromagnetic ordering with the highest magnetization (see Fig. 7.12) whereas the films in region II are characterized by a ferromagnetic live layer and exhibit small and constant magnetization. Assuming that the spin wave intensity scales as the square of the magnetic moment per atom, it is surprising that the spin waves of four layers and ten layers of Fe exhibit similar intensities if the observed spin waves represent true surface spin waves of iron.
Another aspect to note is that, as mentioned earlier, the magnetic live layer in the case of the Fe/Co system is localized at the Fe/Co interface [117]. This indicates that the surface layers of our ten ML Fe is non ferromagnetic which cannot support high energy and high intensity spin waves. Hence, the observed spin waves cannot be true surface spin waves of a high-spin phase of iron.
It is clear that the observed spin waves are neither surface spin waves of Fe nor

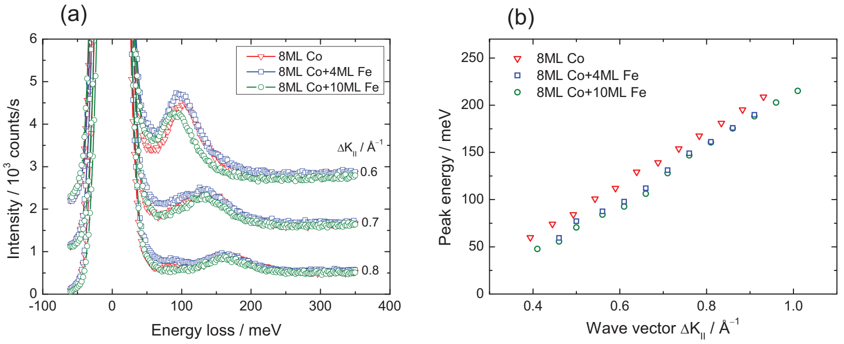

Figure 7.18: (a) Comparison of the spin wave spectra measured on a bare 8 ML cobalt surface (triangles) and after additional deposition of 4 ML Fe (squares) and 10 ML Fe (circles) films. The wave vector transfers range from $0.6\text{Å}^{-1} - 0.8\text{Å}^{-1}$ and are oriented along the [011]-direction. The incident electron energy is 6 eV. The spectra are measured at room temperature. (b) Peak positions of the spin waves of all three systems shown in (a) as a function of wave vector. It can be seen that the spin waves of the three systems are close in energy and intensity.

interface spin waves at the Fe/Co interface. What is the origin of these slightly modified Co spin waves with Fe overlayers on cobalt?

To answer the question, one needs to revisit the preparation procedure and also look carefully at the electron energy loss spectrum. Fig. 7.19(a) presents the spin wave spectra for $\Delta K_{||} = 0.8\text{Å}^{-1}$ measured on the two Fe/Co systems (nominal 4 ML and 10 ML Fe) taken from Fig. 7.18. It can be seen that both spectra exhibit a vibrational peak around 85 meV indicating a possible hydrocarbon contamination on the surface. The spin wave measurements were performed in a vacuum better than 1×10^{-11} mbar and the energy loss spectra did not show an increase in the contamination level with time. An Auger spectrum recorded immediately after the spin wave measurements indicated the presence of carbon on the surface as can be seen from Fig. 7.19(b). This suggests that the contaminants were adsorbed on the surface during preparation. The presence of this contamination could introduce changes in the growth mode and structure of the films. The observed LEED pattern (Fig. 7.16) is consistent with this hypothesis since $p4g(2 \times 2)$ and $c(2 \times 2)$ are common patterns for contaminated surfaces [37]. It is known that even on a clean surface, Fe does not grow in a layer-by-layer mode in the low coverage regime (as indicated by MEED oscillations, for e.g., see Fig. 7.3(a)). STM measurements predict the formation of Fe agglomerates during the initial growth [132]. The presence of contaminants could act as nucleation centres, aiding this agglomeration process further due to the high

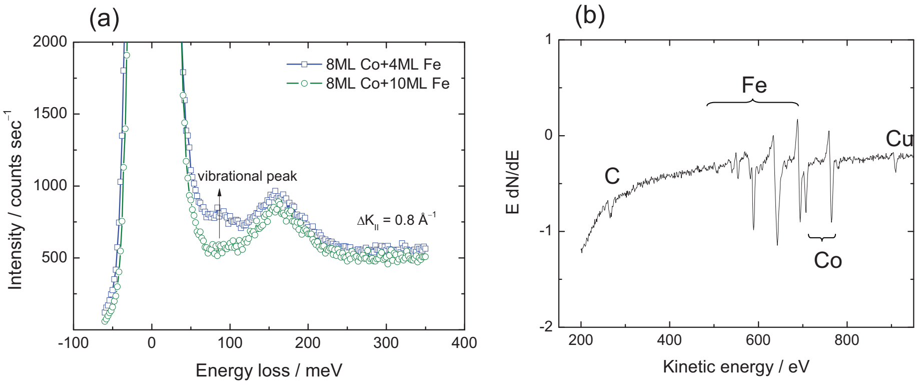

Figure 7.19: (a) Spin wave spectra measured for 4 ML and 10 ML Fe films on 8 ML Co(100) for a particular wave vector transfer of 0.8Å^{-1}. The vibrational peak around 85 meV due to contamination on the surface is visible in both spectra in addition to the spin wave peak. (b) Auger spectrum recorded after the energy loss measurement reveal carbon contamination.

binding energy of carbon with iron. Another aspect to be noted is that the films were annealed to 475 K after preparation. It is known that heating can result in structural changes of the film. It is probable that the increase in temperature could cause coalescence of Fe into clusters.

The proposed hypothesis of the formation of Fe clusters could account well for the observation of slightly modified spin waves of cobalt in the Fe/Co system. The formation of larger Fe clusters instead of layers implies that spin waves were always probed at the cobalt surface, with the presence of Fe clusters introducing small deviations in spin wave energies.

7.5 Discussion

The section begins with a discussion of identical dispersion in the 4 ML Fe/Cu(100) and 4 ML Fe/Co(100) systems despite their differences in magnetic properties. This discussion is followed by the analysis of possible arguments to pinpoint the source of spin waves in the 4 ML Fe/Cu(100) system. It will be shown that the nanomartensite phase is responsible for the observed spin waves in this system. The argument is extended to explain the spin waves in 3 ML and 5 ML iron films in the last part of the section.

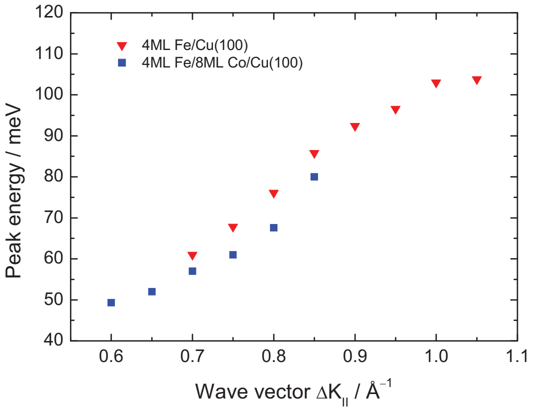

Figure 7.20: Dispersion of the surface spin waves in the systems 4 ML Fe/Cu(100) and 4 ML Fe/Co(100). The dispersion is nearly identical despite the difference in their magnetic anisotropy.

7.5.1 Spin waves in a 4 ML Fe film

A comparison of spin wave dispersion in 4 ML Fe/Cu(100) and 4 ML Fe/Co(100) is presented in Fig. 7.20. The dispersion is almost identical for both systems. The two systems are structurally similar exhibiting (5×1) LEED patterns as shown earlier (see Fig. 7.14). However, the systems are magnetically different due to the additional magnetic interaction present between the Co and Fe layers in the Fe/Co system. Owing to this additional magnetic interaction, the 4 ML Fe/Co(100) system exhibits a in-plane magnetization in contrast to the 4 ML Fe/Cu(100) system which shows perpendicular magnetization (see Fig. 7.12 and 7.1). One might expect this magnetic anisotropy to induce changes in the spin waves. As mentioned in Chapter 2, spin wave energies in the range of wave vectors investigated by EELS are dominated by exchange interaction. The spin-orbit interaction gives rise to magnetocrystalline anisotropy which orients the magnetic moments in a ferromagnet in certain crystallographic directions. The magnetic anisotropy energy of iron is about 10^5 J/m^3. With a lattice constant of 3.61 Å, the energy per Fe atom will be of the order of 10^{-2} meV/atom. This is about four orders of magnitude smaller than the spin wave energies ($\approx 30-100$meV). Hence one can safely assume that the contribution of magnetocrystalline anisotropy to the energy of spin waves is negligible which explains the nearly identical spin wave dispersion in the two systems. Presently, it is not clear if the small difference in energies is significant. Exploration of this fact would require additional measurements on this system as a function of Fe film thickness.

Figure 7.21 presents a comparison of the spin wave dispersion of 4 ML Fe/Cu(100) with 5 ML Fe/W(110). The 5 ML Fe/W(110) data is taken from Ref. [20]. The iron film grows pseudomorphically on the W(110) substrate and therefore exhibits a bcc(110) structure. Hence, the solid circles in Fig. 7.21 represent the surface spin

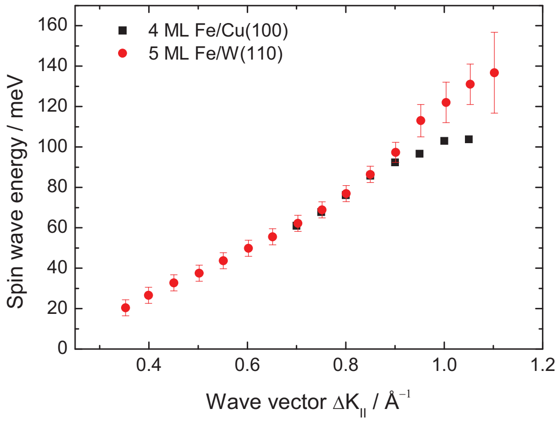

Figure 7.21: Comparison of the spin wave dispersions of the 4 ML Fe/Cu(100) with 5 ML Fe/W(110). The 5 ML Fe/W(110) dispersion is taken from Ref. [20]. The good agreement between the two dispersion curves indicates that the nanomartensitic phase, whose local atomic structure is similar to bcc is responsible for the spin waves in 4 ML Fe/Cu(100). See text for details.

wave dispersion of Fe films with iron in its native bcc structure. The spin wave dispersion of 5 ML bcc Fe and 24 ML bcc Fe were found to be almost identical indicating that the dispersion is due to the surface spin wave mode of the bulk bcc iron [20]. The spin wave energies of 4 ML Fe/Cu(100) are in overall good agreement with the spin wave dispersion of a bcc Fe film. The small deviation at high wave vectors could be attributed to the different surface Brillouin zone of the film and the substrate in the two cases [133]. The nearly identical spin wave dispersion suggests that the observed spin wave signal in the Fe/Cu(100) system stems from those sections of the surface that exhibit a “nanomartensitic” structure which is similar to the bcc(110) structure, however lacking long-range order (Fig. 7.2) [133]. The local atomic arrangement of the nanomartensite phase is related to iron’s native bcc structure with similar bond angles and out-of-plane interatomic distances [113, 114]. A more detailed account of the evolution of the nanomartensite phase and the correlation to observed spin waves is given below.

The clean 4 ML Fe films are predominantly fcc at 300 K. However, the nanomartensite phase is stabilized by two components: The presence of very small doses of hydrogen stabilizes the nanomartensite phase. The reduction of temperature is found to increase the fraction of the nanomartensite phase [115]. The fraction of the nanomartensite phase in a 4 ML film as a function of H_2 dose and temperature taken from Ref. [115] is shown in Fig. 7.22(a). The increase in nanomartensite phase with H_2 exposure is in line with the increase in film magnetization as a function of H_2 dose observed by Vollmer *et al.*, [134] in MOKE experiments. The MOKE measurements of $3-5$ ML films measured between $243-343$ K reveal that the Kerr ellipticity for clean films decreases above 3 ML. However, upon exposure to H_2, the MOKE signal increases up to and slightly above a thickness of 4 ML [134]. This indicates that the

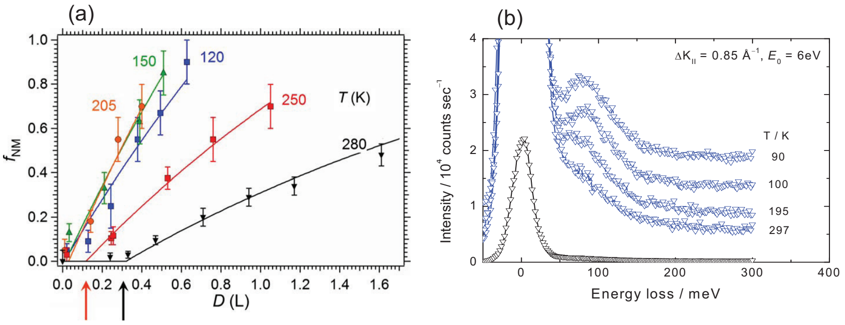

Figure 7.22: Fraction of the nanomartensitic phase in a 4 ML iron film as a function of H_2 dose and temperature. At an H_2 dose of 0.5L and a temperature of 120 K nearly 70% of the film is in the nanomartensite phase. The figure is reproduced from Ref. [115]. (b) Spin wave spectra for a 4 ML Fe film as a function of temperature. The wave vector transfer of 0.85Å^{-1} is oriented along the [011]-direction. The spin wave peak becomes pronounced as the temperature is lowered which could be attributed to the increase in the nanomartensite phase at low temperatures.

presence of the nanomartensitic phase with bcc-like character is the origin of strong ferromagnetism in these films with T_C above 300 K [111].

The iron films for the present measurements were prepared at room temperature. As mentioned earlier, H_2 unavoidably adsorbs on the Fe films from residual H_2 pressure in the chamber. The H_2 dose due to residual gas pressure in the chamber is estimated from $p \times t \times c$, where the pressure p is in the range of 3.5×10^{-10} mbar in the preparation chamber. The dosing time t is about 10 min which involves preparation of the film and transfer to the spectrometer chamber. c is the correction factor to account for the sensitivity of the ionization gauge to a particular gas. The ionization gauges are usually calibrated for N_2. The correction factor for H_2 is 2.5. Thus the H_2 dose is obtained as ≈ 0.5 L (1 L=1 Langmuir = exposure of 10^{-6} torr (1.33×10^{-6} mbar) in 1 second). The small increase in the H_2 coverage as a function of time in the spectrometer chamber ($p \approx 10^{-11}$ mbar) is not taken into account. For a H_2 dose of 0.5 L and at room temperature, only 10% of the film will be in the nanomartensite phase according to Fig. 7.22(a). Owing to the lower content of the nanomartensite phase, one observes only a tail in the energy loss spectrum as can be seen from Fig. 7.22(b). However, as the temperature is lowered, the fraction of the nanomartensitic phase increases for the given H_2 dose. At an H_2 dose of 0.5 L and temperature of 120 K approximately 70% of the film is in the nanomartensitic phase. A corresponding increase in spin wave intensity is

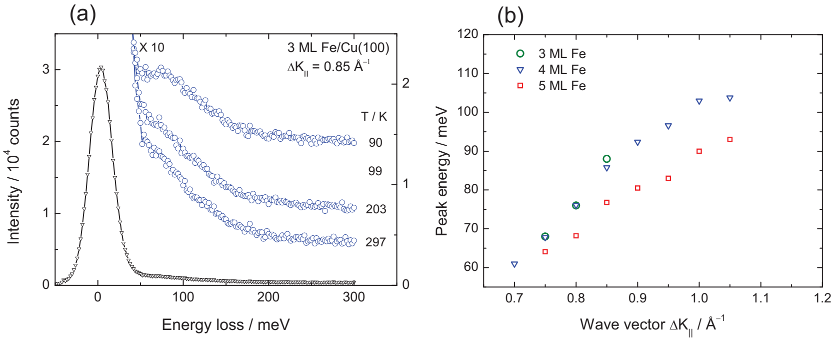

Figure 7.23: (a) Energy loss spectra of a 3 ML Fe film as a function of temperature. A tail in the elastic line at room temperature develops into a peak only at low temperatures similar to the 4 ML Fe/Cu(100) (See Fig. 7.22(b)). (b) Comparison of the spin wave dispersion of 3 ML, 4 ML, and 5 ML Fe films.

observed at low temperatures. The spin waves measured at 90 K show a clear peak (Fig. 7.22(b)), owing to a high content of the nanomartensite phase and hence high magnetization.

The observed temperature effects could also be an outcome of low T_C of the system ($\approx$ 300 K). Hence, one does not observe any spin wave peak for room temperature measurements. To test for the dominant effect among the two (nanomartensite phase or T_C) on the spin waves, a series of experiments with intentional higher hydrogen doses is required. This would imply a higher nanomartensite fraction and serve as a good test on its influence on spin waves.

7.5.2 Spin waves in 3 ML and 5 ML Fe films on Cu(100)

From the STM work of Biedermann *et al.*, one obtains the following information regarding the structure of 3 ML and 5 ML Fe films: a nominal 3 ML film is in the nanomartensite phase at least up to a temperature of 340 K even without H_2 adsorption. The Curie temperature of the system is $\approx$380 K. In the 5 ML case, the majority of films will be in the fcc phase with the nanomartensite phase occuring only at very high hydrogen exposure i.e., at hydrogen exposure close to saturation [115]. The fraction of the nanomartensite phase exhibits a similar temperature dependence as that of a 4 ML film. The Curie temperature of the system is $\approx$250 K. Despite their differences in structure, the spin waves of 3 ML and 5 ML Fe films exhibit a dispersion almost identical to that of a 4 ML film (Fig. 7.23(b)). To understand the spin waves in these two film coverages, the following model is proposed.

Figure 7.24: Intensities of low energy Auger lines of Fe (50eV) and Cu(66eV) as a function of Fe coverage. A good fit of the intensities with the mean free path model is obtained only for coverages higher than two monolayers indicating intermixing in the initial layers.

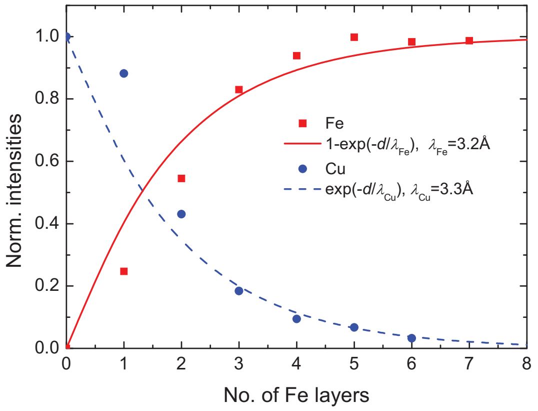

From the low energy Auger measurements one knows that the first $1-2$ layers of iron is intermixed with copper. The Auger curves shown earlier are reproduced here again (Fig. 7.24). Owing to the intermixing, the films up to 2 ML can be in a nonmagnetic phase. This is consistent with previous magnetization measurements which indicate the onset of spontaneous magnetization to be typically at $1.5-2$ ML thickness [111]. Thus, for a 3 ML system, only one layer is magnetically active. It is known that even for a perfect homoepitaxial growth under constant flux, three layers are always open. Thus, for a nominal three layer system, there will be regions of thicknesses varying between $2-4$ layers depending on the initial growth mode. Hence, I propose that the observed spin waves always stem from the four layer island regions which are in the nanomartensitic phase. Based on this model, the observed features of nominal three layer films are explained below:
(1) The emergence of spin waves from four layer islands could well account for the similar dispersion for the nominal 3 ML and 4 ML Fe films.
(2) The spin waves in a nominal three layer film are found to exhibit a similar temperature dependence as those of a 4 ML film i.e., spin waves are observed only at low temperatures (see Fig. 7.23(a)). If the spin waves stem from the actual 3 ML regions, which is supposed to be in the nanomartensitic phase at room temperature with high T_{C} (380 K), one should be able to observe at least a weak spin wave signatures at room temperature. However, spin wave peaks are observed only on lowering the temperature to 100 K.
(3) The third effect which is observed is the intensity variation of spin waves in nominal three layer films on repetition of experiments with freshly prepared samples (see Fig. 7.11(a)). This could be understood with the proposed model. The fraction of 4 ML islands is variable for each preparation which depends precisely on the growth temperature, amount of intermixing in the initial layers etc. The variation

in the area of the 4 ML islands would give rise to the observed variation in the intensity of the spin waves.

The model is now extended to explain the spin waves in nominal 5 ML films that exhibits almost similar dispersion as that of 3 ML and 4 ML Fe films (see Fig. 7.23(b)) save for a slight reduction in energies. A nominal 5 ML film will have regions of thickness varying between $4-6$ layers. The majority of the five layer and six layer regions will be in the fcc phase. A small dose of hydrogen as in our experiments will not give rise to a nanomartensite phase [115]. Hence, the five layer and six layer islands do not contribute to the spin waves. The observed spin wave signal emerges from the four layer part of the nominal five layer system. The small deviation in energies could be due to some influence from the minority regions of 5 ML films or six layer islands that are known to contain tiny fractions of bcc nanocrystals [114]. The small difference could also be an artefact from the uncertainty in determining the peak positions from broad spin wave spectra. Moreover, the measurements of 5 ML films were not repeated to ensure reproducibility and the interpretation therefore has to be taken with a grain of salt.

A detailed understanding of the correlation between structure and spin waves would necessitate a larger experimental database. One would require spin wave measurements of intermediate Fe coverages like 3.5 ML, 4.5 ML and 5.5 ML as well as intentional higher doses of H_2 for any further arguments. This study will be carried out in the future.

7.6 Summary

The spin waves of $3-5$ ML thick Fe films on Cu(100) and 4 ML thick Fe films on 8 ML Co/Cu(100) were studied. The spin wave dispersion is nearly identical to the dispersion reported for bcc Fe(110) layers grown on W(110). Hence, the spin waves are ascertained to stem from the nanomartensite phase of iron . The spin waves in nominal 3 ML and 5 ML Fe films on Cu(100) are predicted to arise from the 4 ML regions of films based on the model proposed.

8 Conclusions and outlook

This thesis has aimed at the study of high energy-high momentum surface spin waves of 3d-transition metals using electron energy loss spectroscopy. Surfaces of 3d-transition metals can be prepared either from bulk single crystals or as surfaces of epitaxial films. Epitaxial films have the advantage that different, non-equilibrium structures can be realized, depending on material, structure and orientation of the substrate. Here the focus was on the thin films grown on copper surfaces in (100) orientation. The best-defined spin wave system in this class of epitaxial films exists for fcc cobalt films on Cu(100) which can be prepared in thicknesses between 2 and 15 monolayers. For the eight monolayer cobalt film the surface spin wave energy and the energy width was determined for wave-vectors ranging between 0.2 and 1.1 Å^{-1} (Section 4.3).

As shown in Section 5.3 the attempt to find spin waves on epitaxial Ni(100) films failed.

A hitherto not reported result of this thesis is the observation of spin waves on cobalt films which are covered by several layers of nickel or copper. The discussion in Sections 6.3.2 and 6.4.2 has shown that the spin waves are localized at the cobalt side of the interface between cobalt and nickel or copper. EELS is therefore capable of studying spin waves at metal/metal interfaces.

Cobalt and nickel grow pseudomorphic on Cu(100), whereas Fe, contrary to earlier belief, realizes a special, partially disordered phase, which has been termed as "nanomartensitic". Locally this structure is akin to the (110) surface of bcc iron. Consequently, the spin wave dispersion observed for that system resembles the spin waves of bcc Fe(110).

Another new result of this thesis is the observation of a standing spin wave mode for the eight monolayer film of cobalt (section 4.3). According to the Heisenberg model (Fig. 4.14), the energy of the standing spin waves depends on the number of magnetic layers. The variation of the energies of the standing spin waves is also affected by a possible variation of the exchange coupling as a function of the number of layers. A systematic study of the standing spin waves in comparison to advanced theoretical methods could therefore provide information on the exchange coupling between the different layers. While this thesis was written, the spectrometer was further improved by a variation of the dimensions of some monochromator slits.

Standing spin wave modes are now observed with several hundred counts per second. A systematic study of standing spin waves as a function of layer thickness is thereby greatly facilitated and will be performed in the near future.

In future work, it would be interesting to study the effect of different substrates and therefore film structures on the spin waves of 3d-metal films, e.g. by depositing them on Cu(110) or Cu(111) crystals.

As a further extension of this work one may think of performing spin wave measurements on 4f-rare earth metals. The atomic magnetic moments of these materials are very large ranging about $10\mu_B$ for dysprosium and $7\mu_B$ for gadolinium [29]. However, the Curie temperatures of the majority of these metals are well below room temperature. The highest Curie temperature (gadolinium) is 289 K [29]. The low Curie temperatures despite the high magnetic moments indicate very weak exchange coupling between the atoms. Consequently, the excitation energies of short wavelength spin waves in these materials are below 10 meV [135, 136]. While such low spin wave energies could be resolved with spectrometers as used for vibration spectroscopy, the expected small intensity would presumably require the employment of multichannel detection schemes. With the spectrometers presently available one could, however, study the effect of small amounts of rare-earth materials on surface spin waves of cobalt and iron. Epitaxially grown rare-earth/3d-metal alloys are further interesting candidates for future work.

Bibliography

[1] P. Grünberg, R. Schreiber, Y. Pang, M. B. Brodsky, and H. Sowers, *Layered magnetic structures: Evidence for antiferromagnetic coupling of Fe layers across Cr interlayers*, Phys. Rev. Lett. **57**, 2442 (1986).

[2] G. Binasch, P. Grünberg, F. Saurenbach, and W. Zinn, *Enhanced magnetoresistance in layered magnetic structures with antiferromagnetic interlayer exchange*, Phys. Rev. B **39**, 4828 (1989).

[3] M. N. Baibich, J. M. Broto, A. Fert, F. N. Van Dau, F. Petroff, P. Etienne, G. Creuzet, A. Friederich, and J. Chazelas, *Giant magnetoresistance of (001)Fe/(001)Cr magnetic superlattices*, Phys. Rev. Lett. **61**, 2472 (1988).

[4] S. Parkin, C. Kaiser, A. Panchula, P. Rice, B. Hughes, M. Samant, and S. Yang, *Giant tunnelling magnetoresistance at room temperature with MgO (100) tunnel barriers*, Nat. Mater. **3**, 862 (2004).

[5] S. Yuasa, T. Nagahama, A. Fukushima, Y. Suzuki, and K. Ando, *Giant room-temperature magnetoresistance in single-crystal Fe/MgO/Fe magnetic tunnel junctions*, Nat. Mater. **3**, 868 (2004).

[6] C. Tsang, R. Fontana, T. Lin, D. Heim, V. Speriosu, B. Gurney, and M. Williams, *Design, fabrication and testing of spin-valve read heads for high density recording*, IEEE Trans. Magn. **30**, 3801 (1994).

[7] D. Mills, *On the magnetic scattering of low energy electrons from the surface of a ferromagnetic crystal*, J. Phys. Chem. Solids **28**, 2245 (1967).

[8] M. P. Gokhale, A. Ormeci, and D. L. Mills, *Inelastic scattering of low-energy electrons by spin excitations on ferromagnets*, Phys. Rev. B **46**, 8978 (1992).

[9] J. Glazer and E. Tosatti, *Theory of spin-flip excitations across the ferromagnetic stoner gap in electron energy loss*, Solid State Commun. **52**, 905 (1984).

[10] J. Kirschner, D. Rebenstorff, and H. Ibach, *High-resolution spin-polarized electron-energy-loss spectroscopy and the Stoner excitation spectrum in nickel*, Phys. Rev. Lett. **53**, 698 (1984).

[11] H. Hopster, R. Raue, and R. Clauberg, *Spin-flip Stoner excitations in a ferromagnet observed by inelastic spin-polarized electron scattering*, Phys. Rev. Lett. **53**, 695 (1984).

[12] S. Modesti, F. D. Valle, R. Rosei, E. Tosatti, and J. Glazer, *Ferromagnetic Stoner excitations detected by electron-energy-loss spectroscopy*, Phys. Rev. B **31**, 5471 (1985).

[13] D. Venus and J. Kirschner, *Momentum dependence of the stoner excitation spectrum of iron using spin-polarized electron-energy-loss spectroscopy*, Phys. Rev. B **37**, 2199 (1988).

[14] M. Plihal and D. L. Mills, *Spin-flip exchange scattering of low-energy electrons in ferromagnetic iron*, Phys. Rev. B **58**, 14407 (1998).

[15] M. Plihal, D. L. Mills, and J. Kirschner, *Spin wave signature in the spin polarized electron energy loss spectrum of ultrathin Fe films: Theory and experiment*, Phys. Rev. Lett. **82**, 2579 (1999).

[16] H. Ibach, D. Bruchmann, R. Vollmer, M. Etzkorn, P. S. A. Kumar, and J. Kirschner, *A novel spectrometer for spin-polarized electron energy-loss spectroscopy*, Rev. Sci. Instrum. **74**, 4089 (2003).

[17] R. Vollmer, M. Etzkorn, P. S. A. Kumar, H. Ibach, and J. Kirschner, *Spin-polarized electron energy loss spectroscopy of high energy, large wave vector spin waves in ultrathin fcc Co films on Cu(001)*, Phys. Rev. Lett. **91**, 147201 (2003).

[18] R. Vollmer, M. Etzkorn, P. Kumar, H. Ibach, and J. Kirschner, *Spin-wave excitation observed by spin-polarized electron energy loss spectroscopy: a new method for the investigation of surface- and thin-film spin waves on the atomic scale*, Thin Solid Films **464**, 42 (2004).

[19] R. Vollmer, M. Etzkorn, P. Kumar, H. Ibach, and J. Kirschner, *Spin-polarized electron energy loss spectroscopy: a method to measure magnon energies*, J. Magn. Magn. Mater. **272**, 2126 (2004).

[20] Y. Zhang, *High wave vector spin waves in ultrathin Fe films on W(110) studied by spin-polarized electron energy loss spectroscopy*, Ph.D. thesis, Martin-Luther University Halle-Wittenberg, Halle (2009).

[21] M. Etzkorn, *Spin waves with high energy and momentum in ultrathin Co-films studied by spin-polarized electron energy loss spectroscopy*, Ph.D. thesis, Martin-Luther University Halle-Wittenberg, Halle (2005).

[22] J. Prokop, W. X. Tang, Y. Zhang, I. Tudosa, T. R. F. Peixoto, K. Zakeri, and J. Kirschner, *Magnons in a ferromagnetic monolayer*, Phys. Rev. Lett. **102**, 177206 (2009).

[23] K. Zakeri, Y. Zhang, J. Prokop, T.-H. Chuang, N. Sakr, W. X. Tang, and J. Kirschner, *Asymmetric spin-wave dispersion on fe(110): Direct evidence of the Dzyaloshinskii-Moriya interaction*, Phys. Rev. Lett. **104**, 137203 (2010).

[24] K. Zakeri, Y. Zhang, T.-H. Chuang, and J. Kirschner, *Magnon lifetimes on the Fe(110) surface: The role of spin-orbit coupling*, Phys. Rev. Lett. **108**, 197205 (2012).

[25] H. Ibach, J. Rajeswari, and C. M. Schneider, *An electron energy loss spectrometer designed for studies of electronic energy losses and spin waves in the large momentum regime*, Rev. Sci. Instrum. **82**, 123904 (2011).

[26] H. Ibach and J. Rajeswari, *Electron energy loss spectrometers: An advanced operation mode for the lens system and the quantitative calculation of solid angle and transmission*, J. Electron Spectrosc. Relat. Phenom. **185**, 61 (2012).

[27] C. A. F. Vaz, J. A. C. Bland, and G. Lauhoff, *Magnetism in ultrathin film structures*, Rep. Prog. Phys. **71**, 056501 (2008).

[28] D. L. Mills, in *Surface excitations*, edited by M. Agranovitch and R. Loudon, volume 9 of *Modern problems in condensed matter sciences*, chapter 3, Elsevier Science Publishers B. V., North-Holland (1984).

[29] J. Stöhr and H. Siegmann, *Magnetism: from fundamentals to nanoscale dynamics*, Springer series in solid-state sciences, Springer-Verlag, Berlin Heidelberg (2006).

[30] W. Heisenberg, *On the theory of ferromagnetism*, Z. Phys. **49**, 619 (1928).

[31] E. C. Stoner, *Collective electron ferromagnetism*, Proc. Roy. Soc. A **165**, 0372 (1938).

[32] E. P. Wohlfarth, *Band model and ferromagnetism*, IMA J. Appl. Math. **4**, 359 (1968).

[33] J. Kirschner, *Direct and exchange contributions in inelastic scattering of spin-polarized electrons from iron*, Phys. Rev. Lett. **55**, 973 (1985).

[34] T. G. Phillips and H. M. Rosenberg, *Spin waves in ferromagnets*, Rep. Prog. Phys. **29**, 285 (1966).

[35] C. Herring and C. Kittel, *On the theory of spin waves in ferromagnetic media*, Phys. Rev. **81**, 869 (1951).

[36] F. Bloch, *On the theory of ferromagnetism*, Z. Phys. **61**, 206 (1930).

[37] H. Ibach, *Physics of Surfaces and Interfaces*, Springer Berlin Heidelberg New York (2006).

[38] C. M. Schneider, P. Schuster, M. Hammond, H. Ebert, J. Noffke, and J. Kirschner, *Spin-resolved electronic bands of fct cobalt*, J. Phys.: Condens. Matter **3**, 4349 (1991).

[39] H. Ibach and H. Lüth, *Solid-State Physics: An Introduction to Principles of Materials Science*, Advanced Texts in Physics, Springer-Verlag berlin Heidelberg New York, third edition (2003).

[40] C. Kittel, *Introduction to solid state physics*, John Wiley and Sons Inc., New York Chichester Brisbane Toronto Singapore, seventh edition (1996).

[41] M. Farle, *Ferromagnetic resonance of ultrathin metallic layers*, Rep. Prog. Phys. **61**, 755 (1998).

[42] D. L. Mills, *Fundamentals and Theory*, volume 1 of *Handbook of Magnetism and Advanced Magnetic Materials*, John Wiley & Sons, Ltd. (2007).

[43] S. Demokritov, B. Hillebrands, and A. Slavin, *Brillouin light scattering studies of confined spin waves: linear and nonlinear confinement*, Physics Reports **348**, 441 (2001).

[44] R. Damon and J. Eshbach, *Magnetostatic modes of a ferromagnet slab*, J. Phys. Chem. Solids **19**, 308 (1961).

[45] J. R. Dutcher, B. Heinrich, J. F. Cochran, D. A. Steigerwald, and J. W. F. Egelhoff, *Magnetic properties of sandwiches and superlattices of fcc Fe(001) grown on Cu(001) substrates*, J. Appl. Phys. **63**, 3464 (1988).

[46] M. P. Seah and W. A. Dench, *Quantitative electron spectroscopy of surfaces: A standard data base for electron inelastic mean free paths in solids*, Surf. Interface Anal. **1**, 2 (1979).

[47] J. Hong and D. L. Mills, *Spin dependence of the inelastic electron mean free path in Fe and Ni: Explicit calculations and implications*, Phys. Rev. B **62**, 5589 (2000).

[48] D. L. Abraham and H. Hopster, *Magnetic probing depth in spin-polarized secondary electron spectroscopy*, Phys. Rev. Lett. **58**, 1352 (1987).

[49] E. Vescovo, C. Carbone, U. Alkemper, O. Rader, T. Kachel, W. Gudat, and W. Eberhardt, *Spin-dependent electron scattering in ferromagnetic Co layers on Cu(111)*, Phys. Rev. B **52**, 13497 (1995).

[50] H. Ibach, M. Etzkorn, and J. Kirschner, *Electron spectrometers for inelastic scattering from magnetic surface excitations*, Surf. Interface Anal. **38**, 1615 (2006).

[51] J. Rajeswari, H. Ibach, C. M. Schneider, A. T. Costa, D. L. R. Santos, and D. L. Mills, *Surface spin waves of fcc cobalt films on Cu(100): High-resolution spectra and comparison to theory*, Phys. Rev. B **86**, 165436 (2012).

[52] H. B. Michaelson, *The work function of the elements and its periodicity*, J. Appl. Phys. **48**, 4729 (1977).

[53] M. Shiraishi and M. Ata, *Work function of carbon nanotubes*, Carbon **39**, 1913 (2001).

[54] A. T. Costa, R. B. Muniz, and D. L. Mills, *Theory of large-wave-vector spin waves in ultrathin ferromagnetic films: Sensitivity to electronic structure*, Phys. Rev. B **70**, 054406 (2004).

[55] A. T. Costa, R. B. Muniz, and D. L. Mills, *Theory of spin waves in ultrathin ferromagnetic films: The case of Co on Cu(100)*, Phys. Rev. B **69**, 064413 (2004).

[56] A. T. Costa, R. B. Muniz, and D. L. Mills, *Theory of spin excitations in Fe(110) multilayers*, Phys. Rev. B **68**, 224435 (2003).

[57] T. Nishizawa and K. Ishida, *The Co (cobalt) system*, J. Phase equilib. **4**, 387 (1983).

[58] C. M. Schneider, P. Bressler, P. Schuster, J. Kirschner, J. J. de Miguel, and R. Miranda, *Curie temperature of ultrathin films of fcc-cobalt epitaxially grown on atomically flat Cu(100) surfaces*, Phys. Rev. Lett. **64**, 1059 (1990).

[59] C. M. Schneider, A. K. Schmid, H. P. Oepen, and J. Kirschner, *Influence of Growth and Structure on the Magnetism of Epitaxial Cobalt Films on Cu(100)*, Plenum Press, New York, (1993).

[60] A. Clarke, G. Jennings, R. F. Willis, P. J. Rous, and J. B. Pendry, *A LEED determination of the structure of cobalt overlayers grown on a single-crystal Cu(001) substrate*, Surf. Sci. **187**, 327 (1987).

[61] T. Allmers and M. Donath, *Controlling Cu diffusion in Co films grown on Cu(001)*, Surf. Sci. **605**, 1875 (2011).

[62] S. T. Coyle, G. G. Hembree, and M. Scheinfein, *Growth, morphology, and magnetic properties of ultrathin epitaxial Co films on Cu(100)*, J. Vac. Sci. Technol. A **15**, 1785 (1997).

[63] M. T. Kief and W. F. Egelhoff, *Growth and structure of Fe and Co thin films on Cu(111), Cu(100), and Cu(110): A comprehensive study of metastable film growth*, Phys. Rev. B **47**, 10785 (1993).

[64] J. Fassbender, R. Allenspach, and U. Dürig, *Intermixing and growth kinetics of the first Co monolayers on Cu(001)*, Surf. Sci. **383**, L742 (1997).

[65] F. Huang, M. T. Kief, G. J. Mankey, and R. F. Willis, *Magnetism in the few-monolayers limit: A surface magneto-optic kerr-effect study of the magnetic behavior of ultrathin films of Co, Ni, and Co-Ni alloys on Cu(100) and Cu(111)*, Phys. Rev. B **49**, 3962 (1994).

[66] J. H. Neave, B. A. Joyce, P. J. Dobson, and N. Norton, *Dynamics of film growth of GaAs by MBE from RHEED observations*, Appl. Phys. A **31**, 1 (1983).

[67] S. Andersson, *Vibrational excitations and structure of CO chemisorbed on Cu(100)*, Surf. Sci. **89**, 477 (1979).

[68] I. Dzyaloshinsky, *A thermodynamic theory of "weak" ferromagnetism of antiferromagnetics*, J. Phys. Chem. Solids **4**, 241 (1958).

[69] T. Moriya, *Anisotropic superexchange interaction and weak ferromagnetism*, Phys. Rev. **120**, 91 (1960).

[70] L. Rayleigh, *On waves propagated along the plane surface of an elastic solid*, Proc. London Math. Soc. **s1-17**, 4 (1885).

[71] K.-P. Kämper, D. L. Abraham, and H. Hopster, *Spin-polarized electron-energy-loss spectroscopy on epitaxial fcc Co layers on Cu(001)*, Phys. Rev. B **45**, 14335 (1992).

[72] M. Mohamed, J.-S. Kim, and L. Kesmodel, *Surface phonon dispersion in ultrathin epitaxial films of Co on Cu(001)*, Surf. Sci. **220**, L687 (1989).

[73] M. Balden, S. Lehwald, E. Preuss, and H. Ibach, *Surface phonons of the clean and H-covered W(110) surface measured with EELS*, Surf. Sci. **307, Part B**, 1141 (1994).

[74] B. M. Hall, S. Y. Tong, and D. L. Mills, *Large-angle electron-energy-loss spectroscopy with the inclusion of a surface image potential*, Phys. Rev. Lett. **50**, 1277 (1983).

[75] E. G. McRae, *Electronic surface resonances of crystals*, Rev. Mod. Phys. **51**, 541 (1979).

[76] R. N. Sinclair and B. N. Brockhouse, *Dispersion relation for spin waves in a fcc cobalt alloy*, Phys. Rev. **120**, 1638 (1960).

[77] J. F. Cooke, J. W. Lynn, and H. L. Davis, *Calculations of the dynamic susceptibility of nickel and iron*, Phys. Rev. B **21**, 4118 (1980).

[78] P. Buczek, A. Ernst, and L. M. Sandratskii, *Different dimensionality trends in the Landau damping of magnons in iron, cobalt, and nickel: Time-dependent density functional study*, Phys. Rev. B **84**, 174418 (2011).

[79] R. B. Muniz and D. L. Mills, *Theory of spin excitations in Fe(110) monolayers*, Phys. Rev. B **66**, 174417 (2002).

[80] A. T. Costa, R. B. Muniz, and D. L. Mills, *Spin waves and their damping in itinerant ultrathin ferromagnets: Intermediate wave vectors*, Phys. Rev. B **74**, 214403 (2006).

[81] S. Lounis, A. T. Costa, R. B. Muniz, and D. L. Mills, *Theory of local dynamical magnetic susceptibilities from the Korringa-Kohn-Rostoker Green function method*, Phys. Rev. B **83**, 035109 (2011).

[82] H. Tang, M. Plihal, and D. Mills, *Theory of the spin dynamics of bulk Fe and ultrathin Fe(100) films*, J. Magn. Magn. Mater. **187**, 23 (1998).

[83] J. Hong and D. L. Mills, *Spin excitations in ferromagnetic Ni: Electrons and neutrons as a probe*, Phys. Rev. B **61**, R858 (2000).

[84] D. L. Abraham and H. Hopster, *Spin-polarized electron-energy-loss spectroscopy on Ni*, Phys. Rev. Lett. **62**, 1157 (1989).

[85] H. A. Mook and D. M. Paul, *Neutron-scattering measurement of the spin-wave spectra for nickel*, Phys. Rev. Lett. **54**, 227 (1985).

[86] H. Ibach, private communication.

[87] B. Schulz and K. Baberschke, *Crossover from in-plane to perpendicular magnetization in ultrathin Ni/Cu(001) films*, Phys. Rev. B **50**, 13467 (1994).

[88] K. Baberschke, *The magnetism of nickel monolayers*, Appl. Phys. A - Mater. **62**, 417 (1996).

[89] W. L. O'Brien, T. Droubay, and B. P. Tonner, *Transitions in the direction of magnetism in Ni/Cu(001) ultrathin films and the effects of capping layers*, Phys. Rev. B **54**, 9297 (1996).

[90] F. Huang, G. J. Mankey, M. T. Kief, and R. F. Willis, *Finite-size scaling behavior of ferromagnetic thin films*, J. Appl. Phys. **73**, 6760 (1993).

[91] M. Tischer, D. Arvanitis, T. Yokoyama, T. Lederer, L. Tröger, and K. Baberschke, *Temperature dependent MCXD measurements of thin Ni films on Cu(100)*, Surf. Sci. **307**, 1096 (1994).

[92] H. Ibach and S. Lehwald, *Temperature dependence of interband transitions and exchange splitting in nickel*, Solid State Commun. **45**, 633 (1983).

[93] P. Srivastava, N. Haack, H. Wende, R. Chauvistré, and K. Baberschke, *Modifications of the electronic structure of Ni/Cu(001) as a function of the film thickness*, Phys. Rev. B **56**, R4398 (1997).

[94] P. Srivastava, F. Wilhelm, A. Ney, M. Farle, H. Wende, N. Haack, G. Ceballos, and K. Baberschke, *Magnetic moments and Curie temperatures of Ni and Co thin films and coupled trilayers*, Phys. Rev. B **58**, 5701 (1998).

[95] F. Wilhelm, U. Bovensiepen, A. Scherz, P. Poulopoulos, A. Ney, H. Wende, G. Ceballos, and K. Baberschke, *Manipulation of the Curie temperature and the magnetic moments of ultrathin Ni and Co films by cu-capping*, J. Magn. Magn. Mater. **222**, 163 (2000).

[96] A. Ney, P. Poulopoulos, and K. Baberschke, *Surface and interface magnetic moments of Co/Cu(001)*, EuroPhys. Lett. **54**, 820 (2001).

[97] Y. Tserkovnyak, A. Brataas, and G. E. W. Bauer, *Enhanced Gilbert damping in thin ferromagnetic films*, Phys. Rev. Lett. **88**, 117601 (2002).

[98] L. Berger, *Emission of spin waves by a magnetic multilayer traversed by a current*, Phys. Rev. B **54**, 9353 (1996).

[99] J. Callaway and C. S. Wang, *Self-consistent calculation of energy bands in ferromagnetic nickel*, Phys. Rev. B **7**, 1096 (1973).

[100] S. S. Dhesi, H. A. Dürr, G. van der Laan, E. Dudzik, and N. B. Brookes, *Electronic and magnetic structure of thin Ni films on Co/Cu(001)*, Phys. Rev. B **60**, 12852 (1999).

[101] S. S. Dhesi, H. A. Dürr, E. Dudzik, G. v. d. Laan, and N. B. Brookes, *Magnetism and electron redistribution effects at Ni/Co interfaces*, Phys. Rev. B **61**, 6866 (2000).

[102] S. S. Dhesi, E. Dudzik, H. A. Durr, G. van der Laan, and N. B. Brookes, *Electron correlation and charge transfer at the Ni/Co interface*, J. Appl. Phys. **87**, 5466 (2000).

[103] H.-J. Ernst, F. Fabre, and J. Lapujoulade, *Growth of Cu on Cu(100)*, Surf. Sci. **275**, L682 (1992).

[104] C. S. Wang, B. M. Klein, and H. Krakauer, *Theory of magnetic and structural ordering in iron*, Phys. Rev. Lett. **54**, 1852 (1985).

[105] F. J. Pinski, J. Staunton, B. L. Gyorffy, D. D. Johnson, and G. M. Stocks, *Ferromagnetism versus antiferromagnetism in face-centered-cubic iron*, Phys. Rev. Lett. **56**, 2096 (1986).

[106] V. L. Moruzzi, P. M. Marcus, K. Schwarz, and P. Mohn, *Ferromagnetic phases of bcc and fcc Fe, Co, and Ni*, Phys. Rev. B **34**, 1784 (1986).

[107] O. N. Mryasov, V. A. Gubanov, and A. I. Liechtenstein, *Spiral-spin-density-wave states in fcc iron: Linear-muffin-tin-orbitals band-structure approach*, Phys. Rev. B **45**, 12330 (1992).

[108] N. Kamakura, A. Kimura, T. Saitoh, O. Rader, K.-S. An, and A. Kakizaki, *Magnetism of Fe films grown on Co(100) studied by spin-resolved Fe* 3*s photoemission*, Phys. Rev. B **73**, 094437 (2006).

[109] T. Bernhard, M. Baron, M. Gruyters, and H. Winter, *Surface structure of ultrathin Fe films on Cu(001) revisited*, Phys. Rev. Lett. **95**, 087601 (2005).

[110] L. Hammer, S. Müller, and K. Heinz, *Fe/Cu(100)-a test case for the understanding of epitaxially grown magnetic thin films*, Surf. Sci. **569**, 1 (2004).

[111] J. Thomassen, F. May, B. Feldmann, M. Wuttig, and H. Ibach, *Magnetic live surface layers in Fe/Cu(100)*, Phys. Rev. Lett. **69**, 3831 (1992).

[112] K. Heinz, S. Müller, and L. Hammer, *Crystallography of ultrathin iron, cobalt and nickel films grown epitaxially on copper*, J. Phys.: Condens. Matter **11**, 9437 (1999).

[113] A. Biedermann, R. Tscheließnig, M. Schmid, and P. Varga, *Crystallographic structure of ultrathin Fe films on Cu(100)*, Phys. Rev. Lett. **87**, 086103 (2001).

[114] A. Biedermann, R. Tscheliessnig, M. Schmid, and P. Varga, *Local atomic structure of ultra-thin Fe films grown on Cu(100)*, Appl. Phys. A - Mater. **78**, 807 (2004).

[115] A. Biedermann, *Stability of the nanomartensitic phase in ultrathin Fe films on Cu(100)*, Phys. Rev. B **80**, 235403 (2009).

[116] W. O'Brien and B. Tonner, *Magnetic phases of ultrathin Fe films on fcc Co(001)*, Surf. Sci. **334**, 10 (1995).

[117] E. J. Escorcia-Aparicio, R. K. Kawakami, and Z. Q. Qiu, *fcc Fe films grown on a ferromagnetic fcc Co(100) substrate*, Phys. Rev. B **54**, 4155 (1996).

[118] S. Müller, P. Bayer, C. Reischl, K. Heinz, B. Feldmann, H. Zillgen, and M. Wuttig, *Structural instability of ferromagnetic fcc Fe films on Cu(100)*, Phys. Rev. Lett. **74**, 765 (1995).

[119] K. Heinz, S. Müller, and P. Bayer, *Iron multilayers on Cu(100) - a case of complex reconstruction investigated by quantitative LEED*, Surf. Sci. **352**, 942 (1996).

[120] C. Egawa, E. M. McCash, and R. F. Willis, *Adsorption of hydrogen on thin fcc-iron films grown on Cu(100)*, Surf. Sci. Lett. **215**, L271 (1989).

[121] A. Biedermann, R. Tscheliessnig, C. Klein, M. Schmid, and P. Varga, *Reconstruction of the clean and H covered magnetic live surface layer of Fe films grown on Cu(100)*, Surf. Sci. **563**, 110 (2004).

[122] K. Johnson, D. Chambliss, R. Wilson, and S. Chiang, *A structural model and mechanism for Fe epitaxy on Cu(100)*, Surf. Sci. **313**, L811 (1994).

[123] A. Barò and W. Erley, *The chemisorption of hydrogen on a (110) iron crystal studied by vibrational spectroscopy (EELS)*, Surf. Sci. Lett. **112**, L759 (1981).

[124] H. Ibach, *Electron energy loss spectroscopy of the vibration modes of water on Ag(100) and Ag(115) surfaces and comparison to Au(100), Au(111) and Au(115)*, Surf. Sci. **606**, 1534 (2012).

[125] H. Li and B. P. Tonner, *Structure and growth mode of metastable fee cobalt ultrathin films on Cu(001) as determined by angle-resolved X-ray photoemission scattering*, Surf. Sci. **237**, 141 (1990).

[126] N. Kamakura, A. Kimura, O. Rader, A. Harasawa, and A. Kakizaki, *Spin- and angle-resolved photoemission of face-centered tetragonal Fe/Co(001)*, J. Electron Spectrosc. Relat. Phenom. **92**, 45 (1998).

[127] H. Magnan, D. Chandesris, B. Villette, O. Heckmann, and J. Lecante, *Structure of thin metastable epitaxial fe films on cu(100): Reconstruction and interface ordering by coating*, Phys. Rev. Lett. **67**, 859 (1991).

[128] H. Landskron, G. Schmidt, K. Heinz, and K. M *Low-temperature p2mg(2X1) structure of ultrathin epitaxial films Fe/Cu(100)*, Surf. Sci. **256**, 115 (1991).

[129] D. P. Pappas, K.-P. Kämper, and H. Hopster, *Reversible transition between perpendicular and in-plane magnetization in ultrathin films*, Phys. Rev. Lett. **64**, 3179 (1990).

[130] D. Li, M. Freitag, J. Pearson, Z. Q. Qiu, and S. D. Bader, *Magnetic and structural instabilities of ferromagnetic and antiferromagnetic Fe/Cu(100)*, J. Appl. Phys. **76**, 6425 (1994).

[131] A. Berger, B. Feldmann, H. Zillgen, and M. Wuttig, *Correlation between the microscopic and macroscopic magnetic properties in ultrathin Fe/Cu(100)-films*, J. Magn. Magn. Mater. **183**, 35 (1998).

[132] A. Brodde and H. Neddermeyer, *Scanning tunneling microscopy on the growth of Fe films on Cu(100)*, Surf. Sci. **287, Part 2**, 988 (1993).

[133] J. Rajeswari, H. Ibach, and C. M. Schneider, *Large wave vector surface spin waves of the nanomartensitic phase in ultrathin iron films on Cu(100)*, Europhys. Lett. **101**, 17003 (2013).

[134] R. Vollmer and J. Kirschner, *Influence of* H_2 *adsorption on magnetic properties of Fe films on* Cu(001), Phys. Rev. B **61**, 4146 (2000).

[135] R. M. Nicklow, N. Wakabayashi, M. K. Wilkinson, and R. E. Reed, *Spin-wave dispersion relation in dysprosium metal*, Phys. Rev. Lett. **26**, 140 (1971).

[136] H. G. Bohn, W. Zinn, B. Dorner, and A. Kollmar, *Neutron scattering study of spin waves and exchange interactions in ferromagnetic EuS*, Phys. Rev. B **22**, 5447 (1980).

List of Own Publications

(in chronological order)

Papers

- H. Ibach, **J. Rajeswari** and C. M. Schneider
  “An electron energy loss spectrometer designed for studies of electronic energy losses and spin waves in the large momentum regime”
  Review of Scientific Instruments **82**, 123904 (2011).
- H. Ibach and **J. Rajeswari**
  “Electron energy loss spectrometers: An advanced operation mode for the lens system and the quantitative calculation of solid angle and transmission”
  Journal of Electron Spectroscopy and Related Phenomena **185**, 61 (2012).
- **J. Rajeswari**, H. Ibach, C. M. Schneider, A. T. Costa, D. L. R. Santos and D. L. Mills
  “Surface spin waves of fcc cobalt films on Cu(100): High-resolution spectra and comparison to theory”
  Physical Review B **86**, 2165436 (2012).
- **J. Rajeswari**, H. Ibach and C. M. Schneider
  “Large wave vector surface spin waves of the nanomartensitic phase in ultrathin iron films on Cu(100)”
  Europhysics Letters **101**, 17003 (2013).

Poster Contributions

- **J. Rajeswari**, L. Baumgarten, B. Küpper, H. Ibach, C. M. Schneider
  "Spin-polarized electron energy loss spectroscopic studies of ultrathin films"
  Delta user meeting 2011, Dortmund, Germany.
- **J. Rajeswari**, L. Baumgarten, B. Küpper, H. Ibach, C. M. Schneider
  "A novel electron spectrometer for surface magnon scattering"
  DPG spring meeting 2011, Dresden, Germany.
- **J. Rajeswari**, H. Ibach, C. M. Schneider
  "A new mode of operation of electron energy loss spectrometers: Application to surface magnon and surface vibration spectra"
  DPG spring meeting 2012, Berlin, Germany.

Talks

- "High resolution electron energy loss spectroscopic studies of surface spin waves in ultrathin Co films on Cu(001)"
  DPG spring meeting 2012, Berlin, Germany.

Acknowledgements

At the end of my thesis, it is a pleasant task to look back my journey of PhD and express my heartfelt and sincere thanks to many people who have helped me walk this path filled with roses and thorns. I would like to thank each and every one of them who encouraged me at every difficult step, to rejoice because thorns have roses and not complain because roses have thorns. However, I am mentioning only a significant few, due to the space constraints.

Firstly, I would like to thank my doctoral thesis advisor Prof. Dr. C. M. Schneider. I thank you for believing me and taking a risk in providing me the opportunity for pursuing PhD in your group. I thank you for your constant support, helpful discussions and guidance. You always found time for me whenever I needed your help. Thank you very much. I always admire your ever-smiling face, in spite of your neck-deep work as director of an institute.

I express my sincere thanks to Prof. Dr. Hans Peter Oepen for being a co-reviewer of my thesis.

I could write a whole chapter thanking Prof. Dr. Harald Ibach, who is the instrumental person behind this thesis, and I still wouldn't do justice. Three years ago I joined the EELS lab with little or no knowledge of the subject. It is under your tutelage that I learnt to look for a pearl in this mighty ocean. It is under your tutelage that I learnt physics is indeed fun. I salute your passion and commitment. I treasure the following advice received from you: "A true scientist should primarily get his satisfaction out of the ability to understand something, that has not been studied before whether it is exciting or not!". I have been very lucky to have you as my supervisor. You will always remain an inspiration for me.

Bernd Küpper! Three years ago when I landed here, first time facing life outside India, you gave me a warm welcome. From then on you became my local guardian, friend and above all the most wonderful technician we could ever ask for. You always had immediate solutions for my problems. Thank you very much Bernd. I also thank your wife, Mrs. Jutta Küpper for all her love and affection.

I thank Dr. Hari Babu for initiating me to research. Thank you for showing me that a road exist beyond M.Sc and ISRO. A road which is less travelled.

Special thanks to Hatice, Christian, Saban and Zhou. Thank you all for providing me with a social life outside research. I cherish the long conversations over a cup of coffee or Pizza with you people. Thank you friends. Thank you so much. I cherish the midnight cooking adventures and marathon chattings with Hatice. Thank you Hatice. Your friendship mean a lot to me.

I thank Dr. Claire Besson for her timely help usually in short notices. Whether it is for fixing my bicycle or fixing the bugs in latex or taking me (and Cate) for a Paris trip or proof reading this thesis, she was always there for me as a good friend. Claire, here is my sincere thanks.

I thank Prof. Dr. Paul Bechthold for his valuable suggestions in this thesis.

I thank all the colleagues from our institute, the PGI-6, for the ambient atmosphere. I thank Denis Rudolf, Moritz Plötzing and Dr. Frank Matthes for being wonderful office mates. Cate, thank you for being a good friend for me.

I thank Heinz Pfeiffer and Jürgen Lauer for their able technical support in electronics.

Many thanks to Margret Frey for assisting me with administrative stuff and paper works.

Shilpa, thank you for being there for me whenever I needed you.

Finally, I would like to thank all my family members for their unconditional love and support in all walks of my life. Heartily thanks to my uncles and aunts Sankar, Chandra, Subramanian and Priya. Special thanks to my sister Kameswari and her family for their support. I am indebted to my grandparents K. S. Ramamoorthy and Swarnam for their unlimited love since my childhood and teaching me the morals of life. My dear'est' parents, S. Jayaraman and Malini Jayaraman: words are not enough to thank you for all that you have done for me. Thank you for all your sacrifices so that I could achieve my goal. Thank you for providing me with opportunities more than I could ask for. Thank you for providing me with all comforts. I owe everything to you.

Curriculum Vitae

Personal Data

Rajeswari Jayaraman
born 08.11.1986 in Chennai, India

Education

Apr. 2003	High school Diploma
Jun. 2003–Apr. 2006	Bachelor student, University of Madras, Chennai, India
Apr. 2006	Bachelor of Science in Physics
Jun. 2006–Apr. 2008	Master student, Department of Physics, Anna University, Chennai, India Thesis title: *“Investigation of filler’s effect on Mg based polymer electrolyte”*
Apr. 2008	Master of Science in Materials Science
Sep. 2008–Aug. 2009	Project Associate, Indian Institute of Technology Madras, Chennai, India
Jan. 2010–present	Ph.D. in physics Peter Grünberg Institut Forschungszentrum Jülich Supervisor: Prof. Dr. C. M. Schneider

Jülich, June 20th 2013

Band / Volume 54
Einfluss unkonventioneller Medien auf die Selektivität ThDP-abhängiger Enzyme
T. Gerhards (2013), XIV, 199 pp
ISBN: 978-3-89336-846-4

Band / Volume 55
Aufbau einer Vierspitzen-Rastertunnelmikroskop/Rasterelektronenmikroskop-Kombination und Leitfähigkeitsmessungen an Silizid Nanodrähten
E. Zubkov (2013), 150 pp
ISBN: 978-3-89336-848-8

Band / Volume 56
Interplay between magnetic and dielectric phenomena at transition metal oxide interfaces
D. Schumacher (2013), IV, 128 pp
ISBN: 978-3-89336-855-6

Band / Volume 57
Single $NdPc_2$ Molecules on Surfaces: Adsorption, Interaction, and Molecular Magnetism
S. Fahrendorf (2013), viii, 100 pp
ISBN: 978-3-89336-856-3

Band / Volume 58
Heyd-Scuseria-Ernzerhof Screened-Exchange Hybrid Functional for Complex Materials: All-Electron Implementation and Application
M. Schlipf (2013), XV, 170 pp
ISBN: 978-3-89336-857-0

Band / Volume 59
Orbital-dependent exchange-correlation functionals in density-functional theory realized by the FLAPW method
M. Betzinger (2013), vi, 173 pp
ISBN: 978-3-89336-858-7

Band / Volume 60
Structural influences on electrical transport in nanostructures
R. D. Frielinghaus (2013), viii, 190 pp
ISBN: 978-3-89336-867-9

Band / Volume 61
Study of intermolecular interactions in hetero-organic thin films
B. Stadtmüller (2013), viii, 198 pp
ISBN: 978-3-89336-871-6

Band / Volume 62
Structure, magnetism and excitations in some Mn-based magnetocaloric effect compounds
M. Gottschlich (2013), 175 pp
ISBN: 978-3-89336-874-7

Band / Volume 63
Neutron Scattering
Lectures of the JCNS Laboratory Course held at Forschungszentrum Jülich and the research reactor FRM II of TU Munich
edited by Th. Brückel, G. Heger, D. Richter, G. Roth and R. Zorn (2013),
ca 350 pages
ISBN: 978-3-89336-880-8

Band / Volume 64
Neutron Scattering
Experiment Manuals of the JCNS Laborator Course held at Forschungszentrum Jülich and the research reactorFRM II of TU Munich
edited by Th. Brückel, G. Heger, D. Richter, G. Roth and R. Zorn (2013),
ca. 150 pages
ISBN: 978-3-89336-881-5

Band / Volume 65
Solutions of Exercises in "An Introduction to Dynamics of Colloids"
J. K. G. Dhont, K. Kang (2013), 143 pp
ISBN: 978-3-89336-882-2

Band / Volume 66
Strukturelle und chemische Charakterisierung von selbst-assemblierten Monolagen organischer Moleküle auf Oberflächen
M. Müller (2013), 168 pp
ISBN: 978-3-89336-883-9

Band / Volume 67
Adsorption of (hetero-)organic Phthalocyanine and PTCDA thin films on Ag(111)
C. Kleimann (2013), iv, 149 pp
ISBN: 978-3-89336-888-4

Band / Volume 68
High-energy high-momentum surface spin waves of ultrathin epitaxial 3d transition metal films
R. Jayaraman (2013), ix, 135 pp
ISBN: 978-3-89336-890-7

Weitere ***Schriften des Verlags im Forschungszentrum Jülich*** unter
http://wwwzb1.fz-juelich.de/verlagextern1/index.asp

Schlüsseltechnologien / Key Technologies
Band / Volume 68
ISBN 978-3-89336-890-7